7-2024

A Study of Electron- and Photon-induced Dissociative Electron Attachment to Molecules and within Anion-Molecule Clusters

Mahmudul Hasan
University of Nebraska-Lincoln

A STUDY OF ELECTRON− AND PHOTON−INDUCED DISSOCIATIVE ELECTRON ATTACHMENT TO MOLECULES AND WITHIN ANION-MOLECULE CLUSTERS.

by

Mahmudul Hasan

A DISSERTATION

Presented to the Faculty of

The Graduate College at the University of Nebraska

In Partial Fulfilment of Requirements

For the Degree of Doctor of Philosophy

Major: Physics & Astronomy

Under the Supervision of Professor Martin Centurion

Lincoln, Nebraska

July, 2024

A STUDY OF ELECTRON− AND PHOTON−INDUCED DISSOCIATIVE ELECTRON ATTACHMENT TO MOLECULES AND WITHIN ANION-MOLECULE CLUSTERS.

Mahmudul Hasan, Ph.D.

University of Nebraska, 2024

Adviser: Martin Centurion

Dissociative electron attachment (DEA) is a resonant process in which a molecule captures a low-energy electron, forming a transient negative ion (TNI). Subsequently, this unstable TNI fragments into a stable anion and one or more neutral fragments. DEA is crucial in various phenomena, ranging from atmospheric and radiation chemistry to processes occurring in plasmas, and is particularly significant in the context of radiation-induced damage to biological molecules. This study uses different experimental methods to better understand the fragmentation in molecular anions forming through dissociative photoexcitation and electron attachment. We have developed an experimental apparatus for dissociative photoexcitation studies. This apparatus generates, manipulates, and analyzes ion-molecule clusters and their fragmentation pattern. We also utilized an apparatus located at Lawrence Berkeley National Laboratory to image the three-dimensional momentum distribution of negative ions produced through DEA to molecular targets. In this dissertation, first, we describe the design of a reflectron time-of-flight (TOF) mass spectrometer, which was implemented in our experimental apparatus - designed to investigate the dissociation dynamics of photoexcited ion-molecule clusters by mass-resolving and detecting fragment anions and neutrals. Then, our experimental work demonstrates previously untested aspects of dissociative photoexcitation in molecular anions with this apparatus. We investi-

gate the DEA process in which multiple TNI states are accessed by absorbing varying numbers of photons. This multiphoton absorption method allowed us to investigate the excited states of molecular anions that may not be accessible through a single-photon absorption or with an electron beam. The significance of our approach is that it does not rely on tunable electron or laser sources to access different TNI states. Finally, we present DEA studies with an external electron beam to investigate the formation of TNIs and fragmentation patterns in different organic molecules using an anion fragment momentum imaging apparatus. We have investigated the TNI formation following low-energy electron attachment to acetic acid and its partially- and fully-deuterated isotopologues in the dissociation channels leading to H^- and D^- formation. Our results confirmed three previously known resonance positions and identified a fourth resonance that had not been reported earlier. We also examined the anion fragment yields from DEA to 1-M-5-Nitroimidazole (1M5NI) at different electron energy. This data can be used to simulate electron-induced radiation damage in biologically relevant media containing 1M5NI as a potential radiosensitizer.

DEDICATION

To Israt Jahan, my beloved wife, and my two sons Rayyan and Ruzaif.

ACKNOWLEDGMENTS

I would like to first thank my supervisor Professor Martin Centurion. He has been an invaluable mentor throughout my entire PhD journey. I am profoundly grateful for his unwavering support, insightful feedback and encouragement. His optimism, patience and consideration extended beyond academics, helping me navigate family challenges and maintain work-life balance. Perhaps his greatest gift has been cultivating my ability to learn independently, diminishing my fear of the unknown.

I extend my sincere appreciation to Dr. Danial Slaughter at LBNL for his invaluable guidance over the past four years. The opportunity to conduct research in his Berkeley lab for seven months was a privilege I deeply value. From our initial encounter during the anion group meeting, Dan has consistently demonstrated patience, offered encouragement, and generously shared both his time and resources. His mentorship has been instrumental in my scientific journey.

I would like to thank my esteemed committee members: Professor Kees Uiterwaal, Professor Alexei Gruverman, Dr. Daniel Slaughter, and Professor James Checco. Their commitment to my academic success has been remarkable. I am deeply indebted to them for their time and expertise, particularly in reviewing my comprehensive examination report and thesis. I appreciate all the work they have done on my behalf.

I am deeply grateful to all members of the Centurion group who have been instrumental in my research journey over the years. I'm particularly thankful to Dr. Xiaojun Wang for his unwavering dedication and crucial contributions to the instrumentation project. Nikhil Pachisia deserves special thanks for his support in executing the multiphoton experiment. I'm also thankful to Dr. Yanwei Xiong, Dr. Kyle Wilkin, and Dr. Sajib Kumar Saha for their warm and invaluable assistance with

laser-related issues. My heartfelt appreciation extends to my outstanding colleagues: Dr. Yibo Wang, Sri Bhavya Muvva, Jackson Lederer, Haoran Zhao, Dr. Lauren Heald, and Cuong Le. Their technical insights proved invaluable in navigating various laboratory challenges and making informed decisions, significantly enhancing the quality of my work.

I am grateful for the professional interactions I've had with researchers at LBNL. I extend my sincere thanks to Dr. Thorsten Weber for his numerous insightful discussions and invaluable support in conducting the DEA experiments. My appreciation also goes to Dr. Wael Iskandar for his expertise and discussions on data analysis methods. Additionally, I would like to thank Professor Gustavo Garcia of Instituto de Física Fundamental. During his visit to LBNL, we engaged in very interesting conversations that extended beyond research topics.

I would like to extend my appreciation to the office staff at UNL who significantly enhanced my experience during my stay there. The machine shop and electronics shop provided for exceptional expertise in addressing the various electrical and mechanical problems that arose in the lab. In the electronics shop, I would like to thank Brian Farleigh and Anatoly Mironov for their collaborative approach and skill in designing electrical components. The machine shop staff, including Bob Rhynalds, Andrew Kehm, Mike Thompson, and Pat Pribil, consistently demonstrated top-tier craftsmanship and a willingness to assist in component design.

I would also like to express my gratitude to a special group of individuals who enriched my social life and became like an extended family during my journey. My sincere thanks go to Md Sazzad Hossain, Naafis Ahnaf Shahed, Farzana Nazneen, Md Ibrahim Kholil, Dr. Sajib Kumar Saha, Jahid Hossain, and Md Abdus Sami Akanda. Their companionship, support, and willingness to engage in social activities have been invaluable, providing a sense of belonging and community that greatly enhanced my

overall experience. In addition, I extend special thanks to Md Faizul Kabir and Kanij Fatema for their unconditional willingness to help in any crisis. Their support has been a source of great comfort and reassurance.

I would like to express my gratitude to all my friends in Lincoln who made my time in the physics department vibrant and memorable: Furong Yan, Dr. Yifei Hao, Dr. Detian Yang, Dr. Ahsan Ullah, Syed Qamar Abbas, Dr. Bret Gergely, and Tianlin Li. I sincerely wish each of them great success in their future endeavors.

Earning a PhD is a significant achievement, but perhaps the greatest accomplishment during this time has been raising my two sons, Rayyan and Ruzaif. Watching you two grow has been the most rewarding experience during my doctoral journey.

I cannot thank enough to my parents with words for their sacrifice and selfless love for my whole life, and having an understanding and lovable sister is such a blessing to my life. Your encouragement and support help me go forward.

Lastly, I must acknowledge one person who has been waiting until the end of my acknowledgments to be mentioned: my beloved wife, Israt Jahan., whose unwavering support and countless sacrifices have been the foundation of my PhD journey. Her patience and understanding during the long hours and challenging moments were invaluable. While I pursued my academic goals, she not only supported my work but also took on the majority of responsibilities in raising our two children. Her strength in managing our family life, often on her own, allowed me to focus on my research. I am deeply grateful for her love, dedication, and the sacrifices she made for our family throughout this challenging yet rewarding journey.

Table of Contents

List of Figures

List of Tables

Chapter 1

Introduction

1.1 Motivation: Dissociation of Molecular Anions

When radiation interacts with matter, it easily produces low-energy electrons. These electrons can subsequently interact with the surrounding molecules. The attachment of an electron to a neutral molecule, followed by fragmentation, is a fundamental process, with a wide-range of implications. This process plays a crucial role in various fields including radiation chemistry, atmospheric chemistry, astrochemistry and astrophysics, plasma chemistry and medicine [15, 16]. In spite of extensive research being conducted for a few decades, understanding these details has remained a major challenge for experimentalists especially at low electron energies.

Dissociative electron attachment (DEA) is one of the fundamental processes in which a molecule captures a low-energy electron, forming a temporary negative ion that undergoes fragmentation into one negative ion and other neutral fragments. Normally the molecules are bombarded with the electrons from a source with sharp, controllable energy distributions, and anion productions are monitored as a function of electron energy.

DEA primarily yields information about a negative ion state forming a temporary or metastable anion [1]. With an additional electron occupying anti-bonding molec-

ular orbitals, molecular groups with high electron affinities are likely to give rise to anionic fragments. The temporary molecular anions can form at different electron energies, each accessing different negative ion states. These distinct temporary anion states can dissociate to either similar or different anionic fragments. For instance, DEA to CF_3I occurs via two distinct resonances: one near 0 eV, which exclusively produces I^-, and another core-excited resonance near 3.8 eV, which generates fragments such as F^-, IF^-, and $CF_3{}^-$ [17, 18]. In contrast, DEA to CH_3COOH leading to dissociation channel H^- involves three resonance positions at 6.8 eV, 7.8 eV, and 9.1 eV [19].

It would be interesting to be able to study DEA processes if multiple negative ion states are accessed through the absorption of different numbers of photons. Instead of varying the energy of electrons, we can modulate the intensity of the laser controlling the number of photons absorbed. This approach allows us to explore how different photon absorption scenarios influence the formation and dissociation of temporary negative ions, offering a novel perspective on the DEA dynamics. But this is not possible starting with the neutral state of the molecule.

One approach for studying DEA is to employ a gas-phase iodide ion-neutral molecule cluster forming a dimer. In these clusters, iodide typically binds weakly with polar molecules through the charge-dipole interaction. When photoexcited, the electron from the iodide is transferred to the neutral molecule, and iodine is no longer bound. The electron transfer process is similar to the mechanism of DEA where low-energy electrons are captured by the neutral molecule and form a temporary negative ion (TNI) [20]. The investigation of these ion-molecule clusters using a single-photon excitation technique, as elaborated in Section 1.3 of this chapter, mainly examines the electron binding properties and anionic dissociation pathways. Additionally, time-resolved studies have been conducted to explore the transient negative ions formed

following electron transfer in these clusters as discussed in [21] and the references therein. These studies reveal the ultrafast temporal evolution of these TNIs, including processes such as interconversion between dipole-bound and valence-bound anion states, while quantifying the time scales for autodetachment, internal conversion, and fragmentation.

The key advantage of this method is that if multiple photons are absorbed during photoexcitation of the iodide ion-molecule cluster, electrons of different energy can be transferred based on the number of photons absorbed, accessing different temporary negative ion states. Each of these temporary negative ion states can then lead to dissociation to either same or different channels. Another advantage of this approach is that upon photodetachment of the iodide ion, a low-energy free electron with a well defined kinetic energy can be captured by the adjacent molecule in the ion-molecule cluster. In DEA, it is difficult to focus and deliver a few-eV electron pulses to the target molecule, so multiphoton absorption by the ion-molecule cluster could be a alternative approach to deliver few-eV electrons to the target molecule.

Moreover, this approach could also lead to time-dependent studies by introducing a second laser pulse to probe the excited anions and measure the temporal evolution of energy and angular distributions of photoelectrons. The photoelectron angular distribution provides insights into the orbitals from which electrons are removed during ionization or detachment [22, 23]. In time-resolved experiments, photoelectron angular distribution measurements offer information on dissociation and electronic relaxation dynamics complementing the time-evolving electron kinetic energy distribution [24, 25, 26]. Furthermore, photoelectron angular distributions are sensitive to molecular alignment effects induced by the initial pump laser pulse [27, 28, 29]. When the pump pulse induces rotational coherences in an electronic state, the temporal evolution of these coherences can be monitored through measurements of time-resolved

photoelectron angular distributions [30, 31].

In order to understand the dissociation of molecular anions from a fundamental point of view, it is first necessary to understand the formation of temporary negative ions more generally.

1.2 Formation and Decay of Temporary Negative Ion

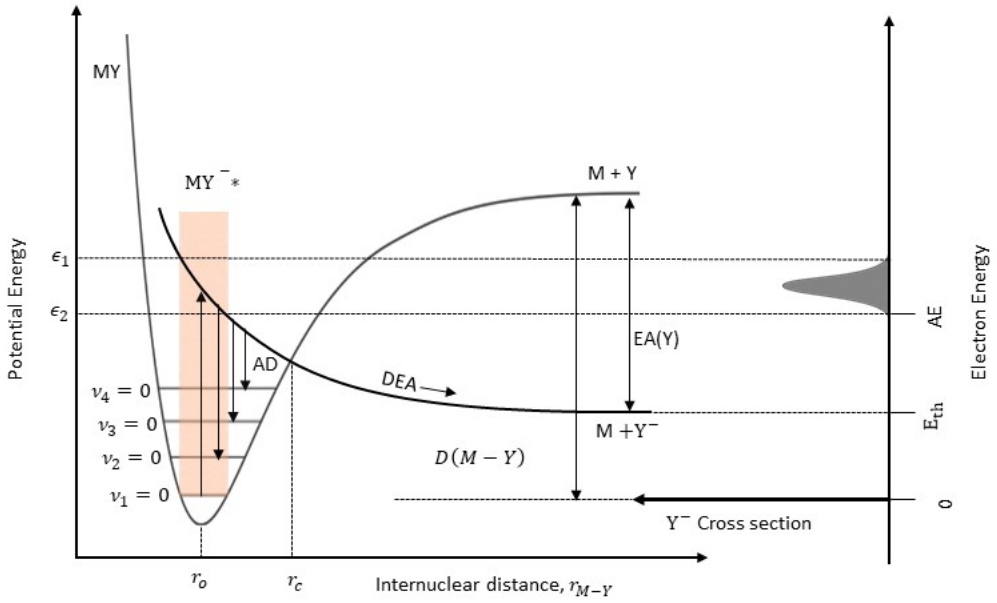

Figure 1.1: A schematic representation of the Born-Oppenheimer potential energy curves with electron attachment to a diatomic molecule MY and the subsequent relaxation processes. The possible relaxation pathways include auto-detachment (AD) and dissociative electron attachment (DEA). In the DEA pathway, the Temporary Negative Ion (TNI) moves along the repulsive potential curve and crosses the critical distance r_c. The electron affinity (EA) of the fragment Y is also shown, along with the threshold energy, E_{th}, and the appearance energy (AE) of the reaction. This figure is adapted from reference [1].

When a low energy electron is resonantly captured by a molecule for a finite amount of time, temporary negative ion (TNI) is formed. The electron capture takes

place only if the energy lies in a specific energy range. Due to this, TNI and resonance are often used interchangeably. The TNI is usually formed in an excited state and is not stable. At low energy, the electron-molecule interaction is complex and can be represented by the Born-Oppenheimer potential energy diagrams as shown in Fig. 1.1. These curves are usually applicable to diatomic molecules. However, for polyatomic molecules, these curves represent one-dimensional slices through multidimensional surfaces along specific reaction coordinates. Within the diatomic model, only a vertical transition is allowed from the ground state of the neutral to the anion state of the molecule. The transition probability for this process is proportional to the Frank-Condon factors (FCF), and is given by the square of the overlap integral between the vibrational wavefunctions for the ground state (φ^0) and the resonant state (φ^*) [32, 33]. The Frank-Condon factor is expressed as:

$$\mathrm{FCF} = | < \varphi^* | \varphi^0 > |^2 \tag{1.1}$$

In accordance with the Frank-Condon principle, FCF is highest for electrons between energies ϵ_1 and ϵ_2 and the transitions from $(\mathrm{MY} + \mathrm{e}^-)$ to MY^- are possible as shown in Fig 1.1. In other words, electron energies between ϵ_1 and ϵ_2 will be captured by the molecule forming TNI. The TNI relaxes to a stable configuration either through autodetachment (AD) or dissociative electron attachment (DEA). In AD, the extra electron is ejected, leaving the parent molecule in a vibrationally excited state. This process is schematically represented by vertical downward arrows from the repulsive potential (MY^{-*}) to the various vibrational states of the neutral molecule. AD can only occur for $r \leq r_c$, where r_c is the crossing point of the two potential energy curves. If the energy of the incoming electron is coupled to the nuclear motion of the molecule, the lifetime of the TNI state can be sufficiently long that the repulsive po-

tential energy curve of the TNI state crosses the critical distance r_c. In this case, the probability of dissociation is greater than that of autodetachment. For $r \geq r_c$, decay through AD is energetically forbidden, and TNI relaxes through DEA, resulting in the formation of a charged fragment (Y^-) and a neutral (M). Dissociation pathways due to AD and DEA can generally be illustrated by the following channels:

$$\mathrm{MY} + \mathrm{e}^-(\epsilon) \rightarrow (\mathrm{MY}^-)^* \xrightarrow{AD} \mathrm{MY} + e^- \tag{1.2}$$

$$\xrightarrow{DEA} \mathrm{M} + \mathrm{Y}^- \tag{1.3}$$

where ϵ denotes the incident energy. This interplay between electronic and nuclear degrees of freedom can lead to fascinating outcomes e.g. strong isotope effects in many DEA studies [34, 35].

In the DEA process, the available excess energy E is distributed between the kinetic energy and internal energy of the resulting fragments. This energy distribution can be described by the following balance equation:

$$\epsilon = [D(\mathrm{M}{-}\mathrm{Y}) - EA(\mathrm{Y})] + E \tag{1.4}$$

where, D(M−Y) is the bond dissociation energy of the molecule MY, EA(Y) is the electron affinity of Y and $\epsilon_1 \leq \epsilon \leq \epsilon_2$. The bracketed term on the right side of the above equation is the threshold of the reaction [1]. The appearance energy is greater than or equal to the threshold energy. Knowing the threshold energy allows us to determine the minimum energy required for the electron to initiate the process in the experiment.

During the electron attachment process, a TNI or resonance forms when an elec-

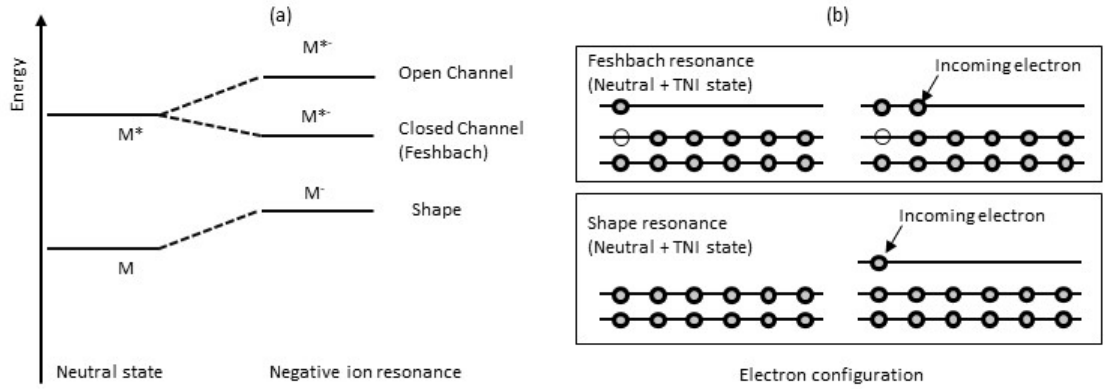

Figure 1.2: A Schematic representation of the classification of resonances is shown, illustrating (a) the relative energy positions of these states compared to the neutral state and (b) their electron configurations in both neutral and TNI states for shape and Feshbach resonances. This figure is adapted from reference [1].

tron is trapped in an unoccupied molecular orbital. This indicates the presence of a neutral state, called the parent state, for a TNI whose electron configuration is identical except for an additional captured electron. When this extra electron is removed from the negative ion resonance, the system reverts back to the parent state, restoring the electron configuration of the initial neutral molecule. Therefore, the negative ion resonance can typically be characterized by its electron configuration. There are two possible scenarios: (i) the incoming electron does not alter the electronic configuration of the neutral molecule or (ii) the electron attachment is accompanied by an electronic excitation of the neutral molecule as depicted in Fig. 1.2 [1]. The first one is called the single particle resonance where the electron finds itself attached to a previously unoccupied molecular orbital of the neutral molecule. On the other hand, the second case is called core-excited resonance where an electron is excited from one of the previously occupied molecular orbitals to an unoccupied or virtual molecular orbital, leaving a hole behind. When the energy of the core-excited resonance is lower than that of the electronically excited neutral molecule or the parent state,

it is referred to as an closed-channel or Feshbach resonance. Feshbach resonances are typically observed 0.5 eV below their parent states [36]. Conversely, if the core-excited resonance is higher than that of the neutral molecule's electronically excited state, it is referred to as open-channel core excited resonance. Single particle and open-channel core excited resonance are also called Shape resonance as the electron is trapped within a centrifugal potential barrier i.e. shape of the potential. These resonances are typically observed $0 - 2$ eV [36] above their parent state.

1.3 Charge Transfer Dissociation of Cluster Anion

In the previous section, we discussed TNIs that are categorized as conventional or valence-bound anions, where the electron is attached to the valence orbital of the molecule. However, molecular anions can also form through non-valence binding modes, influenced by the neutral precursor's dipole moment, quadrupole moment, and polarizability [37, 38].

The molecular anions we are particularly interested in are ion-molecule clusters because of their charge transfer properties, where an I^- anion is complexed with various molecules having dipole moments, quadrupole moments, or polarizabilities [37, 38]. For instance, an ion-molecule cluster formed through charge-dipole interactions includes $I^- \cdot CH_3I$ [20], $I^- \cdot CH_3Br$ [20], $I^- \cdot CH_3CN$ [39], and $CF_3I \cdot I^-$ [40]. The neutral precursors of these ion-molecule clusters have dipole moments of 1.64 [41], 1.82 [41], 3.92 [42], and 1.048 Debye (D) [43]. Additionally, charge-quadrupole interactions are exemplified by $I^- \cdot CO_2$ [44], where CO_2 has a quadrupole moment but no dipole moment. Lastly, charge-polarizability interactions are illustrated in the study of $I^- \cdot C_6F_6$ [45].

Over the past few decades, there has been significant interest in the dissocia-

tion of ion-molecule clusters triggered by electron transfer following photoexcitation [46, 20, 47, 48, 39, 49, 50]. This area of study is interesting because it includes a variety of processes, such as the photoexcitation of ion-molecule clusters, the subsequent electron transfer to neutral molecules which generates molecular anions, and the dissociation of ion-molecule clusters while in the charge transfer excited state.

Cyr *et al.* [20] carried out the groundbreaking experiment on electron transfer induced dissociation on $I^- \cdot CH_3I$. In their study, they investigated the transient negative ion state by monitoring the production of the dissociating ions while varying the photoexcitation wavelength. The charge transfer mechanism can be written as:

$$I^- \cdot CH_3I + h\nu \rightarrow I \cdot [CH_3I]^- \rightarrow I + CH_3 + I^- \tag{1.5}$$

where $I \cdot [CH_3I]^-$ was identified as a charge-transfer excited state of the ion-molecule cluster $I^- \cdot CH_3I$. In the charge transfer phenomenon, $[Ch_3I]^-$ is unstable and readily dissociates through DEA to form I^-. However, verifying the intracluster charge transfer process in the symmetric $I^- \cdot CH_3I$ complex is challenging. To confirm the existence of a charge-transfer excited state, the authors extended their photoexcitation studies on the asymmetric systems $I^- \cdot CH_3Br$ and $I^- \cdot CH_2Br_2$. The authors observed Br^- fragments from both complexes, indicating that the C−Br bond indeed broke upon photoexcitation. This observation supports the existence of a charge-transfer excited state. Additionally, the authors reported the vertical detachment energies (VDE) for these systems. The VDE for $I^- \cdot CH_3I$ and $I^- \cdot CH_3Br$ was approximately 3.4 eV, while for $I^- \cdot CH_2Br_2$, it was around 3.5 eV.

In their photodissociation studies, a single photon with an energy of 3.5 eV was used for all three systems. This 3.5 eV photon can produce an electron nearly zero kinetic energy, which is then captured by the complexes and leads to the formation I^-

and Br^- fragments. Notably, that in DEA to CH_3I [51], CH_3Br [52], and CH_2Br_2 [53], both I^- and Br^- exhibit peak around 0 eV electron energy, indicating a resonance at this energy. It would be fascinating to explore scenarios where electrons carrying more energies are transferred to the molecule in charge transfer mechanism, accessing different resonance positions at higher energies. This could result in the production of different fragments from different resonance positions, aligning with the DEA study. In chapter 3, we will discuss the results of such a study, where the ion-molecule complex $CF_3I \cdot I^-$ absorbs multiple photons. This process allows the transfer of electrons at different energies, accessing different TNI states and dissociating through various channels.

1.4 Multiphoton Dissociation

Multiphoton ionization is a powerful technique used to investigate excited atomic and molecular states that may be either accessible or inaccessible through traditional spectroscopic methods [54]. This technique has a wide range of significant applications across various fields. It is employed in laser-induced plasma generation [55, 56], chemical diagnostics [57, 58], and chiral recognition [59]. Additionally, multiphoton ionization plays a crucial role in laser-filamentation [60, 61, 62, 63], as well as in generating harmonic [64, 65, 66] and high-harmonic frequencies [67], and it is extensively used in photoelectron spectroscopy [68].

Over the past few decades, negatively charged species have gained increasing recognition in atmospheric [69, 70] and interstellar environments [71, 72, 73]. However, experimental studies on the multiphoton excitation of anions are significantly less abundant compared to those for atoms and molecules. Multiphoton excitation has been primarily applied to induce electron detachment from atomic and molecu-

lar anions. In 1965, the first experimental measurements for two-photon detachment of the electron from the I^- anion were performed [74]. Interest in the study of anions grew significantly only toward the late 1980s, marked by various measurements involving halide anions [75]. In 1991, the first measurements on above-threshold detachments were performed using a Nd:YAG laser with intensities greater than 10^{12} W/cm^2. These studies observed the detachment process involving the absorption of two excess photons in anions such as F^- [76], Au^- [77], and Cl^-[78]. On the other hand, for molecular anions, Rosenfeld *et al.* [79] reported multiphoton electron detachment of the benzyl anion using a CO_2 laser. Their study predicted a coupling between vibrational excitation, triggered by the absorption of seven IR photons, and electronic degrees of freedom, indicating a violation of Born-Oppenheimer approximation. This finding is in contrast to single-photon photodetachment, which is generally considered a Born-Oppenheimer electronic transition subject to dipole selection rules [80]. More recently, Mann *et al.* [81] investigated resonant two-photon detachment of WO_2^- in the energy range $1.75 - 2.41$ eV using a Nd:YAG pumped OPO system. In their study, the authors identified two valence-bound excited states of the anion. However, to the best of our knowledge, the study of multiphoton absorption in ion-molecule clusters to investigate their fragmentation patterns has not yet been explored.

1.5 Organization of the Thesis

The aim of the study is to gain a deeper understanding of the fragmentation of molecular anions. We will examine two types of molecular anions: the first one is the conventional or valence-bound anion, where the electron attaches to the molecule's valence orbital and forms TNI. The second type is the non-valence binding anion,

where an I^- anion binds with various molecules that have dipole moments, quadrupole moments, or polarizability, forming an ion-molecule cluster. Since most anions hold their outermost electrons less tightly than most neutrals and cations, stable anions are challenging to produce, control, and study. Therefore, generating them in substantial quantities presents significant experimental challenges. To overcome these challenges and study these molecular anions, we used two different experimental apparatus, each designed to address specific aspects of anion formation and fragmentation.

We have developed an apparatus in our laboratory designed to generate, manipulate and analyze ion-molecule clusters. The apparatus consists of three chambers: source, TOF, and detection. In the source chamber, a gas mixture is expanded into vacuum through a pulsed valve and intersected by a continuous electron beam, generating ion-molecule clusters via electron ionization. The TOF chamber houses a TOF mass spectrometer, ion optics, and a mass filter. These components guide, focus, and separate anions of different masses, allowing for the mass selection of the ion-molecule cluster. Following mass selection, the ion-molecule clusters are photoexcited with a laser pulse, triggering photofragmentation in the detection chamber. A reflectron TOF mass spectrometer is used to reverse the trajectories of the anion fragments to be mass-selected and detected by a channel electron multiplier (CEM) detector. Simultaneously, neutral fragments are detected by a separate CEM detector in coincidence with the fragment anions.

We utilized an apparatus located at Lawrence Berkeley National Laboratory to image the three-dimensional momentum distribution of negative ions produced through DEA to molecular targets. The experimental setup consists of three components: a low-energy pulsed electron gun, an effusive molecular target, and a momentum imaging spectrometer. The momentum imaging spectrometer is composed of a pulsed ion extraction field, an electrostatic lens, and a time- and position-sensitive detector.

It measures the time of flight and position of each ion, enabling the imaging of the full 4π solid angle momentum sphere. The kinetic energy and angular distributions of the ions will be retrieved from the momentum distributions. The kinetic energy distribution provides insights into the state of the neutral fragment and the dynamics involved in the dissociation process. It helps us understand how energy is partitioned during the breakup of the molecule. The angular distribution can reveal information about the the electronic symmetry of the molecular state involved in the dissociation. This setup enabled precise analysis of anion fragment dynamics and energies resulting from DEA processes.

In this thesis, we will detail an experimental setup specifically designed to examine the dissociation dynamics of mass-selected ion-molecule clusters in their excited states. This apparatus allows the detection of the resulting photofragments, including both fragment anions and neutrals. Following this, we will discuss the experiment conducted using this apparatus, where the $CF_3I \cdot I^-$ ion-molecule cluster was photoexcited with 400 nm UV femtosecond laser pulses. In this experiment, the absorption of multiple photons initiates the formation of photofragments. In addition to finding the number of photons absorbed during fragmentation, we will compare the experimental results with those from the single-photon excitation case and DEA to CF_3I to understand the formation of TNIs and subsequent dissociation channels. We observed different fragmentation channels following different number of photons absorption.

We will also present the results from the DEA experiments conducted with the 3D anion momentum imaging apparatus at Lawrence Berkeley National Laboratory. This study focuses on the dissociation channels of acetic acid and its partially and fully deuterated analogues, specifically those leading to H^-/D^- ions. Our investigation has identified three resonance positions corresponding to O−H and C−H bond cleavage. Additionally, we have observed a fourth, previously unreported resonance position,

which we attribute to O-H bond break.

Furthermore, we will present direct measurements of the anion fragment yields and kinetic energies resulting from the DEA to 1-M-5-Nitroimidazole. These experimental data are crucial for accurately simulating electron-induced radiation damage in biological systems containing 1M5NI.

The thesis is organized into the following five chapters. The second chapter details the experimental setup of the ion-molecule cluster, including the methodologies for data acquisition and analysis. Chapter 3 discusses the multiphoton studies of the ion-molecule cluster $CF_3I \cdot I^-$. The fourth and fifth chapters focus on the Dissociative Electron Attachment (DEA) studies. Chapter 4 presents the DEA results for acetic acid exploring its dissociation dynamics. Chapter 5 expands this investigation to 1-Methyl-5-Nitroimidazole. In chapter 6, we provide concluding remarks.

Chapter 2

Experimental Setup for Cluster Anion Photodissociation

2.1 Introduction

We have developed an apparatus in our lab to study the excited-state dissociation dynamics of cluster anions. Following the photodissociation, the anion fragments are mass-resolved and detected in coincidence with the neutrals. Compared with the existing tandem mass spectrometer that detect anion fragments and neutrals [82, 46, 47, 83], our apparatus introduces two improvements [84]:

(i) Higher repetition rate: By utilizing a pulsed nozzle and continuous electron beam, the system is capable of operating at up to 500 Hz, although currently it is limited to 200 Hz due to pumping speed constraints.

(ii) Compact design: The integration of a short TOF spectrometer, a three-electrode mass gate, a compact linear and quadratic reflectron mass spectrometer, and two channel electron multipliers (CEMs) significantly reduces the overall size.

In this thesis, this combination is employed for multiphoton studies of cluster anions, accessing different excited states that leads to different fragments. In the near future, when equipped with electron imaging techniques such as velocity map imaging (VMI), it can lead to time-dependent studies by introducing a second laser pulse to probe the excited anions in real time and measurement of photoelectrons.

The major modules of the cluster anion beam apparatus are: (i) generation of high repetition rate molecular anion pulses, (ii) separation, acceleration, and selection of the target molecular cluster anion, (iii) ultrafast UV lase pulse generation from the fundamental to excite the parent anion, and (iv) detection of anion fragments and neutrals. A more detailed description of the apparatus can be found in [85, 84]. We will start with an overview of the experimental setup.

2.2 Overview of the Experimental Setup

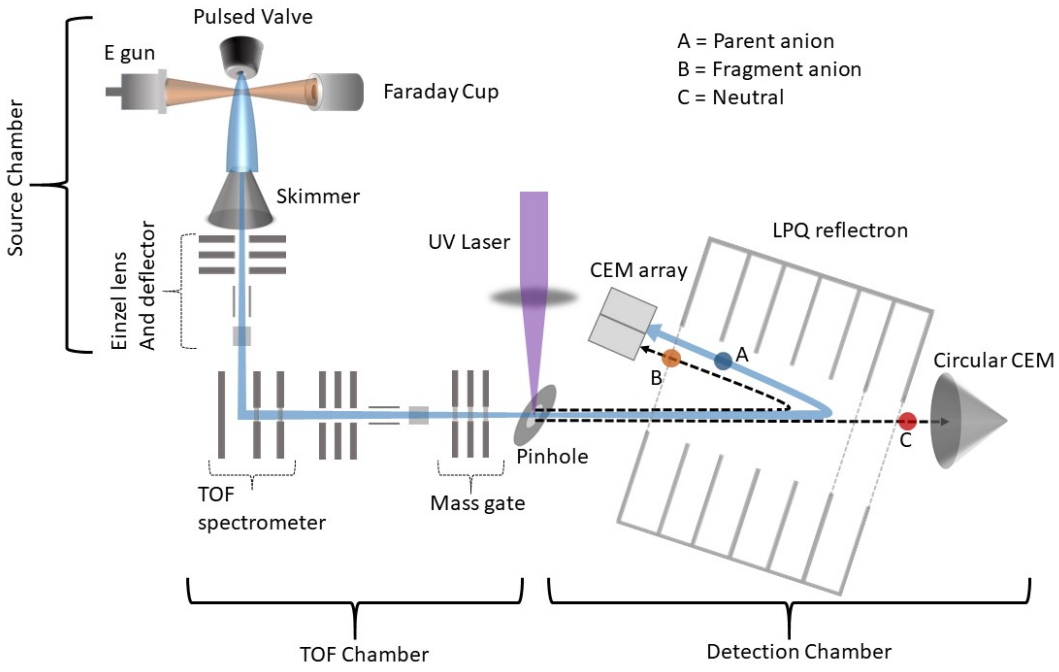

Figure 2.1: Overview of the main components of the experimental apparatus in source, TOF, and detector chambers.

In this section, we will give a brief review on the experimental apparatus and its elements as shown in Fig 2.1.

The source chamber houses a homemade Pierce-type electron gun [86], a duel Faraday cup, an Evan-Lavie pulsed valve [87], a copper skimmer, and ion optics used

to guide the ions to the next chamber. The electron gun and the pulsed valve are oriented in a perpendicular configuration. The continuous electron gun ionizes the gas jet produced by the pulsed valve, generating ions, and ion clusters. The generated ions pass through the copper pinhole. A focusing lens focuses while a pair of deflectors guides them into the TOF chamber.

A Wiley-Mclaren type TOF mass spectrometer [88] separates ions of different masses in time by extracting and accelerating the ion pulses perpendicular to the initial ion beam axis from the source chamber. The ion pulses then pass through a second focusing lens and a second pair of parallel-plate deflectors. A pulsed mass gate then selectively transmits only the target molecular cluster ion.

In the detection chamber, the focused molecular cluster anions are photoexcited by a UV laser pulse propagating perpendicularly at the interaction region. To ensure spatial overlap between the anion beam and the laser, a copper pinhole is positioned at the interaction region. Temporal overlap is achieved through a laser-anion pulse synchronization system. After photoexcitation, a linear plus quadratic (LPQ) reflectron TOF spectrometer is employed to mass-resolve the anion fragments. The LPQ reflectron reverses the trajectory of both parent and fragment anions, which are subsequently captured by two Channel Electron Multiplier (CEM) detectors. The neutral fragments pass through the LPQ reflectron undeflected and are detected by a separate CEM detector.

Section 2.3 of this chapter will concentrate on anion beam generation through the interaction with molecular beam and a continuous electron beam. In Section 2.4, we will explain how the TOF mass spectrometer, ion optics, and mass gate are used to extract, accelerate, and mass-select the target cluster anion. In Section 2.5 , we will discuss the design and SIMION simulation of the reflectron TOF mass spectrometer. Section 2.6 will cover the generation and characterization method of the laser pulse

as well as the overlap scheme of laser and anion pulses at the interaction region. Finally, we will discuss the data acquisition and analysis of the photofragmentation of $CF_3I \cdot I^-$ in Section 2.7.

2.3 Ion Beam Generation

An effective way to prepare charged clusters is to use a combination of pulsed nozzle and a high energy electron beam (∼1keV). A pulsed free expansion from a pulsed valve can provide high neutral densities and create a vibrationally, rotationally, and translationally cooled supersonic beams [89, 90]. The pressure in the gas reservoir or in the pulsed valve can be several atmospheres where as the pressure in the chamber is a vacuum ($\sim 10^{-8}$ torr) during the experiment. Because of the pressure difference, the gas will adiabatically expand (i.e. no energy will be transferred by heating or cooling during the process), and the free enthalpy and the thermal kinetic energy will be transferred into their kinetic energy in the beam propagation. For the adiabatic expansion at constant enthalpy, the following relation is valid [89, 90]

$$C_pT + \frac{1}{2}mv^2 = \text{constant}, \tag{2.1}$$

where m is the molecular mass, C_p is the specific heat capacity of the gas at constant pressure, v is the velocity, and T is the temperature. Now if T_0 is the temperature of the gas reservoir before the valve, then the above equation can be written according to the conservation of energy [89, 90]:

$$C_pT + \frac{1}{2}mv^2 = C_pT_0. \tag{2.2}$$

Using Eq. 2.2 and the standard thermodynamic relations for an adiabatic expansion, the temperature T of the expanding gas after the valve can be written as:

$$T = \frac{T_0}{1 + \frac{\gamma-1}{2}M}, \tag{2.3}$$

where γ is the molar specific heat capacities and M is the Mach number of the expanded gas which can be approximated as [89, 91]:

$$M \approx \left(\frac{\gamma+1}{\gamma-1}\right)^{\frac{\gamma+1}{4}} \left(\frac{x}{d}\right)^{\gamma-1}, \tag{2.4}$$

where x is the distance from the valve opening, d is the opening diameter. As the distance x from the opening increases, M also increases in Eq. 2.4, thus decreasing the temperature of the expanding gas according to Eq. 2.3. In the experiment, molecules under study are seeded in carrier gas such as Ar and therefore the velocity and the amount of cooling can be approximated by the velocity and cooling of the career gas.

In our experimental setup, we used an Even-Lavie (EL) pulsed valve [87] with an aperture of 100μm. A gas mixture containing 98.7% Ar and 1.3% CF_3I, pressurized at 100 psi, was delivered to the EL pulsed valve. Following supersonic expansion, this gas mixture was intersected perpendicularly by a focused, continuous electron beam with an energy of 800 eV. The pulsed valve operated at 200 Hz. Under this condition, the pressure inside the source chamber was maintained $4 - 5 \times 10^{-5}$ Torr, while the pressure in the electron gun side was $2 - 3 \times 10^{-6}$ Torr.

The initial interaction between 800 eV electrons and the supersonic expanding gas produces small positive ions and low energy secondary electrons [46], resulting in the formation of an electrically neutral plasma. This electron rich plasma is the key to the effective formation of the cluster anions in the high density region where many

ion-neutral reactions take place. In our case, this process can be described as follows [40, 82]:

(i) Argon is a very good source of low energy electron upon electron impact through ionization. This low energy electron will be captured by the CF_3I molecule through dissociative electron attachment, resulting in the production of I^- as follows:

$$e^- + CF_3I \rightarrow CF_3 + I^-$$

(ii) CF_3I condensates onto I^- because of the long-range charge-dipole interaction to form $CF_3I \cdot I^-$ in the most dense part of the plasma.

$$CF_3I + I^- \xrightarrow{\text{condensation}} CF_3I \cdot I^-.$$

A camera placed at 45° to both the electron beam and pulsed molecular beam in the system captures the fluorescence of the interaction of the electron and gas mixture in real time. This helps us to monitor the overlap between the two beams. The size of the overlap region is found to be 2.13×2.95 mm at the FWHM and is found by fitting a two dimensional Gaussian to the image.

The anions generated at the interaction region are passed through a flared-conical copper skimmer with an entrance diameter of 3 mm, which selects the most intense part of the anion beam and also helps to maintain the differential pumping between source and TOF chambers. Following the skimmer, the anions are guided and focused at the entrance of the TOF spectrometer with a pair of parallel plates and an einzel lens.

2.4 Focusing, Ion Optics, and TOF Mass Spectrometer

Our objective is to temporally disperse the anions of different masses and accelerate and focus them at the interaction region. The Wiley-McLaren [88] type TOF mass spectrometer consists of three electrodes parallel to each other, namely repelling, extraction, and ground. It extracts and accelerates the anion beam in a direction perpendicular to the incoming beam from the source chamber. A second einzel lens and a second pair of parallel deflectors are used to focus and steer the anion beam. Additionally, we want to optimize the voltages of different components so that a focused beam of smaller temporal length at the interaction region is obtained.

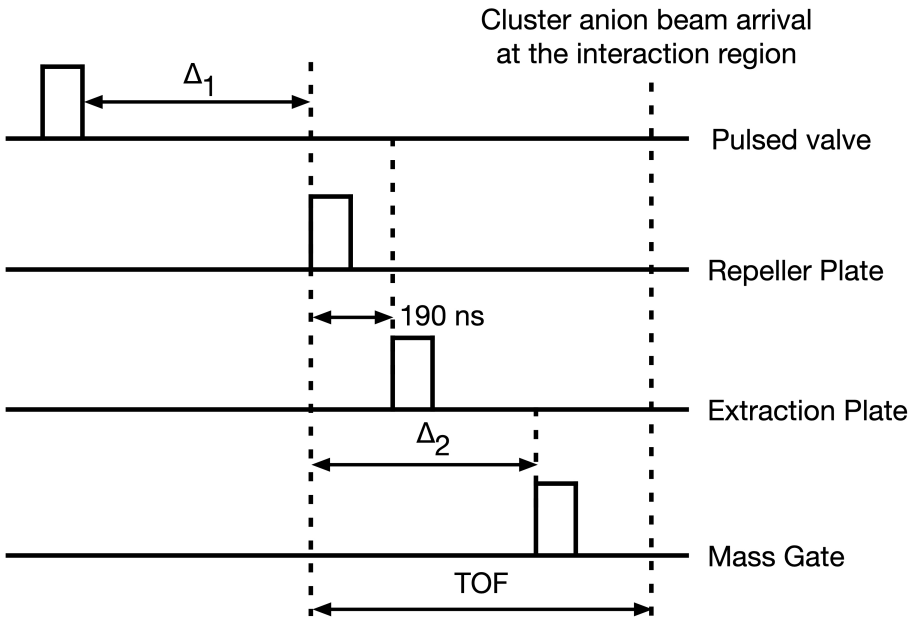

Figure 2.2: Timing scheme to optimize the cluster anion beam at the interaction region.

The timing scheme in Fig. 2.2 is designed to optimize the temporal width of the anion beam at the interaction region. The pulsed valve, operating at 200 Hz, triggers the repeller and extraction plates of the TOF mass spectrometer, while the mass gate is triggered with respect to the repeller plate. The flight time of the anion beam from

the valve to the extraction region, denoted as Δ_1, is varied to maximize the counts of anion beam, particularly those of the target cluster anion. High voltage pulses of -3000 V and -2535 V are applied to the repelling and extraction electrodes, respectively. A delay of 190 ns is applied to the extraction electrode relative to the repeller electrode. This constant delay eliminates most of the energy spread introduced by the initial energy of the ions and reduced the duration of the cluster ion pulses to around 100 ns (FWHM) [85]. In this case, the pulse duration for which the high voltage was applied to repeller and extraction electrode was 4 μs. We can further correct the initial energy spread and reduce the duration of the cluster anion pulse by reducing the pulse duration to 2.258 μs.

A constant potential of -1515 V is applied to the middle electrode of the einzel lens to focus the cluster anion pulse transversely. The potentials on each pair of deflector's electrode, used to steer and correct the small initial transverse velocity component of the cluster anion pulse, are $(0\ \text{V}, -16\ \text{V})$ and $(0\ \text{V}, 225\ \text{V})$, respectively. The CEM array is placed temporarily at the interaction spot, 67 cm downstream from the ground electrode, to record the TOF spectra of the cluster anion along with other anions.

A floating high voltage pulse of -3000 V is applied to the middle electrode of the mass gate, while the outer two electrodes are grounded. The adjustable delay, Δ_2 in Fig. 2.2, determines which anion pulse to select. To select the target cluster anion $CF_3I \cdot I^-$, a delay of 16.59 μs is used. Therefore, after 16.59 μs, the voltage on the middle electrode of the mass gate will go to zero for 1 μs, allowing the cluster anion $CF_3I \cdot I^-$ to pass through undeflected, retaining its TOF spectrum and temporal shape.

Fig. 2.3 shows the TOF spectrum as well as the Gaussian fit of the $CF_3I \cdot I^-$ anion at the interaction region generated using a mixture of Ar and CF_3I. The pulse

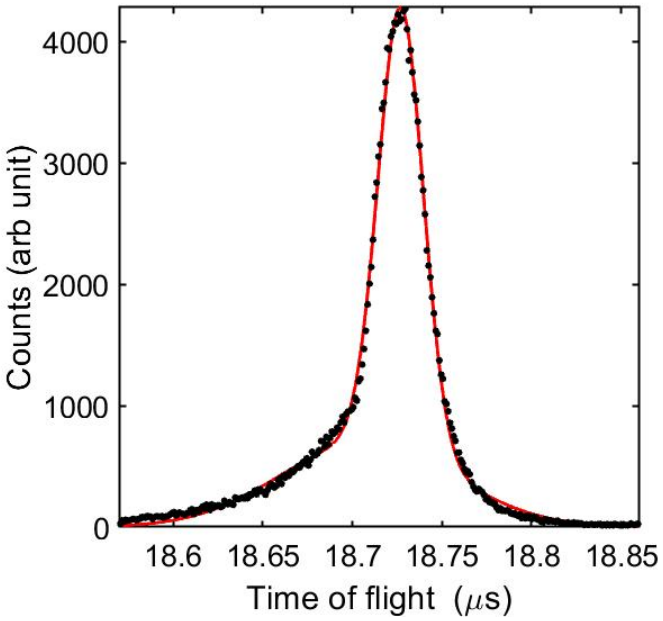

Figure 2.3: TOF spectrum of the cluster anion $CF_3I \cdot I^-$ pulse at the interaction region.

duration of $CF_3I \cdot I^-$ is measured as 34 ns at FWHM by fitting a Gaussian to the spectra. This is an improvement from previous measurement (around 80 ns) [85].

The definition of the mass resolution according to the International Union for Pure and Applied Chemistry given in [92] is: "For a single peak made up of singly charged ions at mass m in a mass spectrum, the resolution may be expressed as $\frac{m}{\Delta m}$, where Δm is the width of the peak at a height which is a specified fraction of the maximum peak height. It is recommended that one of the three values of 50%, 5%, and 0.5% should always be used."

The relation between the TOF t and molar mass m of a particular ion can be described as $t \propto \sqrt{m}$ [93]. Therefore, the resolution $m/\Delta m$ can be written as following :

$$\frac{m}{\Delta m} = \frac{t}{2\Delta t}, \tag{2.5}$$

where Δt is the pulse duration at FWHM of the ion peak of mass m. The mass resolution for the cluster anion $CF_3I \cdot I^-$ peak with $t = 18.73$ μs and $\Delta t = 34$ ns (FWHM), thus becoming 275.

After the optimization of the cluster anion $CF_3I \cdot I^-$ at the interaction point is done, the CEM array is replaced by a copper pinhole. Some minor adjustment of the voltages especially the deflectors is needed to guide the mass selected $CF_3I \cdot I^-$ beam through the pinhole.

2.5 Design of Reflectron Time-of-Flight Mass Spectrometer

2.5.1 Design Perspectives

The TOF mass spectrometer accelerates the mass-selected parent anion to a few thousand eV. Upon photoexcitation of the parent anion, the resulting fragment anions maintain the same speed as the parent anion but possess different kinetic energies, ranging from a few hundred eV to a few thousand eV. To discriminate between the parent and fragment anions following photoexcitation, a reflectron type mass spectrometer is employed.

The most common type of reflectron is the linear reflectron [94]. The voltages inside this reflectron are varied linearly using the relation $V = ax$, where x is the depth of the reflectron. There are two time focus positions: the first at the interaction region and the second at the detector. This is achieved when the ions spend an equal amount of time in the drift and reflectron regions and satisfy the condition $L_1 + L_2 = 4d$, where L_1 and L_2 are the two drift regions before entering and exiting the reflectron, and d is the penetration depth at which the ions turn around. This design is not particularly useful for photodissociation studies. After photoexcitation with the laser of the parent ion, fragment ions will have same velocity as the parent ion but different

energy depending on fragment ion mass-to-charge ratio (m/z). The second time focus positions for the parent and fragment ions differ as the penetration depth changes for parent and fragment ions. This results in the gradual decline of the fragment ion resolution as m/z decreases [93].

The kinetic energy correction or the fragment ion time focusing can be achieved if the voltage inside the reflectron is varied quadratically [95] and is called curved field or parabolic reflectron. Here, the voltages are varied using the law: $V(x) = ax^2$, where x is the depth of reflectron. In this design, the time-of-flight (TOF) of an ion inside the reflectron is independent of energy [95]. The reflectron is designed in such a way that there are no drift regions, i.e., both the time focus positions will be at its entrance. It is difficult to implement the design experimentally as the design requires both the interaction region and detector to be placed as close to the reflectron entrance as possible.

A large enough drift region in between the interaction region and the reflectron entrance is advantageous in photodissociation studies. The fragmentation process starts at the time of photoexcitation and may extend to the time when the parent ions reach the detector, namely prompt and metastable fragmentation. In prompt fragmentation, the fragment ions will be produced at the time of photoexcitation and will be detected as separate peaks. On the other hand, metastable fragmentation occurs at a later time in three regions: (i) before entering the reflectron, (ii) inside the reflectron, and (iii) after exiting the reflectron. As long as the fragmentation occurs before entering the reflectron, the fragment ions will have different TOFs and will appear as separate peaks. Fragmentation that happens inside the reflectron will add to the chemical noise (unwanted fragment signal), whereas those occurring after exiting the reflectron with the same velocity as the parent ion will not contribute to the fragment ion spectra.

2.5.2 Objectives

When designing the reflectron TOF mass spectrometer, there were four goals to be achieved. First, the instrument needed to be compact (< 7 cm in length) so that it can be accommodated within the detection chamber. Second, the apparatus should have a high mass resolution and should be capable of operating over a large mass range. This would allow for the identification of fragment anions from parent anion after photoexcitation, and an ideal one would be the one that could resolve unit mass changes in fragments. Third, the temporal focus position should not change for different masses having different energy. This would permit the identification of different fragment masses without changing the detector position. Last, the circuit design should be such that only one adjustable knob would be needed to change the voltages in each electrodes. Therefore, only a single voltage source would be sufficient for the reflectron operation during the experiment.

To meet the various requirements of our experimental set-up, we chose to vary the voltage inside the reflectron having both linear and quadratic components. Such a design was first proposed by Yoshida [96] and then later adopted in [97].

2.5.3 Theory of Reflectron

Following the treatment of [96], let V_n be the voltage applied to nth electrode at a distance X_n. The voltage V_n applied can be represented as the sum of quadratic voltage V_q (varies as the square of the distance X_n) and linear voltage V_l (varies in proportion to the distance X_n) and is given by the equation:

$$V_n = V_q + V_l \tag{2.6}$$

with,

$$V_q = \frac{1}{2} a {X_n}^2 \tag{2.7}$$

$$V_l = bX_n. \tag{2.8}$$

V_n in terms of parameters $X_n, a \quad \text{and} \quad b$ can be represented as,

$$\begin{aligned} V_n &= V_q + V_l \\ &= \frac{1}{2} a {X_n}^2 + bX_n. \end{aligned} \tag{2.9}$$

The electric field E inside the reflectron can be written as $E = \frac{\mathrm{d}V}{\mathrm{d}X}$. (sign has been ignored as it will depend on the polarity of DC voltage and the choice of particle).

$$\begin{aligned} E &= \frac{1}{2} a \; 2(X_n + \frac{b}{a}) \\ &= aX_n + b. \end{aligned} \tag{2.10}$$

Therefore, the electric field E has only one component, proportional to the distance X_n as well as a constant term.

Consider the parent ion of charge, q and mass, m has kinetic energy, E_k and initial velocity, v_0 then

$$v_0 = \sqrt{\frac{2qE_k}{m}}. \tag{2.11}$$

If the ion has a spread in energy, it can be expressed as the spread in initial velocity.

Now let's consider the distance between the interaction region and the reflectron

entrance as d_1 and d_2 as the distance between the reflectron entrance and the detector. The ion moves in a field free region in d_1, and d_2 as there is no electric field affecting the velocity. As the velocity will be constant, the time of flight T_1 can be written as

$$T_1 = \frac{d_1 + d_2}{v_0} = (d_1 + d_2)\sqrt{\frac{m}{2qE_k}}. \tag{2.12}$$

The equation of motion inside the reflectron can be written as

$$m\frac{\mathrm{d}^2 X_n}{\mathrm{d}t^2} = -qE = -qaX_n - bq. \tag{2.13}$$

Imposing the initial condition, at t_0, $X_0 = 0$ and velocity v_0, the position X_n can be written as

$$X_n = \sqrt{\frac{2E_k}{a}} \sin\sqrt{\frac{aq}{m}}t + \frac{b}{a}\cos\sqrt{\frac{aq}{m}}t - \frac{b}{a}. \tag{2.14}$$

The above equation can be modified by using:

$$\cos\theta = \frac{\sqrt{\frac{2E_k}{a}}}{\sqrt{\frac{2E_k}{a} + \frac{b^2}{a^2}}}, \tag{2.15}$$

$$\sin\theta = \frac{\frac{b}{a}}{\sqrt{\frac{2E_k}{a} + \frac{b^2}{a^2}}}, \tag{2.16}$$

and

$$\theta = \arctan(\frac{b}{a}\sqrt{\frac{a}{2E_k}}). \tag{2.17}$$

Therefore,

$$\begin{aligned} X_n &= \sqrt{\frac{2E_k}{a}+\frac{b^2}{a^2}}\ (\sin(\sqrt{\frac{aq}{m}}t)\ \cos\theta + \cos(\sqrt{\frac{aq}{m}}t)\ \sin\theta) - \frac{b}{a} \\ &= \sqrt{\frac{2E_k}{a}+\frac{b^2}{a^2}}\ \sin(\sqrt{\frac{aq}{m}}t+\theta) - \frac{b}{a}. \end{aligned} \tag{2.18}$$

Eqs. 2.7 and 2.8 can be rewritten in terms of the length of the reflectron L as,

$$V_q = \frac{1}{2}aL^2 \tag{2.19}$$

$$V_l = bL. \tag{2.20}$$

Eq. 2.18 can be written in terms of linear, V_l and quadratic V_q voltages, and the length of reflectron L as

$$X_n = L\sqrt{\frac{E_k}{V_q}+\frac{{V_l}^2}{(2V_q)^2}}\ \sin(\sqrt{\frac{2qV_q}{mL^2}}t+\theta) - L\frac{V_l}{2V_q}, \tag{2.21}$$

with

$$\theta = \arctan(\frac{V_2}{\sqrt{4E_kV_q}}). \tag{2.22}$$

The time of flight (TOF) inside the reflectron T_2 is the time during which the ion enters the reflectron, changes direction, and exits the reflectron again giving $X_n = 0$.

Therefore, using $X_n = 0$ and $t = T_2$, Eq. 2.21 can be written as,

$$\begin{aligned} 0 &= L\sqrt{\frac{E_k}{V_q} + \frac{{V_l}^2}{(2V_q)^2}}\ \sin(\sqrt{\frac{2qV_q}{mL^2}}T_2 + \theta) - L\frac{V_l}{2V_q} \\ \frac{V_l}{2V_q} &= \sqrt{\frac{E_k}{V_q} + \frac{{V_l}^2}{(2V_q)^2}}\ \sin(\pi - \sqrt{\frac{2qV_q}{mL^2}}T_2 - \theta) \\ \frac{V_l}{2V_q} &= \frac{V_l}{2V_q}\sqrt{1 + \frac{4V_qE_K}{{V_l}^2}}\ \sin(\pi - \sqrt{\frac{2qV_q}{mL^2}}T_2 - \theta) \\ T_2 &= L\sqrt{\frac{m}{2qV_q}}[\pi - \arcsin(\frac{1}{\sqrt{1 + \frac{4V_qE_K}{{V_l}^2}}}) - \arctan(\frac{V_l}{\sqrt{4E_kV_q}})]. \end{aligned} \tag{2.23}$$

Let, $\arcsin x = \phi$; $\sin\phi = x$;$\tan\phi = \frac{x}{\sqrt{1-x^2}}$,
where, $x = \frac{1}{\sqrt{1+\frac{4V_qE_K}{{V_l}^2}}}$ and $1 - x^2 = \sqrt{\frac{4V_qE_k}{{v_l}^2+4V_qE_k}}$.
The expression for ϕ can be written as,

$$\begin{aligned} \phi &= \arctan\frac{x}{\sqrt{1-x^2}} \\ &= \arctan[\sqrt{\frac{{V_l}^2}{{V_l}^2 + 4V_qE_k}} \times \sqrt{\frac{{V_l}^2 + 4V_qE_k}{4V_qE_k}}] \\ &= \arctan\frac{V_l}{\sqrt{4V_qE_k}}. \end{aligned} \tag{2.24}$$

Eq. 2.23 becomes,

$$T_2 = L\sqrt{\frac{m}{2qV_q}}[\pi - 2\arctan(\frac{V_l}{\sqrt{4E_kV_q}})] \tag{2.25}$$

The total TOF, T is the sum of T_1 and T_2:

$$T = (d_1 + d_2)\sqrt{\frac{m}{2qE_k}} + L\sqrt{\frac{m}{2qV_q}}[\pi - 2\arctan(\frac{V_l}{.}\sqrt{4E_kV_q}]. \tag{2.26}$$

The focus condition can be achieved by differentiation Eq. 2.26 with respect to

E_k and setting equal to zero, i.e.,

$$0 = \frac{\mathrm{d}T}{\mathrm{d}E_k} \tag{2.27}$$

$$\frac{d_1 + d_2}{L} = \frac{4E_k V_l}{V_l^2 + 4E_k V_q}. \tag{2.28}$$

The above equation can be solved for V_l and after some manipulation,

$$V_l = \frac{2LE_K}{d_1 + d_2}\left[1 - \sqrt{1 - \frac{{d_1 + d_2}^2}{L} - \frac{V_q}{E_k}}\right]. \tag{2.29}$$

In the above equation d_1, d_2, and L are kept constant, i.e., the interaction region, the detector position, and the length of reflectron are fixed. For a certain value of parent kinetic energy E_k, the value of V_q and the corresponding value of V_l using Eq. 2.29 will decide the maximum value of voltage V_n that can be applied to the last electrode of the reflectron. By knowing the value of V_q and V_l, we can calculate the constants a and b using Eqs. 2.7 and 2.8 for the length of the reflectron.

2.5.4 SIMION Simulation

SIMION trajectory software [98], version 8.0, was used to test the possible design (e.g., by changing the number of electrodes, spacing between them, different maximum voltages before deciding the working design). Although the SIMION simulation is not a good replacement for an experiment, changing the different parameters is easier in a simulation environment than in the machine shop.

For the SIMION simulation, we will consider the parent ion $CH_3NO_2 \cdot I^-$ having energy 2700 eV and the fragments originating from that will have different kinetic energy depending on the mass. After photofragmentation of the parent anion, the

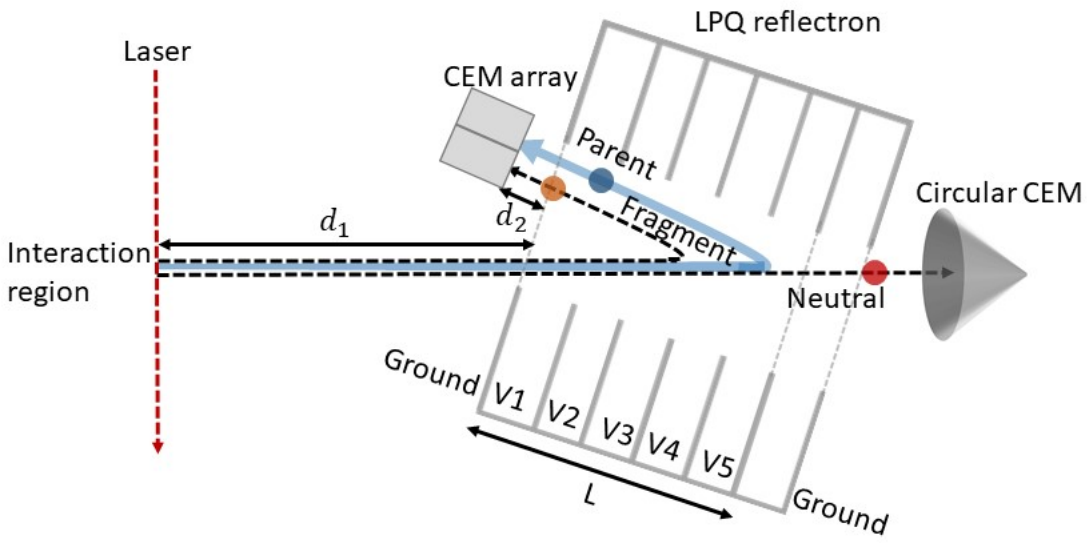

Figure 2.4: Top view of the reflectron TOF mass spectrometer.

range of fragment ion m/z can be large (e.g., for $CH_3NO_2 \cdot I^-$, it starts from 1 (H^-) and can be up to 188 for the parent anion). The reflectron should have the capability to record fragmentation spectra in that range, but it is not feasible to capture the full spectra using only a single maximum voltage at the back of the reflectron. This is due to the choice of detectors and the limitation in their sizes. The amount of bending inside the reflectron while reversing the direction for the lower m/z can be large due to higher maximum voltage and may miss the detector. Therefore, the reflectron should have the capability of operation over a large voltage range so that the smaller masses can be recorded by applying lower maximum reflectron voltage.

For SIMION simulation, we will consider the reflectron consisting of seven electrodes with 50 mm in inner diameter and the outer diameter of 100 mm as shown in Fig. 2.4. The first and last electrodes are kept grounded to avoid leaking of the electric field outside of the reflectron. The electrodes are separated by 13 mm. To find the voltages in each electrode, we will make use of the Eqs. 2.9 and 2.29 to find

V_q and V_l. For a parent anion with energy $E_k = 2700$eV, we consider applying a maximum voltage of 3000 V at the last electrode. With $d_1 = 55$mm, $d_2 = 15$mm, $L = 65$mm, $E_k = 2700eV$ in Eq. 2.29, the maximum voltage of 3000 V will be achieved for $V_q = 1307$ V and $V_l = 1693.5$ V. The ratio of linear to quadratic voltage, $R = \frac{V_q}{V_l} = 0.7718$. This ratio, R is particularly important in reflectron design for two reasons. First, if the reflectron is operated at lower voltage optimized at lower fragment m/z, the focus and trajectory will remain same as the parent anion when optimized at the parent anion's energy. In other words, the reflectron can be optimized to operate at any fragment m/z and in each case, the trajectory and focus position will remain the same as the parent anion. Second, by keeping R the same for the different fragment anion m/z, we can make a single voltage divider circuit with a fixed set of resistances. The resistances will not be changed when optimized at different m/z, and the voltages in the electrodes will change accordingly.

Our simulation begins with the optimization of linear and quadratic voltages for the parent anion $CH_3NO_2 \cdot I^-$ ($m/z = 188$). The objective is to achieve a ratio of 0.7718, after which the voltage for each electrode can be calculated using Eq. 2.9. The voltages calculated to the electrodes from V_1 to V_5 are -391 V, -886.5 V, -1486.5 V, -2191.3 V, and -3000.5 V. The reflectron is rotated by a small angle of 8°, and the detector is rotated by 16°. Fig. 2.5 shows the trajectories of the anions $CH_3NO_2 \cdot I^-$ (green), I^- (blue), and $CH_2NO_2{}^-$ (red) with a m/z of 188, 127 and 60, respectively. We assume the kinetic energy of the parent anion is 2700 ± 100 eV and the corresponding average speed is 52.62 mm/μs. A Gaussian spatial distribution is assumed for parent anion as well as the fragment anions with FWHM of 2 mm. Following photofragmentation, having the same speed as the parent anion, I^- and $CH_2NO_2{}^-$ will have different energy because of their different mass. With the highest kinetic energy, $CH_3NO_2 \cdot I^-$ will penetrate deep inside the reflectron, reverse direction,

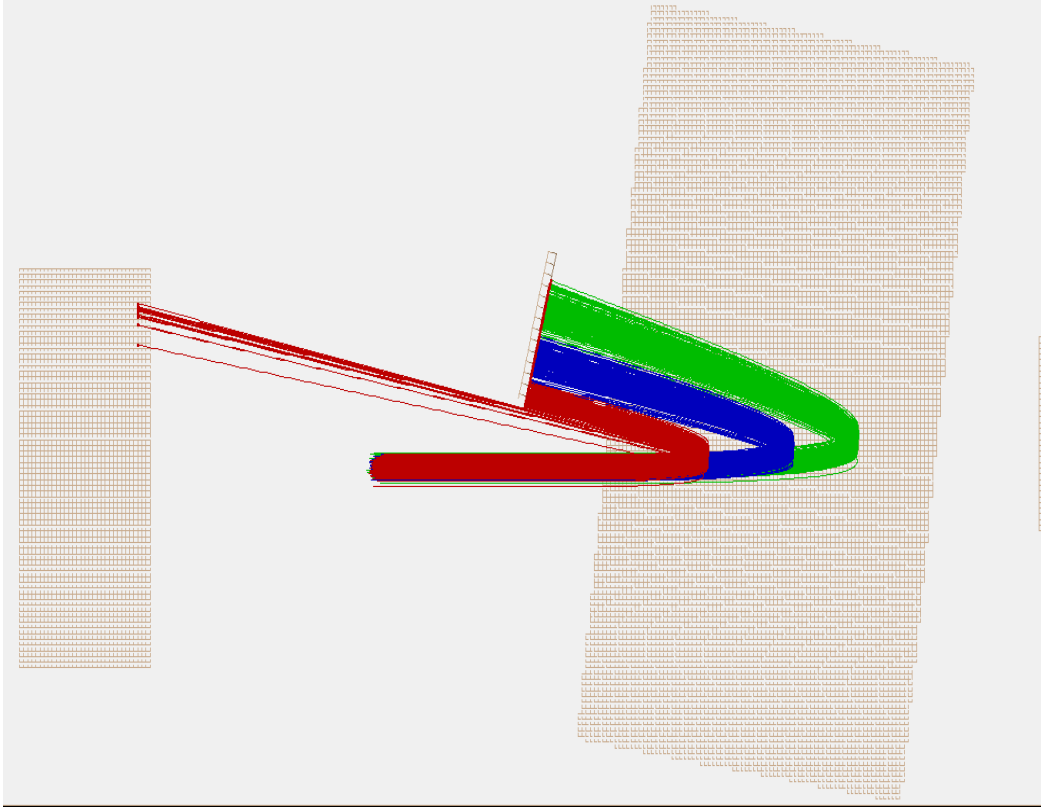

Figure 2.5: Anion trajectory simulation for the anions with $m/z = 188$ (green), 127 (blue), and 60 (red). A Gaussian spatial distribution is assumed for all the anions with FWHM of 2 mm. The potentials of -391 V, -886.5 V, -1486.5 V, -2191.3 V and -3000 V are applied to the five electrodes. The voltages are optimized for $m/z = 188$.

and arrive the detector at some TOF while the fragment anions having small kinetic energy will penetrate less deep and arrive at the detector at earlier TOF than the parent anion in TOF spectra. This is how the reflectron will separate the fragment anions in mass spectra. Here we have used a detector of 30 mm. It is evident that some of the trajectories having smaller fragments like $CH_2NO_2^-$ ($m/z = 60$) will miss the detector. Therefore, it is not possible to detect all the fragment anions of low mass with a single maximum reflectron voltage, e.g., -3000 V, at the back.

Next, we will discuss how the reflectron can be operated at lower voltages to capture the lower m/z fragments. This is one of the advantages of keeping the ratio

Table 2.1: Different voltages required to optimize the reflectron at different m/z.

m/z	E_k (eV)	V_q (V)	V_l(V)	V_n (V)	R
13	186.7	90.4	117	207.5	0.7718
37	531	257	333	590	0.7718
44	632	306	396.5	702.5	0.7717
188	2700	1307	1693.5	3000.5	0.7718

Table 2.2: The voltages at each electrode inside the reflectron when optimized (see Table 4.1) at $m/z = 13, 37, 44,$ and 188.

m/z	V_1 (V)	V_2 (V)	V_3(V)	V_4 (V)	V_5 (V)
13	-27	-61.3	-102.8	-151.5	-207.5
37	-76.9	-174.3	-292.3	-430.9	-590
44	-91.54	-207.6	-348	- 513	-702.5
188	-391	-886.5	-1486.6	-2191.3	-3000.5

R same when optimizing the voltages for different m/z's. The reflectron is optimized for three anions: the parent anion $CH_3NO_2 \cdot I^-$ (188), CH_2NO^- (44), and CH^- (13). In addition to the three anions, the reflectron is also optimized for some $m/z = 37$ to discuss the resolving power later. In Table 4.1, the voltages required to keep the ratio R same for each m/z are shown, and Table 2.2 shows the voltages in each electrode. Fig. 2.6 shows the TOF spectrum of the parent anion as well as the fragment anions with reflectron optimized at m/z: 188, 44, 37, and 13. There are two distinct features noticeable from the Fig. 2.6.

Feature I: In Fig. 2.6c, when the reflectron voltages are optimized at $m/z = 188$, the arrival time of the parent anion $CH_3NO_2 \cdot I^-$ at the detector is around 5.53 μs. The arrival time for the fragment anions at $m/z = 44$ and 13 in Figs. 2.6b and 2.6c, are similar to the parent anion case when the voltages are optimized at lower fragment anion m/z's. Therefore, the reflectron can be operated over a large mass

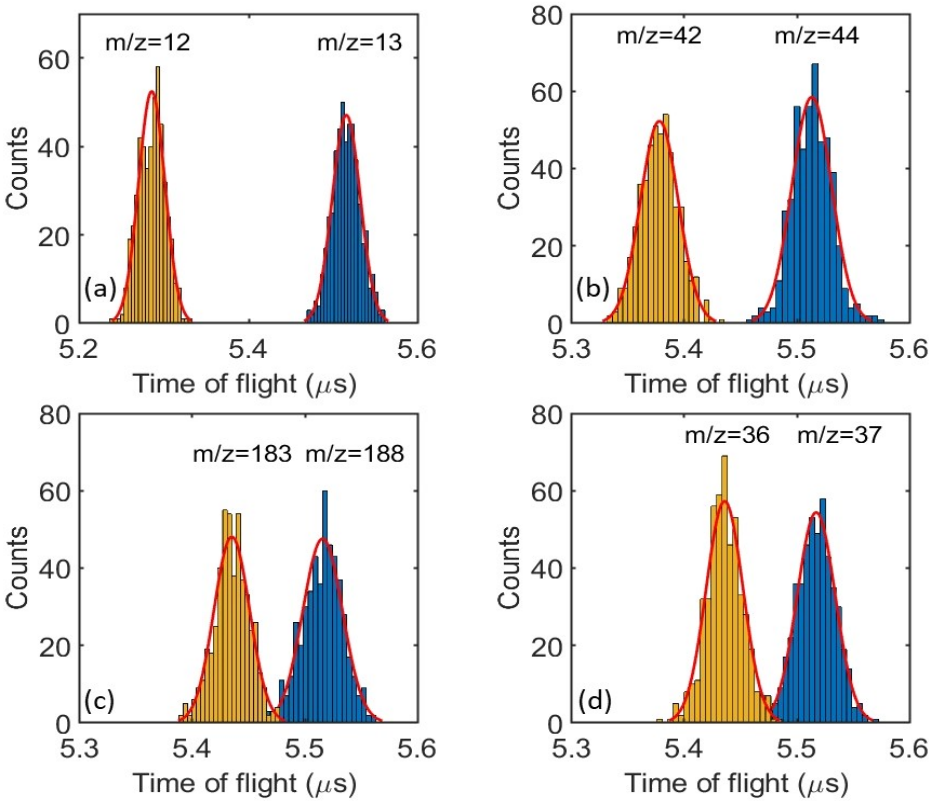

Figure 2.6: Simulated TOF spectrum of the anions where the reflectron potentials are optimized at (a) $m/z = 13$, (b) $m/z = 44$, (c) $m/z = 188$, and (d) $m/z = 37$.

range and the trajectory will be same for each m/z as long as the reflectron voltages are optimized by keeping the same ratio. This will allow detection of the fragments with any m/z.

Feature II: One can see that when the reflectron is optimized at $m/z = 13$, the separation of the adjacent m/z is large compared to optimization at $m/z = 44$. We can quantify this separation by defining a delay factor (DF) as:

$$\text{Delay factor}, DF = \frac{\text{Time delay at FWHM of adjacent } m/z}{\text{FWHM of the optimized } m/z}. \tag{2.30}$$

In Fig. 2.6a, the time delay at FWHM of $m/z = 12,\ 13$ is 192.93 ns and the delay

factor becomes 4.95. For $m/z = 42$ and 44 it is 2.24, and for $m/z = 183$ and 188 it is 1.04. Therefore a delay factor of at least 1 means two peaks are separate with minimum overlap and resolvable. When the reflectron is operated at the optimized voltage of the parent anion, a m/z difference of 5 is resolvable. But when it is operated at lower fragment m/z, it is possible to separate each mass from adjacent mass for m/z lower than 44. To be specific, for an arbitrary $m/z = 37$ in Fig. 2.6d for which the DF is 1.08, non-ambiguous detection of unit m/z separation is achievable.

We will connect the above results to calculate the resolution or resolving power of the reflectron. These terms (resolution and resolving power), commonly used interchangeably, are usually defined as $\frac{m}{\Delta m}$ [99] and is often given as a quantitative measure of the ability of a mass spectrometer to separate ions. We will use the valley definition recommended by the International Union for Pure and Applied Chemistry given in [92] and the references therein to define the resolving power: "Let two peaks of equal height in a mass spectrum of masses m_1 and m_2 be separated by a valley or overlap which at its lowest point is a stated percentage of either peak height, then the resolving power is defined as $\frac{m_1}{m_1 - m_2}$. The percentage overlap (or "valley") concerned must always be stated."

To determine the resolving power of the reflectron we will use a 5% valley definition where the two peaks are separated by a valley which at its lowest point is 5% of the height of the either peak. In Fig. 2.6c, the overlap of the mass spectrum between mass 188 and 183 is around 5%, thus yielding a resolving power of $\sim$ 37 (188/5). This is confirmed when we look at Fig. 2.6d, where the overlap of the mass spectrum between mass 37 and 36 is also 5%, resulting in a resolving power of 37. Therefore, unit mass resolution is readily apparent in SIMION mass spectra up to $m/z = 37$. However, the resolving power also depends on the flight time, initial kinetic energy of the parent anion, and initial source size at the interaction region. It can be improved

by making the length of the reflectron larger, reducing the kinetic energy of the parent anion, and making the initial source size smaller at the interaction region. The first two factors are fixed after the reflectron is designed and cannot be modified during the actual experiment. However, if the size of the source decreases, the resolving power can be large. For this analysis, we have assumed a Gaussian source with FWHM of 2 mm. The size of the laser beam in the experiment is around 200-500 μm at FWHM. Therefore, the effective source size is reduced to the size of the laser, further improving the resolving power.

2.5.5 Reflectron Circuit

As the voltages in the five electrodes inside the reflectron vary in a combination of linear and quadratic terms, we cannot simply use a constant resistance of the same value to create a voltage network for the desired electrostatic field gradient in Table 2.2. To calculate the resistances, the voltage divider formula for a circuit with two resistances R_1 and R_2 of the form,

$$V_{out} = \frac{R_2 V_{in}}{R_1 + R_2} \tag{2.31}$$

is used, where V_{in} and V_{out} are the input and output voltages. Now considering $R_t = R_1 + R_2$ to be the total resistance of the circuit, $V_T = V_{in}$ to be the max voltage in the circuit, and $V_{out} = V_i$ of the desired voltage of each electrodes, then the resistances of the electrodes $R_2 = R_i$ can be written, after rearrangement, as

$$R_i = \frac{V_i R_T}{V_T}. \tag{2.32}$$

The values of V_i and V_T are already known from simulation, deciding the total

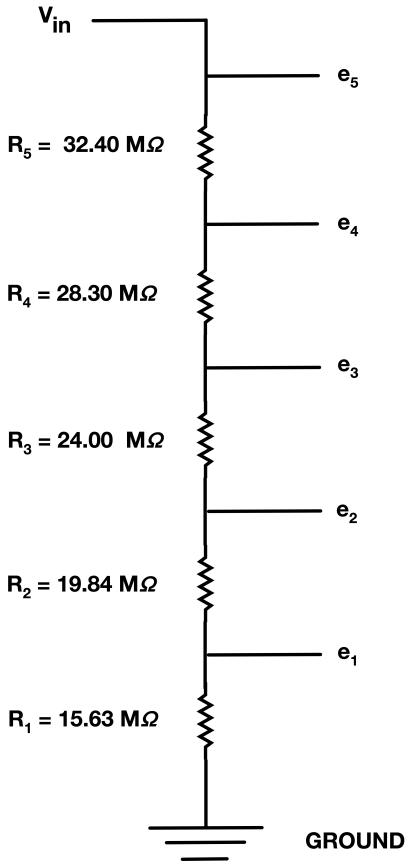

Figure 2.7: Electrical circuit for the reflectron.

resistance R_T for lower current in the circuit, values of R_i for each electrodes can be calculated. Using $R_T = 120$ MΩ, $V_T = 3000.5$ V when optimized for $m/z = 188$, $V(i) = 391$V, 886.5 V, 1486.6 V, 2191.3 V and 3000.5 V, the resistances in each electrodes are, after calculating the differences of adjacent electrodes, 15.63 MΩ, 19.84 MΩ, 24 MΩ, 28.3 MΩ, and 32.4 MΩ. The resistances in the electrodes remain the same (less than 1% variation) when optimizing for different m/z using the same ratio R of quadratic to linear voltage. Therefore the same reflectron circuit in Fig. 2.7 can be used for any m/z as long as the voltages are optimized with the same ratio.

2.6 Laser-Anion Interaction: UV Pulse Generation and Beam Crossing

In this section, we will discuss the generation and characterization of the UV laser pulse, as well as the procedure for overlapping the laser and anion beams.

2.6.1 UV Laser Pulse

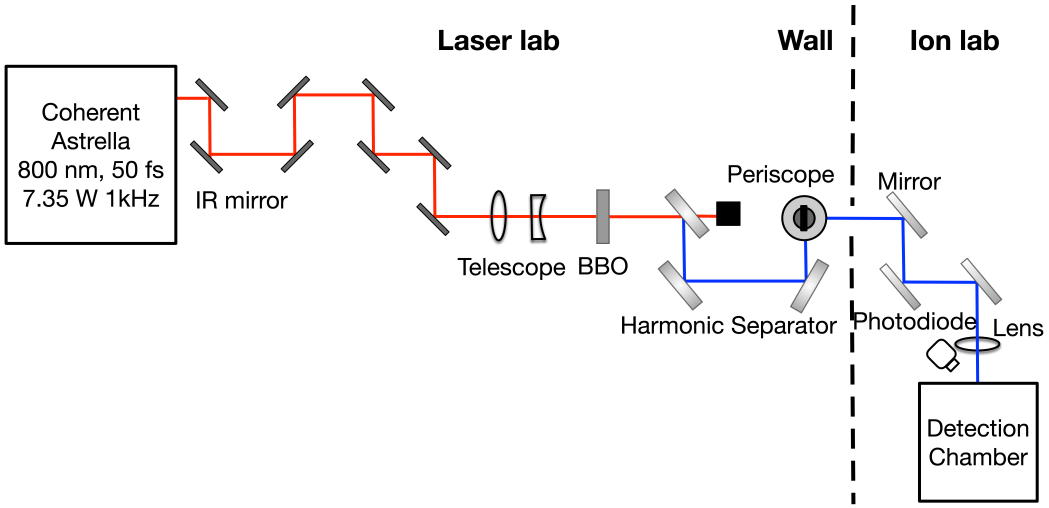

Figure 2.8: Laser optics for generating and transporting the UV laser beam.

The laser system used in our measurement is a Ti:Sapphire laser producing 50 fs pulses with up to 7 mJ energy at a repetition rate of 1kHz and a central wavelength of 800 nm. The laser optics used in our experiment is shown in Fig. 2.8. For our experiment, the laser was operated at 100 Hz repetition rate and the E.L. valve at 200 Hz repetition rate so that the pressure at the source chamber did not go beyond a certain maximum.

The UV pulses at 400 nm were generated through a nonlinear second harmonic generation crystal (a $10 \times 10 \times 0.5$ mm^3 beta-barium-borate, known as BBO) which has a polarization perpendicular to the 800 nm pulse. The fundamental is filtered

out using five harmonic separator mirrors after the BBO. A periscope in the laser lab is used to match the height of UV pulses and the anion beam in the experimental setup. The UV pulses are then transported to the optics in the ion laboratory near the detection chamber. A focusing lens of focal length 295 mm having a thickness of 2.6 mm is used to focus the beam to increase the intensity at the interaction point. The focused beam enters through a 4 mm fused silica window to the detection chamber.

A movable knife edge is used to measure the size of the UV laser beam before the lens. By incrementally blocking the laser beam and measuring the power with a power meter, the data is collected until the beam is fully blocked. Following fitting an error function to the data as a function of the position of the knife edge as illustrated in Fig. 2.9, the diameter of the UV beam before the lens is 2.2 mm at FWHM (3.74 mm at $1/e^2$). The power of the UV beam before the lens is measured with a power meter and is 84 mW at a repetition rate of 100 Hz.

The focusing lens is placed outside of the detection chamber on a linear stage, allowing for the adjustment of the laser beam size at the interaction point. Assuming a Gaussian beam profile and negligible beam divergences before the lens, the spot size at the interaction region has a diameter of 0.2 mm using the FWHM criterion (0.33 mm using the $1/e^2$ criterion). To calculate the Fourier transform-limited pulse duration, $\tau_{2\omega}$ of the 400 nm UV pulse from the BBO in terms of the pulse duration of the fundamental pulse, τ_ω, we will use [100, 101]

$$\tau_{2\omega} \simeq \frac{\tau_\omega}{\sqrt{2}} \sqrt{1 + \frac{2\ln 2}{3} \left(\frac{gL}{\tau_\omega}\right)^2}, \tag{2.33}$$

where the group velocity mismatch $g = 197$ fs/mm [102] and the thickness of the BBO crystal $L = 0.5$ mm is used in our experiment. With $\tau_\omega = 50$ fs, the pulse duration of the UV pulse after the BBO is 59 fs. Furthermore, temporal broadening

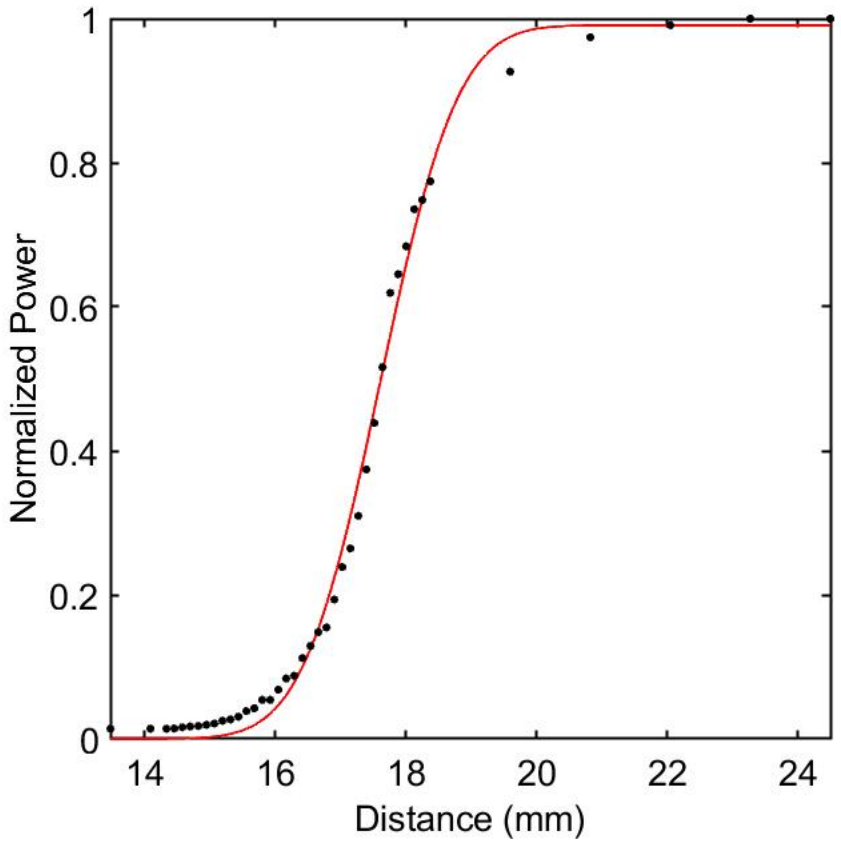

Figure 2.9: Laser beam size characterization. Red line is the fitting function and black dots are the normalized power.

can also occur by the chirp induced by the 2.6 mm fused silica lens and 4 mm fused silica optical window attached to the vacuum chamber. Therefore, the dispersion by these optical elements needs to be included for a more accurate calculation of pulse duration using,

$$\tau'_{2\omega} = \tau_{2\omega}\sqrt{1+\left(\frac{4\ln 2\ \mathrm{GDD}}{\tau_{2\omega}^2}\right)^2}, \tag{2.34}$$

where the group delay dispersion GDD is the group velocity dispersion GVD multiplied by the path length in fused silica, GDD = GVD $\times$ L_1. With GVD = 97.55 fs^2/mm [103] for 400 nm in fused silica, $\tau_{2\omega}$ = 59 fs, and the thickness of

the lens and vacuum chamber window, $L_1 = 6.6$ mm, the minimum pulse duration is 66 fs.

Now we have all the parameters needed to calculate the spatio-temporal intensity profile of the laser pulse. The spatio-temporal intensity distribution of the laser pulse assuming a Gaussian distribution is

$$I(r,t) = I_0 \exp\left[-2\left(\frac{r}{\omega_0}\right)^2 - 4\ln(2)\left(\frac{t}{\tau}\right)^2\right] \tag{2.35}$$

where I_0 is the peak intensity, ω_0 is the Gaussian beam waist (i.e., the radius using the $1/e^2$ criterion), and τ is the pulse duration. If we integrate over space and time, the energy E of each FWHM becomes,

$$E = \sqrt{\frac{\pi}{\ln(2)}}\frac{I_0 \pi \omega_0^2 \tau}{4} \tag{2.36}$$

After rearranging the peak intensity in terms of pulse energy E,

$$I_0 \simeq 1.88\frac{E}{\pi\omega_0^2\tau} \simeq 1.88\frac{P/R}{\pi\omega_0^2\tau} \tag{2.37}$$

where the pulse energy is the ratio of the average power P of the laser beam and the repetition rate R. With the UV beam of average power $P = 84$ mW, repetition rate $R = 100$ Hz, a focal size $\omega_0 = 0.0165$ cm, and pulse duration $\tau = 66$ fs, the peak intensity is $I_0 = 2.8 \times 10^{13}$ W/cm^2.

2.6.2 Spatial Overlap

The spatial overlap of the anion and laser pulses is achieved with the help of an elliptical copper aperture of size 3 mm $\times$ 4.2 mm placed at the interaction region at 45° relative to both the anion pulse and the laser pulse. We discussed the focusing

of the cluster anion beam at the interaction region in Section 2.4. After that is done, the CEM array is removed and the deflector voltages are adjusted so that maximum counts of the cluster anion through the pinhole are achieved at the circular CEM detector. The cluster anion beam therefore is focused at the interaction region and passes through the copper pinhole. The UV laser pulse is also adjusted so that it passes through the copper pinhole. This arrangement will make sure that laser-anion beams are spatially overlapped in the interaction region and very little adjustment is needed during the experiment.

2.6.3 Temporal Overlap

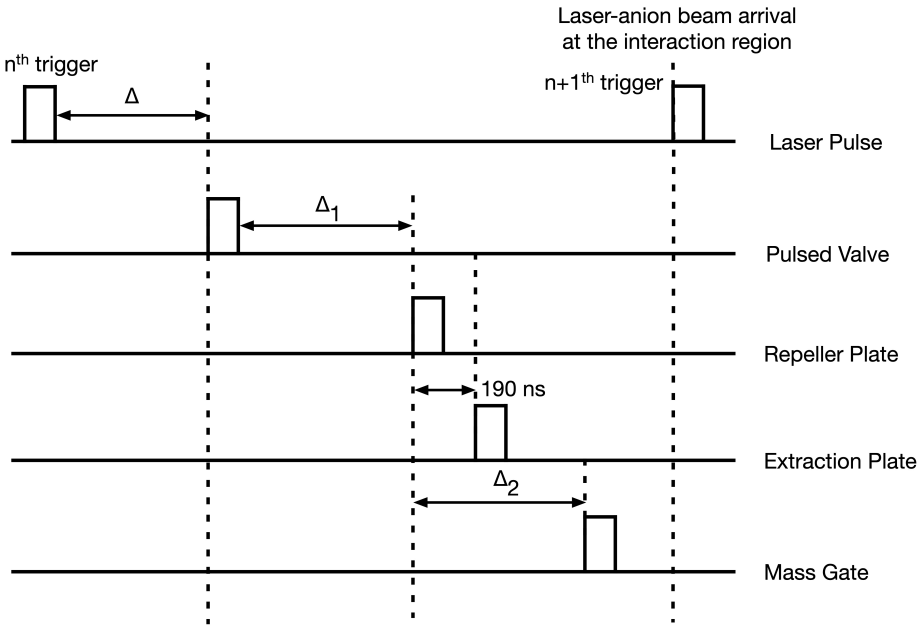

Figure 2.10: Laser-anion event timings for the photofragmentation experiment.

The temporal overlap ensures that the mass-selected cluster anion pulse arrives at the interaction spot simultaneously with the UV laser pulse. The Ti:Sapphire laser system is triggered internally by the Q-switch which serves as a master trigger of the timing scheme and runs at 100 Hz repition rate. The master trigger is doubled

to 200 Hz by combining the two outputs of the SRS DG 535 Delay Generator, with the second output delayed by 5 ms relative to the first. This 200 Hz trigger signal serves as the external trigger for the pulsed valve. When the Q-switch is triggered, the UV laser pulse arrives at the optical window after 2.67 μs, as measured by the a photodiode placed just outside the detection chamber window (Fig. 2.8). This is the n^{th} trigger in Fig. 2.10.

To achieve overlap, the arrival time of the anion pulse is delayed so that it overlap with the next laser pulse ($n + 1^{th}$ trigger in Fig. 2.10). This delay is called the laser-valve delay and is represented by Δ. The laser-valve delay Δ has to be adjusted for temporal overlap of the anion pulse and the laser pulse. The actual value of Δ is not known until the photo fragments and neutrals are observed, but an approximate Δ can be found by overlapping the signals of the UV laser pulse from the photodiode and the parent anion in the TOF spectrum. A small change in Δ affects the neutral signal and serves as an indicator for the overlap between laser and anion pulses. The rest of the timings are the same as discussed in Section 2.4.

2.7 Data Acquisition and Analysis

2.7.1 Data Acquisition and Preprocessing

We simultaneously collect data with laser on and laser off by running the nozzle at higher repetition rate than the laser. The laser is run at 100 Hz repetition rate and the pulsed valve at 200 Hz. This arrangement has particular importance during data acquisition. As the laser pulse comes to the interaction region every 10 ms and the cluster anion pulse every 5 ms, we can collect data simultaneously with laser on and laser off. The data collected with the laser on will result in neutral and fragment anions as well as the unexcited parent anion in the mass spectra. The data collected

with laser off will only have the parent anion in the mass spectra. Simultaneously taking data with and without laser will take into account any variation in the cluster anion beam current during the experiment. A separate set of data is also taken with the laser on but the pulsed valve off to account for the laser background in the TOF spectra.

TOF spectra are acquired using the RoentDek TDC4HM time-to-digital converter (TDC) card with 4 channels. The TDC converter has 0.5 ns resolution with no dead time. In our experiment, both the neutral and fragment anions are detected with CEM detectors. For the neutral detection, a circular CEM with a diameter of 10 mm is used, while for the anion detector two rectangular detectors each having a dimension of 5 mm $\times$ 15 mm are used. The two rectangular CEMs (namely upper and lower) are stacked together to make 5 mm $\times$ 30 mm, called the CEM array, to increase the detection area. So, there are three signals from the three CEM detectors that need to be processed. The first three channels of the TDC card are dedicated to the three signals from the circular and two rectangular CEM detectors to collect data. These signals are amplified by a pre-amplifier (SR240A, SRS). Signals are then discrimination by a constant fraction discriminator (21X4141, Lawrence Berkeley Laboratory). The TOF spectra are recorded for each laser on and laser off shot that are separated in post processing. Using the COBOLD data acquisition and analysis program, the TOF data was read and visualized in real time as well as stored for further analysis.

2.7.2 Data Analysis

Our goal is to get the background subtracted TOF spectrum of the fragment anions after photofragmentation. The first part of the data analysis procedure is to isolate the events with laser on and laser off from the recorded data. Secondly, to

get the background subtracted TOF mass spectra of the fragment anions $C(t)$, the background signals from cluster anion i.e. laser off $C_{loff}(t)$ data and laser background $C_{lbkg}(t)$ data need to be subtracted from the laser on $C_{lon}(t)$ data using the relation,

$$C(t) = C_{lon}(t) - C_{loff}(t) - C_{lbkg}(t) \tag{2.38}$$

The above relation sometimes underestimates or overestimates the background subtracted signals, since the laser background data is taken at a later time after the data acquisition is completed for a range of intensities. To address this, we introduce a multiplication factor f, into the background subtraction procedure. This factor is defined as: $f = \frac{\text{Integrated laser-on counts in selected range}}{\text{Integrated laser background counts in same range}}$. The selected range starts from the laser background signal and extend to before the fragment signal begins. The modified background subtraction relation can be expressed as:

$$C(t) = C_{lon}(t) - C_{loff}(t) - C_{lbkg}(t) \times f \tag{2.39}$$

$$f = \frac{C_{lon}(t) - C_{loff}(t) - C(t)}{C_{lbkg}(t)} \tag{2.40}$$

Fig. 2.11 represents the TOF spectrum after the photofragmentation in the TOF range 20 μs to 26 μs. The TOF spectrum contains the parent anion and fragment anions as well as the laser background. Here the log scale is used to show both the parent and anion fragments. The parent anion will have the highest kinetic energy and will arrive at the detector at a later time, around 24.5 μs in the spectrum. The fragment anions having the same speed as parent anion will have lower kinetic energy and will arrive at the detector at earlier times (left of parent anion) e.g. in the TOF range 21.8μs to 24.2μs. The laser background is higher at earlier times (20μs to 21.8μs range) and decreases at later times. Fig. 2.12 shows the TOF spectrum in the range

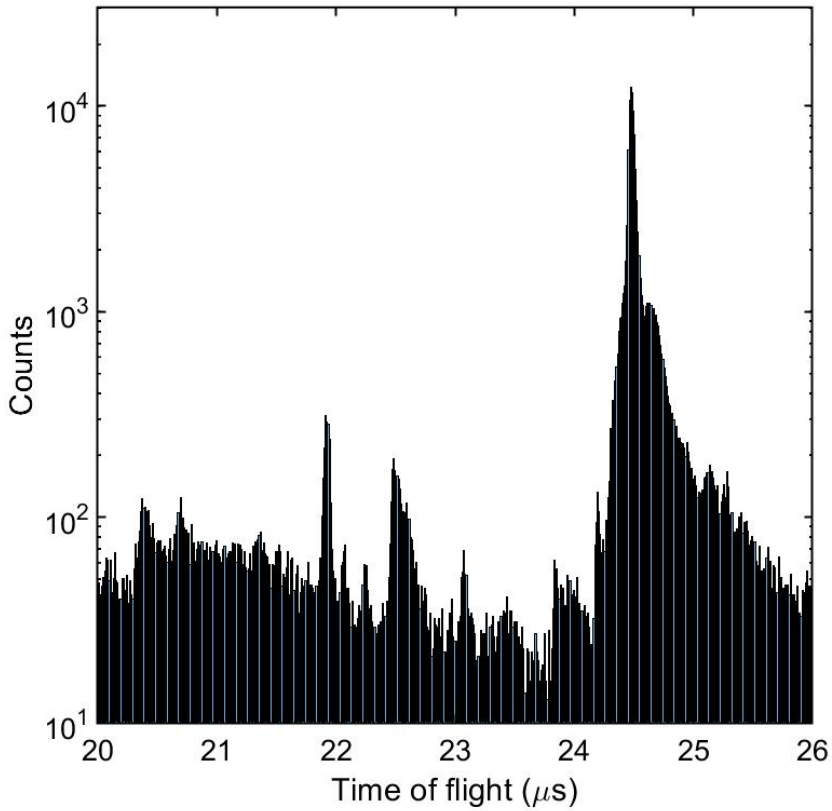

Figure 2.11: TOF Spectrum of the cluster anion $CF_3I \cdot I^-$ and fragment anions in log scale. Data was taken for 1000 s and at a laser energy of 830 μJ per pulse.

20μs to 24μs for laser on, laser off, and laser background. Using the relation 2.39, the background subtracted signal is obtained and is shown in Fig. 2.14. Since only fragment signals are shown in this figure, a linear scale is used.

To identify the possible anion fragments, we have used the SIMION simulation to match the experimental TOF data. For the SIMION simulations, we used the following parameters: (i) distance between the interaction region and reflectron entrance was set to 65 mm, (ii) length of the reflectron was 64 mm, and (iii) distance between the reflectron entrance and detector was 12 mm. The source size was modeled using a 3D Gaussian distribution with dimensions of 0.2 mm $\times$ 0.2 mm $\times$ 3 mm. These dimensions were chosen based on the considerations: (i) in the plane perpendicular

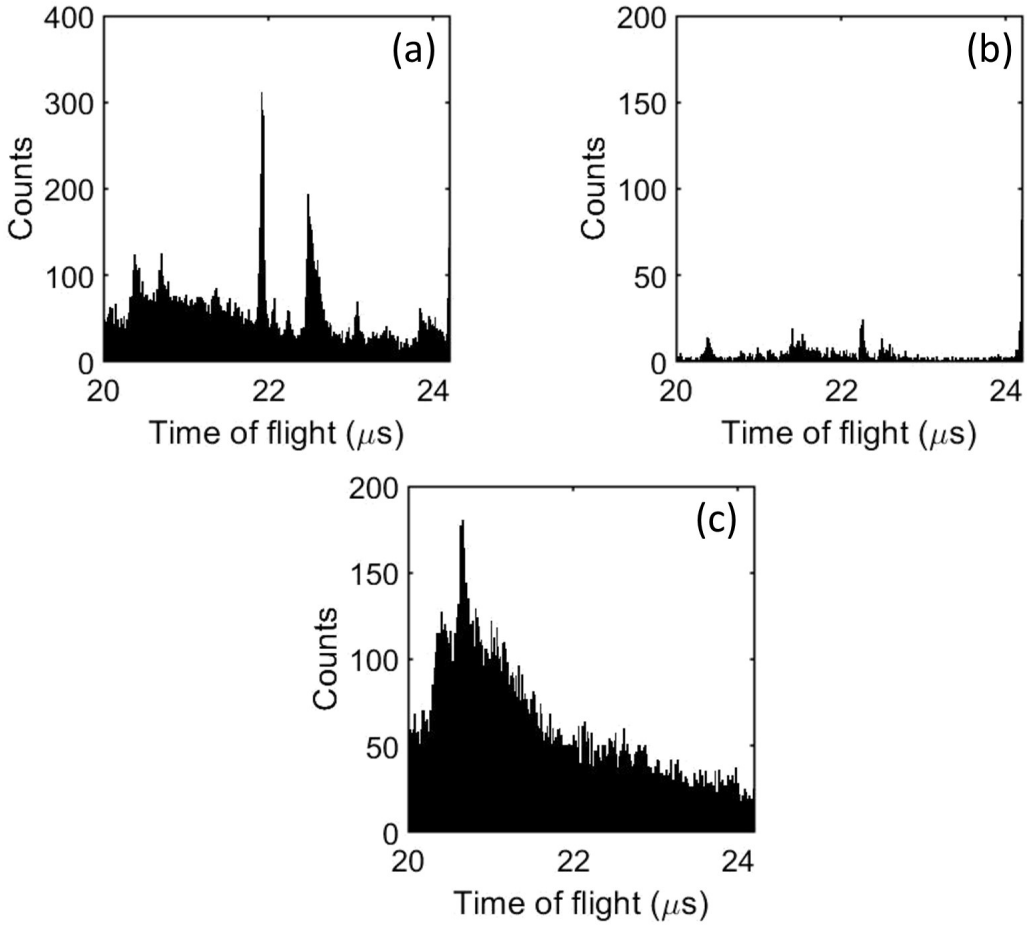

Figure 2.12: TOF spectrum in the range where fragment anions are expected. (a) laser on, (b) laser off, and (c) laser background data.

to the laser beam propagation, the source size is considered by the laser beam dimensitions (0.2 mm $\times$ 0.2 mm) and (ii) along the laser propagation direction, we used a 3 mm source size to account for the measured parent anion beam dimensions of 2.78 mm $\times$ 3.18 mm [85].

The velocity of both parent and fragment anions used in the SIMION simulation was determined to be 40.5 mm/μs. The CEM detector was placed at the interaction

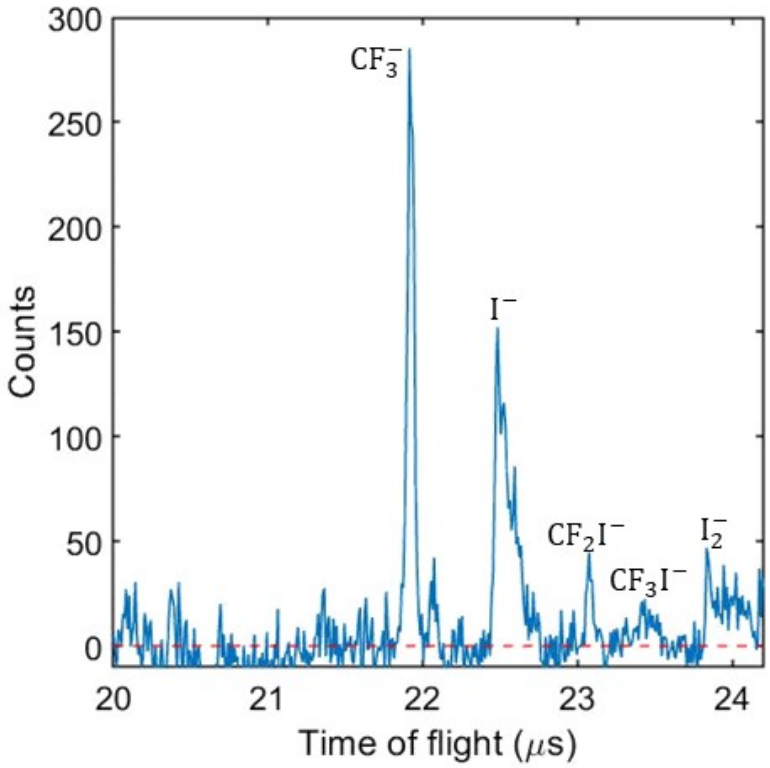

Figure 2.13: Background subtracted TOF spectrum of the fragment anions.

point to measure the time of arrival of the parent anions $CF_3I \cdot I^-$, which was 18.73μs as shown in Fig. 2.3. This time was measured by placing the CEM array at the interaction region. The arrival time of the parent anion was also measured at the circular CEM (Fig. 2.4) with the mass gate and reflectron off. Using the known distance between the interaction region and the circular CEM, along with the measured time of travel, the speed of the parent anion is calculated to be 40.5 mm/μs. As the anion fragments will have the same speed and size as the parent anion at the interaction region, the trajectories of the possible anion fragments from the interaction region to CEM array with reflectron on can be simulated using SIMION.

For SIMION, the voltages applied to the electrodes of the reflectron from V_1 to V_5 were -596.7 V, -1355 V, -2275 V, -3356.8 V, and -4600 V, respectively. These voltages

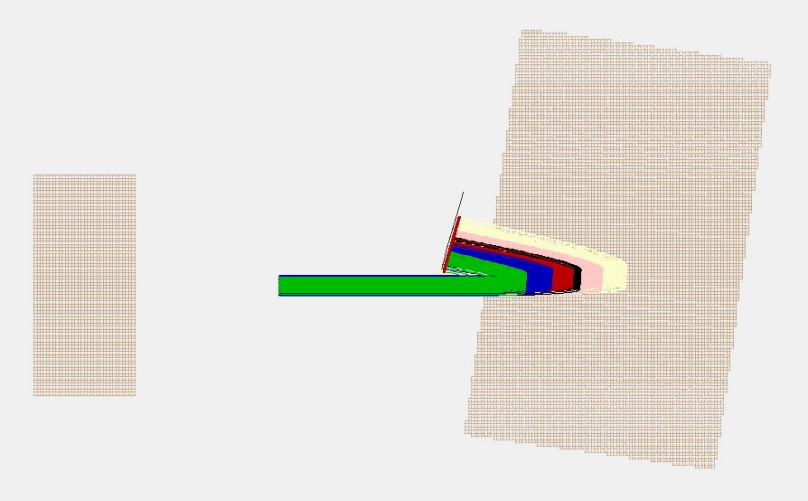

Figure 2.14: The trajectories of the parent and fragment anions in the SIMION simulation are shown. The the colors light yellow, pink, black , red, blue and green represent $CF_3I \cdot I^-$, $I_2{}^-$, CF_3I^-, CF_2I^-, I^- and $CF_3{}^-$, respectively.

are calculated using the procedure discussed in section 2.5. The maximum voltage of -4600 V was chosen on the last electrode V_5 during the experiment to maximize the parent anion counts. The possible anion fragments detected by comparing the extracted TOF from simulation and experimental TOF are $CF_3{}^-$, I^-, CF_2I^-, CF_3I^- and $I_2{}^-$. The trajectories of the parent anion and fragment anions in the SIMION simulation are shown in Fig. As given in Table 2.3, the extracted TOFs from SIMION simulation for these five fragment anions are consistent with the experimental TOFs with small deviations (less than 6%).

To summarize, Table 2.4 presents the potentials applied to various components of the apparatus, including the TOF mass spectrometer, Einzel lens, two pairs of parallel-plate deflectors, mass gate, and reflectron mass spectrometer, used in the multiphoton absorption experiment on $CF_3I \cdot I^-$.

Table 2.3: TOF (μs) data of the parent and fragment anions at the CEM array from the interaction point in the experiment and SIMION simulation.

Fragments	TOF (expt)	TOF (sim.)
CF_3^-	3.18	3.08
I^-	3.75	3.84
CF_2I^-	4.35	4.43
CF_3I^-	4.71	4.65
I_2^-	5.11	5.24
$CF_3I \cdot I^-$	5.55	5.88

Table 2.4: Potentials applied to various electrodes used in the experiment on cluster anion $CF_3I \cdot I^-$.

Electrodes	Potentials (V)
Repelling (TOF)	-3000 (pulsed, 2.258 μs)
Extraction (TOF)	-2535 (pulsed, 2.258 μs)
Ground (TOF)	ground
Side (Einzel lens)	ground
Middle (Einzel lens)	-1515 (constant)
Deflector 1	-52.9 (constant)
Deflector 2	+217 (constant)
Side (mass gate)	ground
Middle (mass gate)	-3000 (pulsed, 1 μs)
Reflectron 1st	ground
Reflectron 2nd	-596.7 (constant)
Reflectron 3rt	-1355 (constant)
Reflectron 4th	-2275 (constant)
Reflectron 5th	-3356.7 (constant)
Reflectron 6th	-4600 (constant)

Chapter 3

Multiphoton Fragmentation of Ion-molecule Cluster $CF_3I \cdot I^-$

3.1 Abstract

In recent decades, ion-molecule clusters have been used to study electron capture processes, where the excess electron on the ion is transferred to the molecule, triggering a dissociation reaction. This area of study is interesting because it includes a variety of processes, such as (i) the photoexcitation of ion-molecule clusters, (ii) the subsequent electron transfer to neutral molecules which generates molecular anions, and (iii) the dissociation of ion-molecule clusters while in the charge-transfer excited state. Methods such as photoelectron spectroscopy, photofragment action spectroscopy, and translational spectroscopy using single photons have been employed to study the charge-transfer excited state. We will use multiphoton absorption to investigate excited states of anions that may be either accessible or inaccessible through spectroscopic methods.

We have examined the multiphoton absorption in $CF_3I \cdot I^-$ for the first time to explore the fragmentation pattern under the intense laser field. We focus 400 nm pulses and record anion mass spectra as a function of intensity in the range 1.66×10^{13} to 2.8×10^{13} W/cm^2. We observed five different fragment anions: $CF_3{}^-$, I^-, CF_2I^-, CF_3I^- and $I_2{}^-$, along with total yields of neutral. The present multiphoton

fragmentation results are compared with the single photon study with $CF_3I \cdot I^-$ and with the low energy electron attachment to CF_3I through dissociative electron attachment (DEA). Among the fragments, in the single-photon absorption of $CF_3I \cdot I^-$, the fragments I^-, CF_3I^- and $I_2{}^-$ were observed, where as $CF_3{}^-$ and I^- were yielded in the DEA study of CF_3I. The threshold for each reaction and the number of photons absorbed in the fragmentation are also reported which suggests that more than one photon are absorbed for dissociation to occur in each channel. The different energies of the electrons produced in the charge transfer process are absorbed by CF_3I for each channel. This absorption accesses different resonance positions in CF_3I, which will dissociate into various fragments, though the fragments from the photodissociation process are not completely isolated. This observation is supported by the resonance positions observed in DEA studies to CF_3I for fragments $CF_3{}^-$ and I^-. Therefore, by using multiphoton absorption as a tool to study cluster anions, we demonstrate that different excited states can be accessed by absorbing varying number of photons. These distinct excited states will lead to the formation of different decay channels. Some of the excited states, and ultimately the fragments, cannot be produced using single-photon absorption in cluster anions.

3.2 Introduction

Electron transfer is an important topic responsible for many processes in atmospheric, plasma and radiation chemistry. Dissociative electron attachment (DEA) shares similarities with electron-transfer triggered dissociation. In DEA, low energy electrons of appropriate energy attach to a neutral molecule, forming a temporary negative ion [1]. This temporary negative ion then dissociates into a negative ion and a neutral fragment. In contrast, in the electron-transfer triggered dissociation of ion-

molecule clusters, the electron results from an electron transfer from the ion within the ion-molecule cluster. The fragmentation pattern may therefore differ between these two processes due to the presence a neutral in the vicinity of the molecular anion.

Plasma etching is an important manufacturing process in the fabrication of microelectronic devices [104, 105], and $CF_3I \cdot I^-$ could be a significant species in plasma chemistry. CF_4 and CHF_3 are the most common process gasses for plasma etching [106], but due to their long atmospheric lifetimes, they are considered global warming gases [28]. CF_3I is considered an alternate because of its relatively low global warming potential [107] and has shown etching rates similar to the traditional mixtures [108]. Despite this, the composition of these plasma is less understood [109]. The dissociative electron attachment to CF_3I generates I^- in high yield [110, 18] which can then interact with the abundant CF_3I gas to form species such as $CF_3I \cdot I^-$. These species though potentially common in plasma mix, have not been extensively studied.

The photoexcitation of $CF_3I \cdot I^-$ has been studied recently using single photon absorption in the wavelength range from 225 nm (3.5 eV) to 355 nm (5.5 eV) [111, 40, 84]. Using photoelectron spectroscopy, Bansu *et al.* [40] measured two direct photodetachment thresholds of $CF_3I \cdot I^-$ at 4.0 and 4.9 eV. The energy gap between the two vertical detachment energies (VDE) is due to spin-orbit coupling of the neutral iodine. The stabilization energy of $CF_3I \cdot I^-$, which is defined as the difference between the vertical detachment energy of the cluster and electron affinity of iodine (3.059 eV), is around 0.9 eV. This energy is much higher than many other anion clusters involving iodine: 0.47 eV for $I^- \cdot CH_3CN$ [112], 0.46 for $I^- \cdot H_2O$ [112], 0.36 eV for $I^- \cdot CH_3I$ [112], 0.172 eV for $I^- \cdot CO_2$ [44], 0.115 eV for $I^- \cdot N_2O$ [44], and 0.1 eV for $I^- \cdot CO$ [113]. Bansu *et al.* also suggested that there is a strong covalent contribution in $CF_3I \cdot I^-$ in addition to the charge dipole interaction, and could be the reason for

this high stabilization energy. The authors reported two charge transfer excited states near the two vertical detachment energies in addition to the vibrational structure in their photoelectron spectra.

Scarton [111] performed charge transfer DEA in ion-molecule cluster, $CF_3I \cdot I^-$ by photo-initiating electron transfer. Here the author performed single photon photoexcitation and photodetachment experiment of $CF_3I \cdot I^-$ using 260 nm (4.77 eV) and 318 nm (3.90 eV) photons below each of the direct photodetachment thresholds and detected anion fragments I^-, CF_3I^- and $I_2{}^-$. Analyzing photofragmentation action spectra, the author suggested that the electron attachment mechanism is probably due to the excitation of a weakly-bound ion state of the complex.

In the recent paper from our group [84], the excited-state dissociation dynamics of $CF_3I \cdot I^-$ was studied with a 266 nm (4.66 eV) laser pulse and compared with the ground and excited states of electronic structure calculations where the fragments I^- and CF_3I^- were detected along with neutral fragments. This study suggested the existence of a charge transfer excited state of $CF_3I \cdot I^-$ that is not stable and dissociates into fragments CF_3I^- and I. After retaining some of energy released in the dissociation as internal energy, CF_3I^- further dissociates into CF_3 and I^-.

In the above-mentioned experiments, the photodissociation of $CF_3I \cdot I^-$ was studied using a single photon in the vicinity of the two vertical detachment energies at 4.0 and 4.9 eV. So far, no attempt has been made to investigate the fragmentation pattern of $CF_3I \cdot I^-$ after multiphoton absorption. In this work, we aim to investigate the role played by the iodide ion in charge transfer excitation of the iodide-molecule cluster $CF_3I \cdot I^-$ when absorbing two or more photons of energy of 3.1 eV. The mechanism for the formation of the anion fragments can be described as an intracluster charge transfer [49, 50, 84] where an electron is ejected from I^- through the formation of a dipole-bound excited state. Upon electron transfer from I^- to CF_3I, the iodide

atom is no longer bound to the cluster. This electron is subsequently captured by CF_3I, initiating a process analogous to dissociative electron attachment. This electron capture triggers the dissociation of the molecule. The decay channels of $CF_3I \cdot I^-$ resulting in fragmentation through this process can lead to:

$$\begin{aligned} CF_3I \cdot I^- + kh\nu \rightarrow [CF_3I^- \cdots I]^* &\rightarrow CF_3I^- + I && (3.1)\\ &\rightarrow CF_3{}^- + I + I && (3.2)\\ &\rightarrow CF_3 + I^- + I && (3.3)\\ &\rightarrow CF_2I^- + F + I && (3.4)\\ &\rightarrow CF_3 + I_2{}^-, && (3.5) \end{aligned}$$

where k is the number of photons absorbed and $h\nu$ is the energy of each photon. Alternatively, by absorbing the photons, I^- can break directly from the $CF_3I \cdot I^-$ that may result in decay channels:

$$CF_3I \cdot I^- + kh\nu \rightarrow CF_3I + I^- \quad (3.6)$$

Electron detachment can also occur from $CF_3I \cdot I^-$ via direct detachment or indirectly from an excited state of the cluster, or from hot photofragments [49, 50] that produce neutrals only :

$$\begin{aligned} CF_3I \cdot I^- + kh\nu &\rightarrow CF_3I \cdot I + e^- && (3.7)\\ &\rightarrow [CF_3I \cdot I^-]^{-*} \rightarrow [CF_3I \cdot I^-] + e^- && (3.8)\\ &\rightarrow CF_3I^- + I \rightarrow CF_3I + I + e^-. && (3.9) \end{aligned}$$

To determine the multiphoton ionization rate, we will utilize a simple approach

as outlined in [54]. Consider a case involving 2-photon ionization, where the laser has a frequency ω and an intensity I. If a first-order energy-conserving transition can occur, the rate at which one photon is absorbed can be expressed as:

$$w_1 = \sigma_1 I \tag{3.10}$$

where σ_1 is the one photon cross-section. Let us consider the energy-time uncertainty relation, $\Delta E.\Delta t = \hbar\omega.\tau \approx \hbar$. Here τ represents the lifetime of a laser-induced virtual state. For a second photon to be absorbed, the interaction must occur while the system remains in this virtual state. The rate absorbing the second photon will be identical to the first, because the fundamental single-photon absorption process remains unchanged. The overall rate for the second photon absorption will be

$$w_2 = \sigma_1 I \omega^{-1} \sigma_1 I = \sigma_1 I \tau \sigma_1 I = \sigma_2 I^2. \tag{3.11}$$

One can generalize the overall rate of n photon ionization as:

$$w_n \simeq (\sigma_1 I \tau)^{k-1} \sigma_1 I = (\sigma_1^k \tau^{k-1}) I^k = \sigma_n I^k. \tag{3.12}$$

The above result is referred to as I^k power law.

The I^k relation is useful in identifying the order of the multiphoton process. By taking the natural logarithm of both the ionization rate and laser intensity, we obtain:

$$\ln(w_k) = \ln(\sigma_k) + k \ln(I) \tag{3.13}$$

$$\frac{\partial \ln(w_k)}{\partial \ln(I)} = k \tag{3.14}$$

The later result implies that when we plot the rate of ionization (the dependent

quantity in the experiment) against the laser intensity (the independent variable) in a double-logarithm representation, the data points form a straight line. The slope of this line corresponds to the integer number of photons involved in the process. This method allows us to identify the number of photons absorbed in the dissociation of each fragment anion. If the number of photons absorbed for the fragmentation channels is different, it suggests that the distinct excited states of the parent anion $CF_3I \cdot I^-$ are accessed during the photofragmentation process. Additionally, it is also possible that a fragment anion can be produced by multiple fragmentation channels in which case the slope will not be a single number. Therefore, distinct excited states activates different fragmentation pathways depending on the intensity of the laser.

For this experiment, we use 3.1 eV photons, which is well below the two vertical detachment energies, to investigate the fragmentation pattern of $CF_3I \cdot I^-$. We will concentrate on identifying the fragments and determining the dissociation channel by which $CF_3I \cdot I^-$ undergoes fragmentation. We will also present the threshold energy and the number of photons required for each channel. Finally, we will compare the dissociation channels resulting from the electron energy absorbed by CF_3I during the charge transfer process with the electron energy required for the DEA to CF_3I to occur for the same channels.

3.3 Experimental

The laser parameters to acquire the experimental data are $\lambda = 400$ nm and intensities up to $I = 2.8 \times 10^{13}$ W/cm^2. We measured the laser-induced multiphoton dissociation of $CF_3I \cdot I^-$ at five different intensities. These measurements were performed using a $f = 295$ mm focusing lens which produced a $1/e^2$ diameter of 330 μm. As discussed in section 2.6, the laser runs at 100 Hz while the cluster anion,

$CF_3I \cdot I^-$ beam was at 200 Hz. Alternating $CF_3I \cdot I^-$ pulses are dissociated by the intense laser pulses. With the pulsed valve switched off, the laser background data is taken separately. We subtract the laser background and laser off signals from the laser on signal to get the background subtracted TOF spectra as discussed in section 2.7.

3.4 Results and Discussion

3.4.1 Photofragmentation mass spectra of $CF_3I \cdot I^-$

Table 3.1: TOF (μs) data of parent anion, fragment anions, and neutrals at the CEM array and circular CEM from the interaction point in the experiment and SIMION simulation.

Molecules	TOF (expt)	TOF (sim.)
$CF_3I \cdot I^-$	[5.33-6.07]	5.88
$CF_3{}^-$	[3.07-3.305]	3.08
I^-	[3.67-4.03]	3.84
CF_2I^-	[4.27-4.435]	4.43
CF_3I^-	[4.57-4.82]	4.65
$I_2{}^-$	[5.055-5.205]	5.24
Neutral	[4.22-4.37]	4.30

We compare the experimentally obtained TOF of each peak with the SIMION simulations (Section 2.7) to identify the anion fragments. Fig. 3.1 shows the TOF spectrum of the fragment anions and neutrals produced after photoexcitation. There are five distinct peaks, each varying in peak heights and width. We identified five fragment anions: $CF_3{}^-$, I^-, CF_2I^-, CF_3I^-, and $I_2{}^-$, and total yield of neutrals. For neutrals, the TOF is measured from the interaction point to the circular CEM while for the parent and fragment anions, the TOF is measured from the interaction point

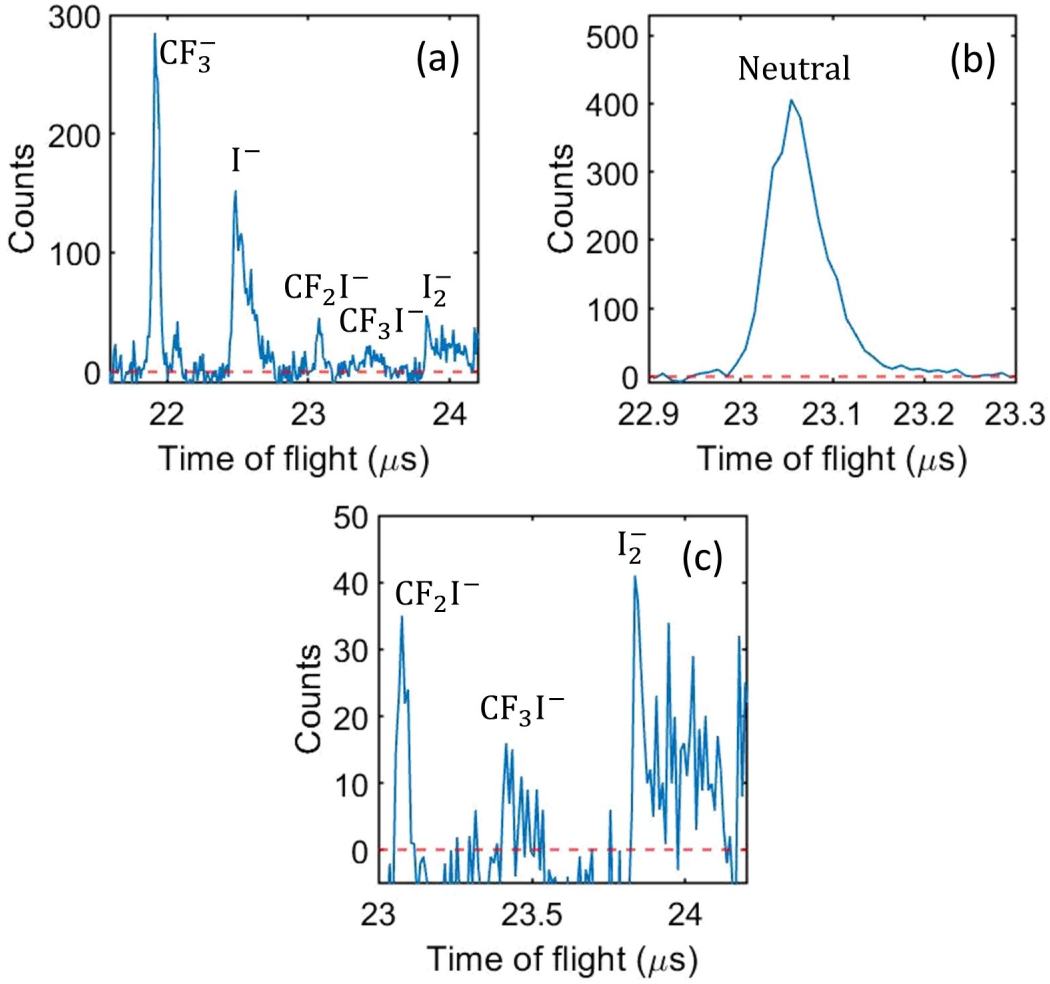

Figure 3.1: TOF spectrum of the (a) fragment anions, (b) neutrals and (c) zoomed version of fragments from multiphoton dissociation of $CF_3I \cdot I^-$ at 400 nm and intensity of 2.8×10^{13} W/cm^2.

to the CEM array. Since the peak widths of different anions vary, a specific width (around four times their FWHM) as shown in Table 3.1 is chosen for each peak to extract the total counts. Fragments anions travel through two meshes through the LPQ reflectron with a total transmission efficiency of 62% while the neutrals travel through three meshes with a total transmission of 49%. To match the transmission efficiency, neutral counts are multiplied by a factor of 1.265 in all calculations.

Figure 3.1c, shows the background-subtracted TOF spectra of the three least abundant fragment anion peaks and was obtained by choosing a bin size of 10 ns. It is important to note that the subtraction process (discussed in section 2.7) can lead to negative count in the TOF spectra. Since laser on, laser off, and laser background counts are distributed in a Poisson distribution, there is a statistical uncertainty of $\sqrt{C}$ for any counts C. In areas dominated by laser background, the subtraction may result in both positive and negative values due to the statistical fluctuations. These negative values are retained because removing them would artificially increase the counts.

Care should be taken when comparing the relative yields of different fragment anions and neutrals at the same laser intensity. The efficiency of Channel Electron Multipliers (CEMS) for detecting negative ions and neutrals increases with increasing energy: the detection efficiencies rise sharply at low energies and reach a plateau of near unity at higher energies [114, 115, 116]. On MCP-based detector, Stephen and Peko [114] measured the absolute detection efficiencies of neutral, positive, and negative oxygen. The authors found that the likelihood of detecting neutral oxygen increases by more than two orders of magnitude while the efficiency of negative oxygen detection varies less than one order of magnitude as the energy increased from 20 eV to 1000 eV. The fragment anions and neutrals produced after photofragmentation at the interaction region have the same velocity as the parent anion, but their energies differ due to their different masses. In our experiment, the parent anion has an energy of 2748 eV, while the lowest mass observed fragment anion CF_3^- has an energy of 587 eV, and the lowest mass neutral can be fluorine F with an energy of 162 eV. Neutrals with lower energy may not be detected at the same efficiency as those with high energy or as efficiently as fragment anions. We have not performed an absolute calibration of the detector efficiency in our experiment. However, Koplitz and McVey

[117], in their study of the multiphoton ionization of bromobenzene, have pointed out that the relative intensities of a given fragment across a range of laser intensities might be more reliable. We will discuss next the fragmentation pattern at different intensities.

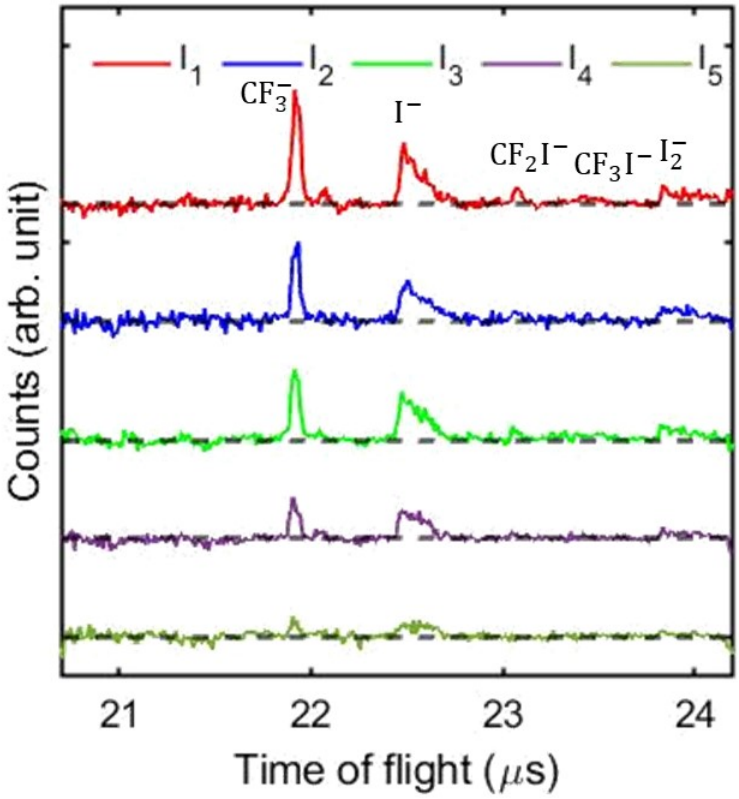

Figure 3.2: Photofragments generated by multiphoton excitation of $CF_3I \cdot I^-$ at intensities: I_1= 28 TW/cm^2 , I_2= 25.5 TW/cm^2 , I_3= 22.3 TW/cm^2 , I_4= 19.5 TW/cm^2, and I_5= 16.6 TW/cm^2.

3.4.2 Fragmentation pattern at different intensities

We present the TOF spectra of the fragment anions and neutrals as a function of pulse intensity in Figs. 3.2 and 3.3. In the experiment, the laser intensity was changed by changing the phase matching angle of the BBO crystal. The most dominant

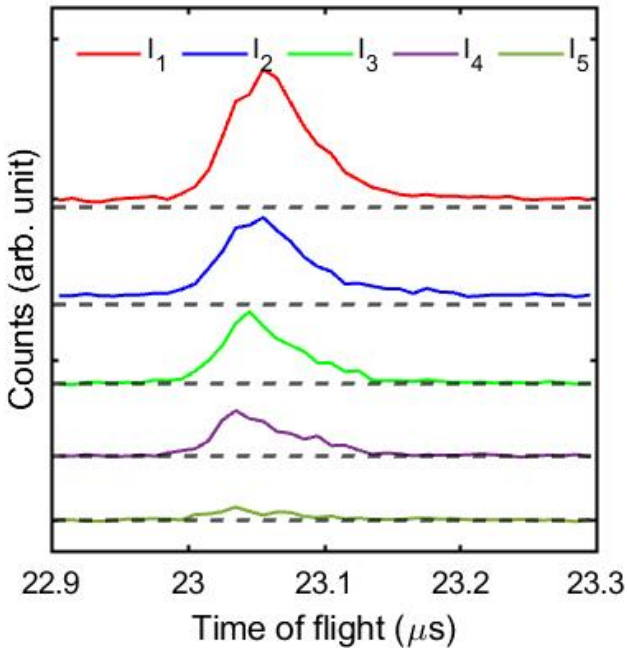

Figure 3.3: Neutrals generated by multiphoton excitation of $CF_3I \cdot I^-$ at intensities: I_1= 28 TW/cm^2 , I_2= 25.5 TW/cm^2 , I_3= 22.3 TW/cm^2 , I_4= 19.5 TW/cm^2, and I_5= 16.6 TW/cm^2.

fragments observed across all intensities are CF_3^- and I^-. In contrast, the signals for the other fragments CF_2I^- and I_2^- are relatively weak and are noticeable at all the intensities in the spectra. A small quantity of CF_3I^- is detected as a minor fragment; however, its yield is insufficient to follow its intensity dependence. In general, the signals for both fragment anions and neutrals decrease as the intensity decreases. Moreover, the yield of each fragment anion and neutrals not only varies with the laser intensity, but the ratio of any two fragment signals also changes with intensity. We will explore two intensity-dependent scenarios: (i) the ratio of the total anion counts with respect to the total neutrals yield and (ii) the ratio of each fragment's signal and the total yield of neutrals to the parent anion.

To determine the intensity-dependent branching ratios, the total anion signal at each intensity is normalized to the counts of the total neutral yield, as shown in Fig.

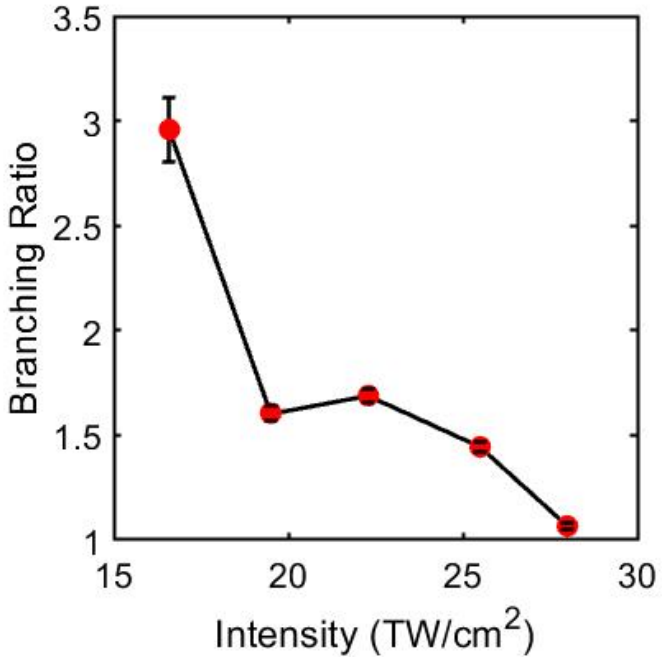

Figure 3.4: Branching ratios of the total fragment anions with respect to the total yield of neutrals versus the laser intensity.

3.4. The relative yield of the neutrals increases with intensity, indicating a higher probability of photodetachment at higher intensities. It is evident that the branching ratios of the fragment anions increase as the laser intensity decreases, peaking at the lowest intensity. This means that at lower intensities, anionic fragmentation becomes more dominant than the electron detachment from $CF_3I \cdot I^-$, resulting in a higher proportion of these specific fragment anions. As discussed in Section 3.2, the electron detachment channels predominantly produce high-mass neutrals, which are detected more efficiently by the CEM due to the higher detection efficiency for higher energy neutrals.

We will now focus on how the yield of the different fragments depends on intensity. To account for fluctuations in the anion beam current, we use the ratio of the fragment counts to the parent counts. In this analysis, we exclude the fragment anion CF_3I^-

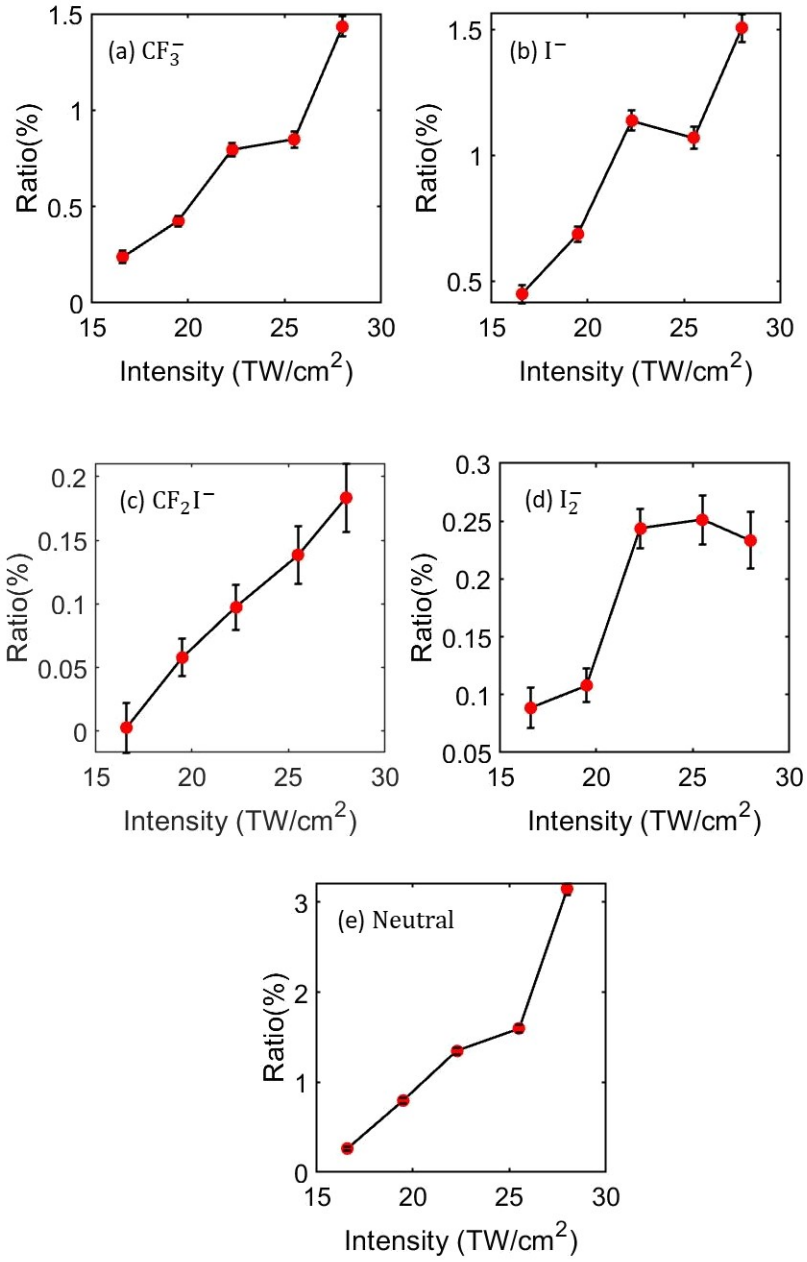

Figure 3.5: (a), (b), (c), (d), and (e) show the ratio of photofragments: CF_3^-, I^-, CF_2I^-, and I_2^-, and neutrals with respect to the parent anion at different laser intensities. Here the ratio is defined as the fragment signal divided by the parent anion $CF_3I \cdot I^-$ signal.

due to its low signal-to-noise ratio, and therefore no ratio analysis is attempted for this fragment. The ratios of CF_3^-, I^-, CF_2I^-, I_2^-, and neutrals to the parent anion

Table 3.2: The ratio of photofragments: CF_3^-, I^-, CF_2I^-, and I_2^-, and neutrals relative to the parent anion at different laser intensities. Here the ratio is defined as the fragment signal divided by the parent anion $CF_3I \cdot I^-$ signal. To estimate the uncertainty for each species, we follow these steps: (i) calculate the square root of the integrated counts within the interval provided in Table 3.1 for each condition: laser on, laser off and laser background, and (ii) combine the results using the rules of error propagation for summation, as detailed in [8]. For the ratios of the fragment signals to the parent anion signal, the uncertainties are propagated using the rules of error propagation for quotients[8].

I (TW/cm^2)	Neutral	CF_3^-	I^-	CF_2I^-	I_2^-
28	3.147 ± 0.065	1.434 ± 0.062	1.506 ± 0.055	0.183 ± 0.027	0.233 ± 0.025
25.5	1.598 ± 0.041	0.848 ± 0.042	1.070 ± 0.044	0.138 ± 0.022	0.251 ± 0.021
22.3	1.346 ± 0.037	0.795 ± 0.034	1.138 ± 0.039	0.097 ± 0.018	0.244 ± 0.017
19.5	0.796 ± 0.029	0.425 ± 0.027	0.687 ± 0.032	0.058 ± 0.015	0.108 ± 0.014
16.6	0.263 ± 0.020	0.239 ± 0.032	0.449 ± 0.035	0.003 ± 0.019	0.088 ± 0.017

are given in Table 3.2 and also shown in Fig. 3.5 as a function of intensity. In Fig. 3.5, each data point presents the integrated signal of the corresponding fragment anion or neutral divided by the integrated signal of the parent anion at each intensity. The integration ranges used for these calculations are given in Table 3.1. As one would expect, the highest uncertainties are found in anions for which the signal-to-noise ratio is very low, such as CF_2I^- and I_2^-. Overall, as the intensity decreases, the ratio of the fragment anions and neutrals decreases except for I_2^-. The I_2^- signal shows a plateau for intensities above 22 TW/cm^2 and then falls off sharply below that. This behavior will be discussed in more detail in the following section.

Fig. 3.6 shows that the ratio of the anion fragments and neutrals relative to the parent plotted against laser intensity in double logarithm representation. Weighted least square fits have been performed on the data, and the corresponding mathematically fitted slopes are given in Table 3.3. The curves for the fragment anions CF_3^-, I^-, and CF_2I^- indicate 3.07 ± 0.52 , 1.99 ± 0.49, and 3.26 ± 0.69 photon processes,

respectively. For I_2^- anion, there are two regions of intensity where the slope is different. Initially, a slope of four indicates that four photons are needed in the production of I_2^-. However, as the intensity increases, the slope decreases to zero, suggesting a saturation point where increasing the intensity no longer affects the anion yield. At this point, other mechanisms such as dissociating into neutral and ionic iodide or just electron detachment from I_2^-, may occur. The highest uncertainty, observed for the I_2^- fragment (4.09 ± 1.36), suggests some mixing between processes involving three to five photons. In general, as a fragment could be produced by multiple channels, some mixing is expected. The fitted slopes for the neutrals also indicate a process involving the absorption of four photons. It would explain the higher yields of neutrals at higher intensities relative to the anions.

Table 3.3: Fitted slopes were determined by plotting the natural log of the fragment anion signals with the natural log of the laser intensity and fitting to linear trends weighted by the error bars.

Species	Mathematically fitted slopes
CF_3^-	3.07 ± 0.52
I^-	1.99 ± 0.49
CF_2I^-	3.26 ± 0.69
I_2^{-*}	4.09 ± 1.36
Neutral	3.9 ± 0.64

* The highest two intensities are excluded for this slope calculation (See Fig. 3.6d). The fitted slope for the highest three intensities is -0.1 ± 0.27.

3.4.3 Thermodynamic threshold and excess energy

We will use Hess's law to calculate the threshold for the reaction as well as the excess energy. The thermodynamic threshold is equivalent to the sum of three energy

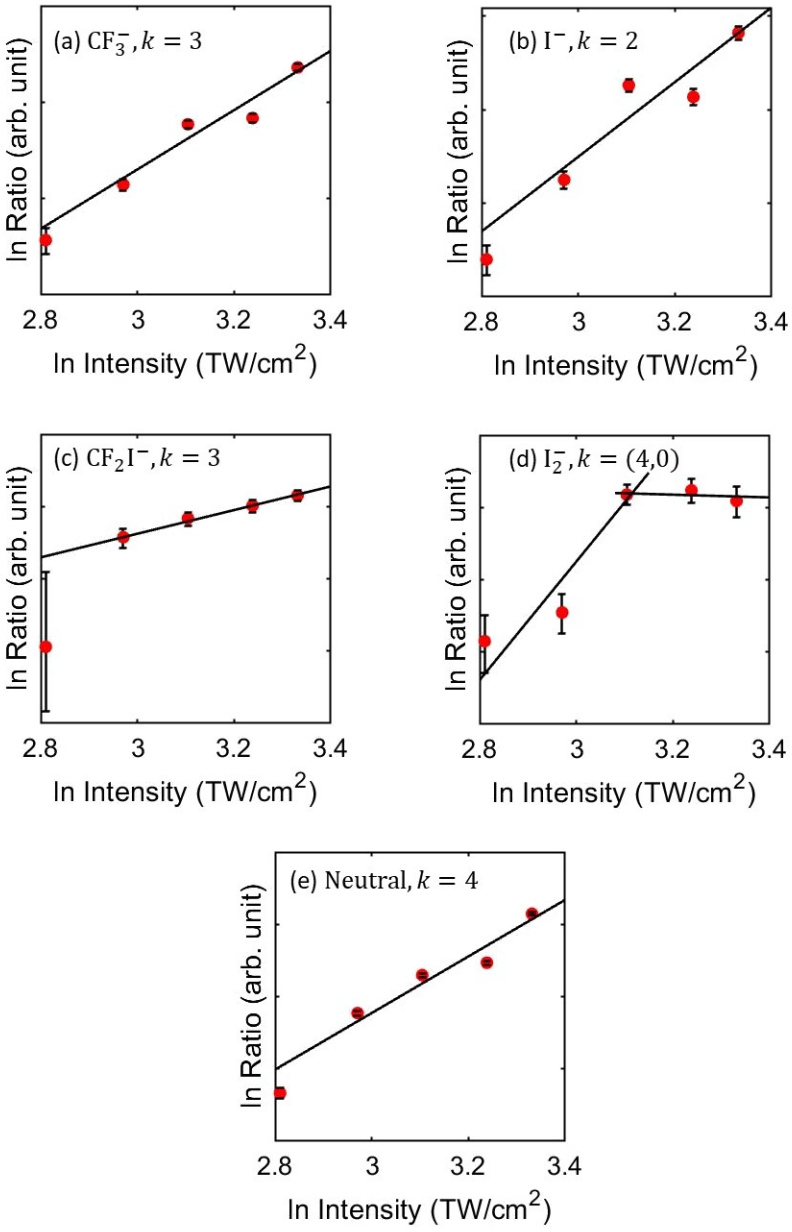

Figure 3.6: Dependence of the natural log of the fragment anion signals with the natural log of the laser intensity for (a) CF_3^-, (b) I^-, (c) CF_2I^-, (d) I_2^-, and (e) neutrals. Weighted least-squares fits have been performed on the data, and the k values represents the resulting slopes suggesting the number of photons absorbed in that photofragmentation channel. Mathematically fitted slopes can be found in Table 3.3.

components: (1) the energy required to remove the electron from the ion-molecule complex, i.e, electron affinity of $CF_3I \cdot I^-$; (ii) the energy necessary to break the relevant bond in the process (e.g, C–I bond in CF_3–I); and (iii) the energy released upon reattaching the electron to the receptor i.e. electron affinity of the receptor. The excess energy is the photon energy minus the thermodynamic threshold. This excess energy will be partitioned in the translational and vibrational energy of the recoiling fragments. There are two electron detachment thresholds of $CF_3I \cdot I^-$ at 4.0 and 4.9 eV due to the spin-orbit coupling of the neutral iodide. As an example, we will show the calculations of the thermodynamic threshold and excess energy for $CF_3{}^-$ as follows. Assuming the photon energy initiates a charge transfer followed by dissociation:

$$\begin{aligned} \mathrm{TH} &= \mathrm{EA}(CF_3I \cdot I^-) + \mathrm{D}(CF_3\text{–I}) - \mathrm{EA}(CF_3{}^-) \\ &= 4 + 2.39 - 1.7 = 4.69\,\mathrm{eV} \end{aligned}$$

where TH represents the thermodynamic threshold of the reaction, EA denotes the electron affinity, and D represents the bond dissociation energy. The experimental data showed that the production of $CF_3{}^-$ proceeds via a three photon process. Therefore,

$$\begin{aligned} \mathrm{Excess\,energy} &= \mathrm{h}\nu\text{-TH} \\ &= 9.3 - 4.69 = 4.61\,\mathrm{eV} \end{aligned}$$

The thermodynamic thresholds and excess energies of the fragments anions are given in Table 3.4. Here we assumed the electron from I^- is transferred to CF_3I and left the neutral iodide in $^2P_{3/2}$ or $^2P_{1/2}$ state. For the calculations, the value of the

Table 3.4: The thermodynamic threshold (TH) and excess energy of the fragment anions. k is the number of photons absorbed and $h\nu = 3.1$ eV is the photon energy.

Fragments	k	khν	TH ($I[^2P_{3/2},^2P_{1/2}]$)	E_{excess} ($I[^2P_{3/2},^2P_{1/2}]$)
CF_3^-	3	9.1	4.69, 5.59	4.61, 3.71
I^-	2	6.2	3.33, 4.23	2.87, 1.97
CF_2I^-	3	9.3	x	x
CF_3I^-	x	x	2.43, 3.33	x
I_2^-	4	12.4	3.87, 4.77	8.53, 7.63

bond dissociation energy D(CF_3–I)= 2.39 eV [118] is used. The electron affinities of CF_3 and I used are = 3.059 eV [119] and = 1.7 eV [120]. For the electron affinity of $CF_3I \cdot I^-$, the first and second peaks at 4 and 4.9 eV in the photoelectron spectra [40] are used here.

Upon charge transfer from I^- to CF_3I, CF_3I^- will dissociate through the dissociative electron attachment, producing CF_3^-, I^- and CF_2I^-. The fragment I^- can also be produced via directly detaching from $CF_3I \cdot I^-$. For the this process, the binding energy between CF_3I and I^- in $CF_3I \cdot I^-$ has been calculated to be 0.742 eV [84]. Some CF_3I^- produced in charge transfer process are stable enough to survive until it reaches to the detector. We will discuss the formation of I_2^- in the following section. It is observed that the threshold energies for each channel are above the one photon energy of 3.1 eV used in the experiment, except for CF_3I^- with neutral I in $^2P_{3/2}$ state. Therefore, more than one photons are required for fragmentation to happen.

3.4.4 Comparison with single photon excitation and DEA

We will compare the photofragments identified in our multiphoton absorption experiment with those observed in single photon studies of $CF_3I \cdot I^-$, as well as with the fragments of the dissociative electron attachment to CF_3I. Of particular rele-

vance to our study are the works of Scarton [111] and Wang *et al.* [84]. Scarton used photon energies of 3.9 eV and 4.77 eV. In their experiment, the photon energies were obtained by frequency mixing the output of a Nd:YAG-pumped Spectra-Physics MOPO-710 (optical parametric oscillator). The laser intensities were maintained sufficiently low to ensure that only single-photon processes were possible. The author observed photofragments I^-, CF_3I^- and $I_2{}^-$ which matches with the present multiphoton absorption results, although they didn't observe the other two fragment anions: $CF_3{}^-$ and CF_2I^-. On the other hand, only I^- and CF_3I^- were detected with 4.66 eV photons by Wang *et al.* [84].

Studies on low energy electron attachment to CF_3I through dissociative electron attachment [18, 17] have reported the formation of F^-,$CF_3{}^-$, I^-, and FI^-, but no detectable CF_3I^-. Among these fragments, $CF_3{}^-$ and I^- matches with our measurement. These two fragments were produced at two resonance positions at electron energies around 3.8 eV and 0 eV, respectively.

In DEA to CF_3I, the maximum yield of $CF_3{}^-$ anions appeared at approximately 4 eV incident electron energy. In our experiment, we found that the $CF_3{}^-$ channel is accessed through the absorption of three UV photons at 400 nm. The 9.3 eV excitation of $CF_3I \cdot I^-$ can produce electrons with energies of 5.3 eV or 4.4 eV, corresponding to the $^2P_{3/2}$ and $^2P_{1/2}$ states of neutral iodine, respectively. These electrons can subsequently be captured by CF_3I. It is highly probable that the 4.4 eV electron is captured by CF_3I forming TNI CF_3I^-, which dissociates to $CF_3{}^-$ and I. This suggests that our experiment accesses the same resonance as in the DEA studies.

The fragment I^- can be produced via two mechanisms: (i) an electron transfer from I^- to CF_3I, resulting in dissociation to yield $CF_3 + I + I^-$ and (ii) Direct detachment of I^- from $CF_3I \cdot I^-$, producing $CF_3I + I^-$. In the DEA study, the maximum

yield of I^- is peaked around 0 eV incident electron energy [17, 18]. We observed that the I^- channel is a 2 photon process. Therefore, 6.2 eV excitation to $CF_3I \cdot I^-$ can produce 2 eV or 1 eV electrons in two spin-orbit states of iodide. It is likely that 1 eV electrons from the iodide in $^2P_{1/2}$ state are captured by CF_3I which dissociate to produce I^- and CF_3.

The binding energy between CF_3I and I^- in $CF_3I \cdot I^-$ has been calculated to be 0.742 eV [84]. Therefore, only one photon with energy 3.10 eV should be sufficient to break the $I \cdot \cdot I^-$ bond in $CF_3I \cdot I^-$. In our experiment, it is not possible to distinguish from which the I^- is produced based on the TOF spectra. However, we observed that the width of the I^- signal is the largest among all fragments. This broadening suggests that the I^- anions may be generated through multiple pathways, contributing to their varied kinetic energies (not measured) and resulting in a broader distribution in the TOF spectra.

The production of CF_2I^- is a three-photon process. In the literature unfortunately the electron affinity of CF_2I is not available so we cannot calculate the threshold energy. This anion was not observed in single photon excitation and DEA studies. However, its observation in multiphoton studies suggests that the absorption of three photons accesses an excited state inaccessible via single-photon or DEA processes.

The threshold for CF_3I^- production in charge transfer process is 2.43 eV (Table 3.4) and 3.33 eV ($^2P_{3/2}$ and $^2P_{1/2}$), respectively suggesting one or two photon process. But, CF_3I^- has greater chance of dissociating due to its large DEA cross-section for I^- around 0 eV electron energy [17, 18]. This channel is not observed in DEA study but observed in single-photon studies.

The I_2^- can be produced after electron transfer from I^- to CF_3I, followed by direct breaking the $C \cdot \cdot I$ bond. The threshold for the I_2^- production is 3.87 eV (Table 3.4). In our experiment, I_2^- production is a 4 ± 1 photon process at lower

laser intensities and reaches saturation at higher intensities. Previous studies have reported six vertical detachment energies from I_2^-, ranging from 3.235 eV to 4.418 eV, corresponding to the ground and five valence excited states of neutral I_2 [121, 122]. Additionally, three resonance positions were observed at 0.05 eV, 0.9 eV, and 2.5 eV from DEA to I_2 [123]. At these higher intensities, I_2^- can either dissociate to neutral and ionic iodide or just directly detach the electron.

These observations highlight that different fragmentation channels are activated by varying numbers of photons, reflecting the complex dynamics of multiphoton ionization where different photon absorption processes involve accessing of multiple excited states of the parent anion $CF_3I \cdot I^-$

3.5 Conclusion

The intensity dependence of the multiphoton fragmentation of $CF_3I \cdot I^-$ has been studied using 3.1 eV photons. Five different fragment anions: CF_3^-, I^-, CF_2I^-, CF_3I^- and I_2^- were observed, along with total yields of neutral. Threshold energy calculations suggested that at least two photons needed to be absorbed for dissociation to occur leading to the formation of these anion fragments. This finding is consistent with the number of photons absorbed as determined by the fitted slopes. The production of neutrals indicated a four-photon process, which explains the higher yields of neutrals at higher intensities.

In contrast to the single-photon studies, where only the fragments anions I^-, CF_3I^- and I_2^- were observed, the multiphoton study detected two additional fragments: CF_3^- and CF_2I^-. In addition, observation of CF_3^- and I^- in the current experiment is consistent with the DEA study. These two anions were formed at two different TNI states. The absorption of 3 and 2 photons for these channels in the experiment

suggested that electrons produced at different energies in charge transfer process are absorbed by CF_3I, accessing two TNI positions that will dissociate to $CF_3{}^-$ and I^-.

In conclusion, electrons of different energies, produced in the charge transfer process are absorbed by CF_3I, leading to formation of distinct TNI states. These states subsequently dissociate into different fragments. Noticeably, discrepancies in fragmentation channels between multiphoton and single-photon studies suggest that certain excited states accessible through multiphoton processes may be inaccessible via single-photon absorption. Furthermore, the detection of CF_2I^- fragment, absent in both single-photon and DEA studies, provides evidence for the production of a unique TNI state exclusively observable in multiphoton experiments. These observations indicate the unique capability of multiphoton studies in probing the electronic structure of molecular anions.

3.6 Outlook

In this chapter, we discussed the dissociation of $CF_3I \cdot I^-$ where multiple photons with an energy of 3.1 eV were absorbed. We have provided evidence that multiple excited states were accessed through multiphoton absorption, leading to dissociation into different fragment channels. In order to further validate this observation of multiple excited states, an identical experiment should be performed on analogous molecules such as $CF_3Br \cdot I^-$. This would further provide additional information into the charge transfer and direct dissociation mechanisms through the observation of I^- and Br^- fragments anions.

Electron imaging techniques, such as velocity map imaging (VMI), can be used to investigate the dissociation dynamics. A VMI setup can be integrated into the existing apparatus to enable time-dependent studies. In the time-resolved photodissociation

process, a second laser pulse is used to probe the excited anions and measure the temporal evolution of kinetic energy and angular distributions of the resulting photoelectrons. Time-resolved investigations utilize photoelectron angular distribution (PAD) measurements to reveal dissociation mechanisms and electronic relaxation dynamics, providing complementary information to the temporal evolution of electron kinetic energy spectra. Additionally, if the pump pulse induces rotational coherences within an electronic state, the temporal progression of these coherences can be systematically monitored through the acquisition of time-resolved PAD data.

Chapter 4

Dissociative Electron Attachment to Acetic Acid

4.1 Introduction

Simple carboxylic acids are well established to exhibit rich chemical reactivity in environments that are exposed to low energy free electrons [124]. Dissociative electron attachment (DEA) is an important reaction that occurs by resonant electron-molecule interactions, producing a transient negative ion (TNI) resonance [125]. There are many prominent examples of molecules having several anion resonances, characterized as single-electron shape resonances, or excited resonances, where a target electron is excited in the electron attachment process, producing a correlated two-electron one-hole system that decays by autodetachment or dissociation [36]. Feshbach resonances occur when the potential energy of the anion resonance is lower than the corresponding excited state of the neutral molecule. This energetically forbids the resonance from decaying by single-electron autodetachment, thus enabling nuclear motion and dissociation to proceed on femtosecond timescales.

Acetic acid produces several reactive anions and neutral radicals by DEA, which proceeds via a shape resonance at low attachment energies, or via Feshbach resonances at higher energies [126, 127, 128, 129, 130]. Sailer *et al.* [126] reported nine fragment anions in the 0-13 eV electron energy range with the dominant products

being $CH_2O_2^-$ and CH_3COO^-, appearing from two low energy resonances at 0.75 eV and 1.5 eV, respectively. The authors also performed *ab initio* calculations and assigned these states as single particle shape resonances to the two lowest unoccupied molecular orbitals, LUMO and LUMO+1. Subsequent works in Refs. [127, 128] confirmed the existence of a 1.5 eV shape resonance in the dissociation channel producing CH_3COO^-. Freitas *et al.* [131] performed electronic structure calculations using the Schwinger multichannel method and found that the π^* shape resonance at 1.5 eV is characterized by single occupation of the LUMO, having A'' symmetry, with dissociation enabled by nonadiabatic coupling to an A$'$ state. The authors found no explanation for the lower energy production of $CH_2O_2^-$ that was reported in the experiments of Sailer *et al.* [126, 127]. Recently, Chakraborty *et al.* [129] reported a velocity slice imaging study of the heavier anion fragments around the 10 eV Feshbach resonance, tentatively assigning the $13a'$ Rydberg state as the parent TNI state by comparing the resonance energy with the $13a'' \rightarrow 3pa''$ Rydberg transition that was reported at 9.268 eV in VUV absorption spectroscopic studies by Leach *et al.* [6].

Prabhudesai *et al.* [19, 11] carried out DEA measurements leading to H^- ions from acetic acid, and H^- and D^- from partially deuterated acetic acid, CH_3COOD, in the energy range of 0-18 eV identifying three resonance peaks. For CH_3COOD, the authors found that the first two sharp resonances at 6.7 eV and 7.7 eV contributed to the O-D bond break, and the third broad resonance, centered at 9.1 eV, produced H^- by C-H bond break. The relative yields of H^- and D^- from two different bond scissions confirmed the existence of a functional group dependence leading to site-selective fragmentation at the hydrogen site, which was also observed in condensed phase acetic acid [132]. Despite of H^- being the dominant anion fragment around 6-10 eV from DEA to acetic acid [19, 11], the resonance symmetries, dissociation mechanisms, and dynamics of the TNI resonances in acetic acid remain poorly un-

derstood.

Dissociation of acetic acid by O-H break produces H^- and an acetyloxyl radical, CH_3COO, which has several low-lying excited electronic states [5, 133] that could be significantly populated at ambient temperatures. This radical is therefore an important intermediate in atmospheric, combustion, and synthetic organic chemistry [134, 135]. Dissociation by C-H break results in a carboxymethyl radical, CH_2COOH, which may play an important role in the formation of glycine and other complex organic molecules in planetary atmospheres and interstellar media [136].

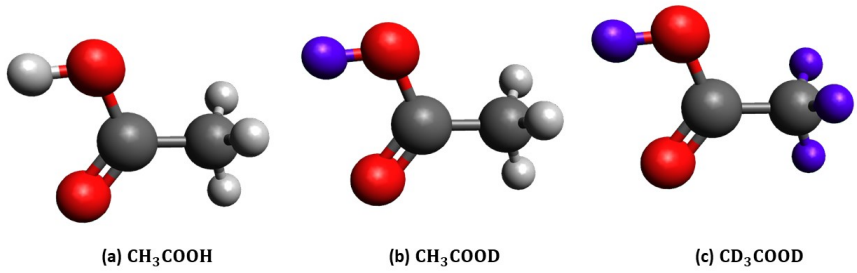

Figure 4.1: Molecular structure of (a) acetic acid, (b) partially deuterated acetic acid, and (c) fully deuterated acetic acid.

In this work we focus on the rich information provided by the momentum distributions of either H^- or D^- anions, produced by breaking specific bonds, namely the hydroxyl (O-H or O-D) and/or methyl (C-H or C-D) bonds. For this, we have carried out anion fragment momentum imaging measurements on acetic acid (CH_3COOD) partially deuterated acetic acid, CH_3COOD, and fully deuterated acetic acid (CD_3COOD), their structural schematics shown in Fig. 4.1. We examine the kinetic energy and angular distributions of the H^- and D^- fragments measured by 3D anion fragment momentum imaging in the 6.7 eV to 10 eV energy range. Anion fragment angular distributions contain information about the symmetry of the resonance states as well

as the associated dissociation dynamics of the specific dissociation channel of interest.

We continue with a brief description of the experimental technique in Sec. **??**. In Sec. 4.3, we describe a model that we employ to analyze the experimental angular distributions to understand the possible resonance symmetries. In Sec. 4.4, we summarize our experimental results for the O-H and C-H bond breakage that are provided by momentum images as well as the associated kinetic energy and angular distributions. In Sec. 4.5 and 4.6, we discuss the results and provide concluding remarks.

4.2 Experimental Setup

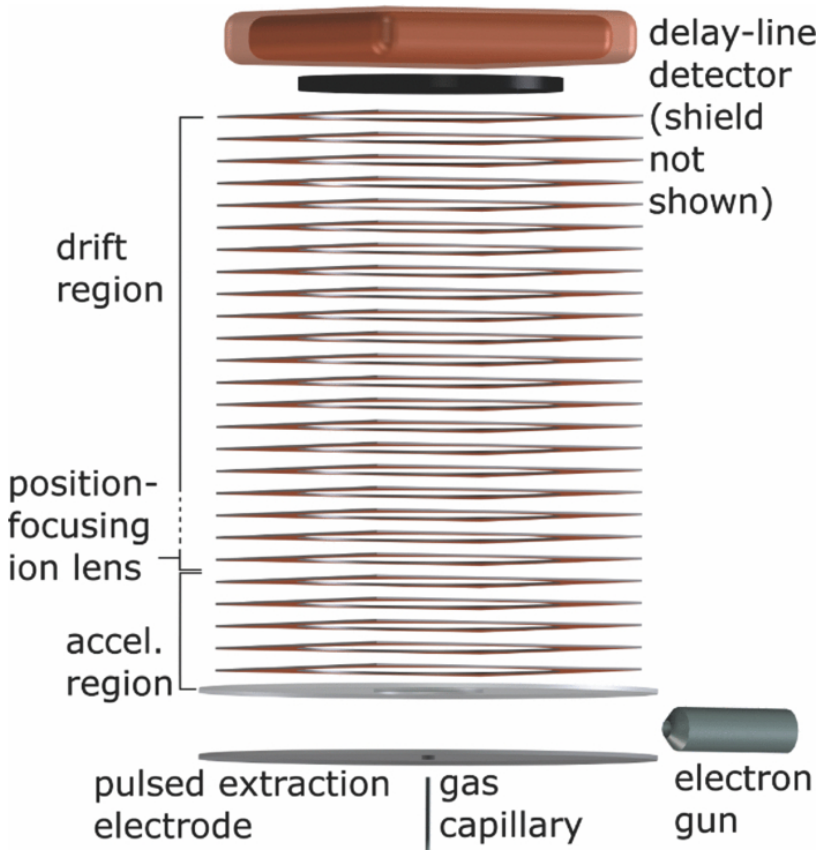

Figure 4.2: A schematic diagram illustrating the geometry and main components of the momentum imaging apparatus. Figure adopted from Ref. [2].

The experimental apparatus used in the present study has been described in detail previously in Ref. [2] and the schematic diagram is shown in Fig. 4.2. Here we provide a brief discussion of the experimental arrangement most relevant to the current work. Briefly, the setup consists of an energy-tunable pulsed electron beam from a commercially acquired electron gun (Kimball Physics Inc.) and an effusive gas jet of the molecular target from a stainless steel capillary that was directed perpendicular to the electron beam. The gun produces 80 ns pulses of electrons at 50 kHz repetition rate, with an energy spread of 0.5 eV full-width-at-half-maximum (FWHM) in a beam 1 mm in diameter. A pair of Helmholtz coils, producing a 25 G uniform magnetic field coaxial to the electron beam, collimates and transports the electrons to the interaction region while preventing most of any scattered electrons from entering the anion imaging spectrometer. The anion yields of O^- from DEA to CO_2 across the thermodynamic threshold at 3.99 eV were measured for the calibration of the electron beam mean energy, which was checked before and after each experiment.

The 3D anion fragment momentum imaging spectrometer consists of a series of copper electrodes that constitutes an ion acceleration region and an ion focusing drift region, with the time-of-flight direction being orientated perpendicular to the electron beam and parallel to the effusive gas jet direction. An ion repeller electrode is grounded while the electron beam packet passes through the interaction region. It is then subsequently pulsed to -35 V, in order to push any anions formed in the electron-molecule attachment process into the spectrometer, after the short electron bunch (80 ns) cleared the interaction region. In the present experiments, the electric field was typically 24 V/cm over the entire acceleration region. In the ion focus region of the spectrometer, which forms an electro-optical lens to compensate for the extended electron-molecule interaction volume, the electric field was varied from 120 V/cm to 0 V/cm. The anions are momentum-imaged onto a pair of time sensitive

80 mm diameter multichannel plates (MCP) chevron stack, equipped with a position-sensitive delay-line anode. The arrival times and positions of the ions were recorded event-by-event in list-mode format. After a thorough off-line calibration and analysis, the 3D momenta of each ion fragment were generated. A momentum calibration was performed by measuring the well-known O^- kinetic energy and angular distributions from DEA to O_2 [137].

The H^- channel can be formed by hydroxyl (O-H) or methyl (C-H) bond break. The dissociation channels were isolated by performing experiments with acetic acid deuterated only at the hydroxyl site (CH_3COOD). The anion imaging spectrometer allows us to identify H^- and D^- by their times-of-flight, and thus the contributions of each dissociation channel at different energies were separated. The thermodynamic thresholds for the relevant two-body and three-body reactions are given in Tab. 4.1.

Table 4.1: Energetics of various dissociation channels producing H^- fragments. The enthalpy of formation, bond energies, and electron affinities were taken from Refs. [9, 10, 11, 12, 13, 14]

Number	Dissociation channel	Thermodynamic threshold (eV)
1	$H^- + CH_3COO$	4.02
2	$H^- + CH_2COOH$	3.47
3	$H^- + CH_3 + CO_2$	3.39
4	$H^- + CH_2CO + OH$	5.46
5	$H^- + CH_2 + COOH$	7.99

4.3 Angular Distributions

In the axial recoil approximation (ARA) [138], the dissociation axis of a molecule does not rotate significantly during the dissociation process, i.e., the dissociation of the TNI state occurs much faster than the rotation of the bond, proceeding ei-

ther by molecular rotation or other nuclear degrees of freedom. Consequently, the angular dependence of electron attachment in the molecular frame is preserved in the dissociation as long as the ARA is valid. A result of the ARA is the angular distribution fragment ions, with respect to the incoming electron beam direction, depends only on the electron attachment probability in the body-fixed frame of the molecule [139, 140]. Within the ARA, the fragment angular distributions can reveal the electronic symmetry or nuclear conformation of the initial state [141, 142]. In some previous studies, electron scattering theory has been employed to predict fragment angular distributions under the ARA and, when compared with anion fragment imaging measurements, the ARA was found to break down, indicating coupled electronic and nuclear dissociation dynamics [143] and conical intersections [144] coupling electronic states of the anion.

O'Malley and Taylor [139] pioneered early theory efforts to connect the fragment angular distribution to the symmetry of the resonance states of the transient anions produced in DEA. This theory applies specifically to diatomic molecules and assumes that (i) only single resonance states contribute in the DEA process and, (ii) that the subsequent dissociation obeys the ARA, i.e., that the negative ion state does not undergo a rotation during the dissociation, and (iii) that the coupling is independent of the spin states, i.e., only depends on pure electronic matrix elements. Using the above approximations, Azria *et al.* [145] later expanded this theory to polyatomic molecules and obtained the following expression for the distribution of the anionic fragments as a function of the angle θ relative to the incident electron beam:

$$I^{\epsilon}(\theta) \propto \frac{1}{2\pi} \int_0^{2\pi} |\sum_{lm} a_{lm} i^l e^{i\delta_l} \chi^{\epsilon}_{lm}(\theta, \phi)|^2 d\phi \tag{4.1}$$

where (θ, ϕ) are the polar and azimuthal angles between the electron beam and the

dissociation axis of the anion. $\chi^{\epsilon}_{lm}(\theta, \phi)$ are the basis functions of the irreducible representation of the point group of the molecule and are expressed in terms of a linear combination of spherical harmonics in the molecular dissociation frame. The expansion coefficients a_{lm} are real numbers. The phases δ_l represent the contributions of the direct scattering process to the DEA resonance [146]. The values of the indices l and m with a non-zero contribution to the sum in Eq. (4.1) are restricted to the irreducible representation of the resonant state. Only a few values of partial waves, for instance up to $l = 2$, where $l = 0, 1$ and 2 represent s, p and d partial waves, respectively, are needed to fit the angular distributions. As the number of partial waves increases, so does the number of maxima and minima in the angular distributions [145].

The application of this model to fit the experimentally measured angular distributions has been demonstrated for several diatomic [146] and polyatomic molecules [145, 147, 148, 149, 150, 151]. The applicability of this approach is limited to single resonance cases only, and the coupling of two resonances may not be treated properly. A more rigorous method would be to perform *ab initio* electron scattering calculations [143]. However, this method is computationally expensive, even for small molecules, and requires an extensive survey of the electron-molecule autodetachment continuum to identify the most relevant states, which is beyond the scope of the present experimental study.

Acetic acid, in the equilibirum geometry of the ground electronic state, is planar with the symmetry point group C_s. The C_s point group has two symmetry operations: identity, E, and reflection through the mirror plane, σ_h. The two symmetries in the two irreducible representations associated with the Cs point group are A' and A''. The

A' representation is symmetric to both E and σ_h. The A'' representation is symmetric to E but antisymmetric to σ_h. The ground state configuration of acetic acid, according to the density functional theory molecular orbital calculations of Leach *et al.* [6], is $(1a' - 10a')^2(1a'')^2(11a')^2(12a')^2(2a'')^2(3a'')^2(13a')^2$, which has A' symmetry. The angular distribution function under the ARA for $A' \rightarrow A'$ transitions with the three lowest partial waves s, p and d, is

$$\begin{aligned} I^{A'}(\theta) =& \alpha_{00}^2 + 2\alpha_{00}\alpha_{10}\sin(\delta_0 - \delta_1) \\ &+ \alpha_{10}^2\cos^2(\theta) + \alpha_{11}^2\sin^2(\theta) + \alpha_{20}^2(3\cos^2(\theta - 1)^2 \\ &+ \alpha_{21}^2\cos^2(\theta)\sin^2(\theta) + \alpha_{22}^2\sin^4(\theta) \\ &+ 2\alpha_{00}\alpha_{20}\cos(\delta_0 - \delta_2)(3\cos^2(\theta - 1)^2 \\ &+ 2\alpha_{10}\alpha_{20}\sin(\delta_1 - \delta_2)\cos\theta(3\cos^2(\theta - 1)^2 \\ &+ 2\alpha_{11}\alpha_{21}\sin(\delta_1 - \delta_2)\cos\theta\sin^2(\theta) \end{aligned} \tag{4.2}$$

and the $A' \rightarrow A''$ transitions, with the two lowest partial waves p and d is

$$\begin{aligned} I^{A''}(\theta) =& \alpha_{11}^2\sin^2(\theta) + \alpha_{21}^2\sin^2(\theta)\cos^2(\theta) + \alpha_{22}^2\sin^4(\theta) \\ &+ 2\alpha_{11}\alpha_{21}\sin(\delta_1 - \delta_2)\cos\theta\sin^2(\theta) \end{aligned} \tag{4.3}$$

Each of the present measured angular distributions are fitted with the Equations (4.2) and (4.3) to find the resonance symmetry.

4.4 Results

The experimental results are organized as follows. We present the momentum imaging experimental results obtained from the dissociation products of the O-H/O-D and C-H/C-D bond breakages of acetic acid and its partially- and fully-deuterated isotopologues, over the energy range 6.7 eV to 10 eV. We then present the ion kinetic energy distributions, which we extract directly from the measured absolute momenta. Finally, we present the angular distributions and, following the procedure discussed in section 4.3, we fit our angular distributions for the candidate $A' \rightarrow A'$ and $A' \rightarrow A''$ transitions to determine the symmetry of the TNI state.

4.4.1 H^- (D^-) due to O-H (O-D) bond break

The measured momentum images of the D^- anions resulting from DEA to partially deuterated acetic acid, CH_3COOD, at the first resonance (6.7 eV) are displayed in Fig. 4.3a. For each momentum image, the entire 3D momentum distribution of H^-/D^- ions is projected onto the longitudinal and transverse momentum coordinates with respect to the incident electron beam direction. The longitudinal and transverse coordinates are parallel and perpendicular to the incident electron beam, respectively. We observe that the momentum distributions have comparable intensity in the forward (positive longitudinal) and perpendicular directions, while exhibiting maximum intensities in the backward (negative longitudinal) direction. The transformation of the 3D momentum distributions to longitudinal and transverse coordinates[2] projects uncertainties at very small transverse momenta, which we see as noise along zero transverse momentum.

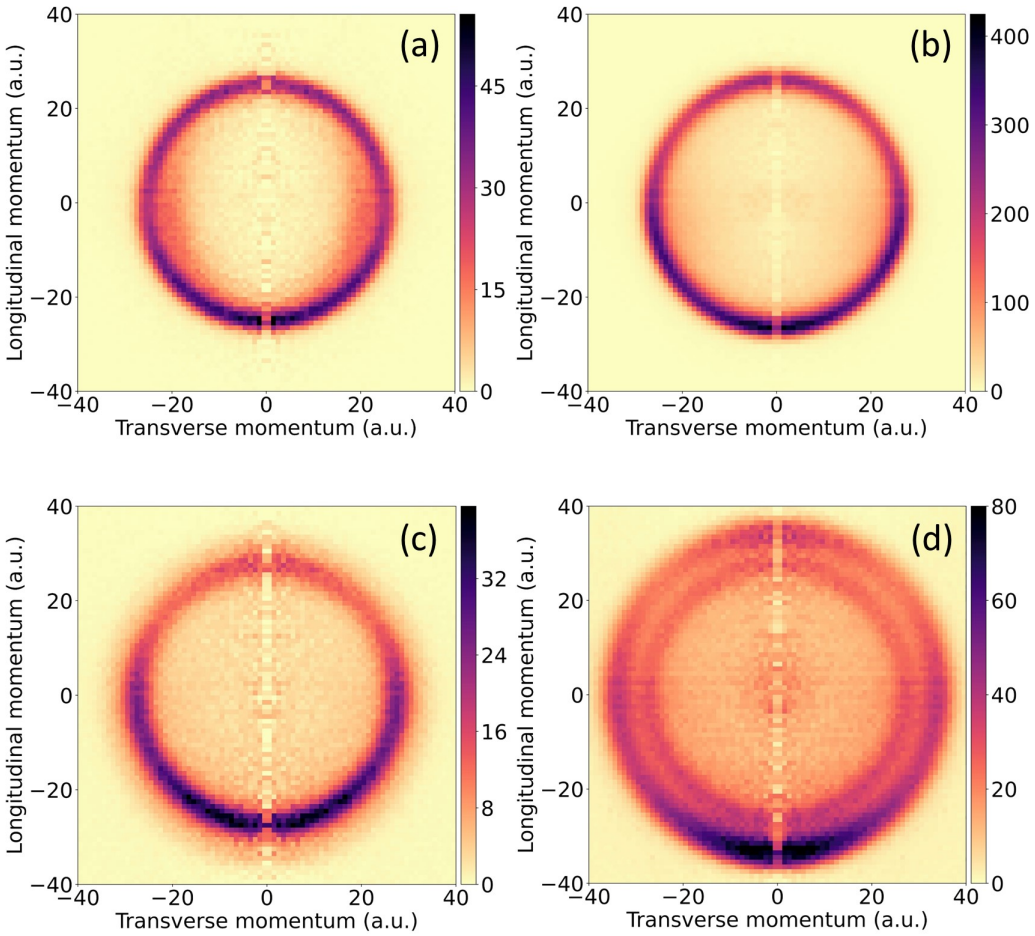

Figure 4.3: Momentum distribution of D^- ions from O-D bond cleavage of CH_3COOD at incident electron energies of (a) 6.7, (b) 7.7, (c) 9.1 eV and (d)10 eV. The incident electron momentum is in the positive longitudinal direction (upward).

The momentum distribution of D^- from CH_3COOD (Fig. 4.3b) at the second resonance (7.7 eV) shows a similar maximum in the backward direction just like the first resonance at 6.7 eV. In contrast to the momentum image at 6.7 eV, the 7.7 eV momentum image has broader peaks in the backward and perpendicular directions. As the electron energy is increased to 9.1 eV in Fig. 4.3c, we observe a similar structure again, with a maximum ion yield in the backward and perpendicular directions

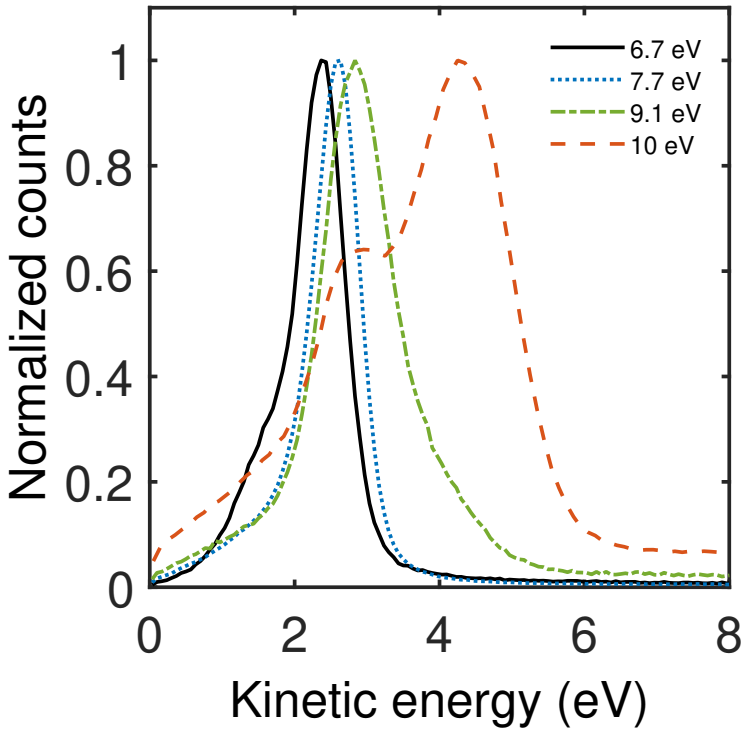

Figure 4.4: Kinetic energy distribution of D^- ions from O-D bond cleavage of CH_3COOD at incident electron energies of 6.7, 7.7, 9.1 and 10 eV. The ion yield for each distribution is rescaled to a maximum of 1 (arbitrary units).

and with very little ion yield in the forward direction. Fig. 4.3 shows the momentum distribution of the D^- ions from CH_3COOD at 10 eV, where two distinct rings, corresponding to two different ion momenta, i.e., fast and slow ions, are observed, indicating two different dissociation pathways. The outer ring (fast D^-) and inner ring (slow D^-) have momenta of $\approx$ 27 a.u. and $\approx$ 35 a.u., respectively. The ion emission patterns of the fast and slow ions have similar features: a global maximum in the backward direction, and significant yields in the perpendicular and forward directions. We note that the ion yield of the slow D^- appears to be smaller than the yield for the fast D^- at 10 eV, however the relative yields depend strongly on the incident energy, and are almost equal at 9.6 eV.

The kinetic energy distributions of the D^- ions, obtained from DEA to CH_3COOD, are shown in Fig. 4.4. The kinetic energy distribution of D^- at 6.7 eV (solid black curve) has two features: a peak at 2.39 eV, and a low-energy shoulder around 1.6 eV. Previous studies [152, 153, 154] showed that the cross-sections for producing H^- and D^- from DEA to H_2O and D_2O, respectively, is very high at 4.6 $\times 10^{-}18$ cm^2 around 6.7 eV. Therefore, any D^- fragments from DEA to D_2O contaminants are expected to be strongest around this energy. The kinetic energy for the 1.6 eV feature is consistent with a small ($< 2\%$) contamination of the CH_3COOD sample with D_2O [154]. We also performed H^- DEA momentum imaging measurements at the 6.7 eV and 7.7 eV resonances in CH_3COOH and D^- from CD_3COOD, neither of which are presented here, because the water contamination in each sample was evidently higher, such that the $H^-(D^-)$ contribution from DEA to background H_2O (D_2O) was more significant. Any contributions from H_2O and D_2O at energies higher than 7 eV were determined, by the same comparisons, to be insignificant.

The 2-body dissociation producing D^- anions by O-D bond cleavage can be written in the form of Reaction 1 in Tab. 4.1. Based on the thermochemical data [9, 10, 11], the threshold for this dissociation channel is 4.02 eV. The difference between the incident energy and the threshold for the reaction to take place is the excess energy, which is 2.68 eV for an incident electron energy of 6.7 eV. This energy is distributed between the translational kinetic energies and the internal energies of the fragments. Using momentum conservation, we can estimate the total kinetic energy release, E_T:

$$E_T = E_T^i \times \frac{M}{m} \tag{4.4}$$

where, E_T^i, M, and m are the kinetic energy of the D^- fragment, the mass of the parent molecule, CH_3COOD, and the mass of the neutral fragment, CH_3COO, respectively.

At 6.7 eV of the incident electron beam, the peak in the kinetic energy distribution appears to be at 2.39 eV. The difference between the excess energy and E_T is 0.25 eV. This is 9% of the available excess energy, and it contributes to rotational and/or internal excitation of the CH_3COO fragment. At 7.7 eV, the kinetic energy of the D^- anion has a peak at 2.6 eV, corresponding to $E_T = 2.69$ eV. The excess energy is 3.68 eV, leaving about 27% of the available excess energy as rotational or internal energy in the neutral molecular fragment. As the incident electron energy is increased to 9.1 eV at the 3rd resonance in Fig. 4.4 for D^-/CH_3COOD, about 2.1 eV (corresponding to 41% of the excess energy) goes into the internal energy of the neutral fragment. At 10 eV, the peak corresponding to the slow D^- is similar in energy and width to the peak at 9.1 eV. In contrast, the fast D^- kinetic energy peak is at 4.5 eV, and the width of the fast D^- distribution is about 2 eV. About 1.52 eV and 2.9 eV (i.e., $\approx$ 25% and 48% of the excess energy) is partitioned into rotational or internal excitation of the fast and slow neutral fragments, respectively. Remarkably, for all of the incident energies in the present experiments, more than 50% of the dissociation energy is partitioned into the translational energy of the dissociating fragments.

Fig. 4.5a shows the angular distribution of the D^- ions from O-D bond breakage for the fist resonance at 6.7 eV from DEA to CH_3COOD. Here, we include only the ions with kinetic energies above 1.8 eV, in order to exclude any possible contributions from the small background of D_2O. The dissociation angle is defined with respect to the incident electron beam direction. Most of the fragment ion yield is in the backward direction $> 120°$, with smaller ion yields in the range of $0 - 120°$. The measured angular distributions are fitted with equations (4.2) and (4.3), for three models: (i) $s + p(A')$ (blue), (ii) $s + p + d(A')$ (black), and (iii) $p + d(A'')$ (purple). The angular distributions clearly show a finite ion yield in the 0° and 180° directions (i.e., parallel and antiparallel to the electron beam, corresponding to right and left in

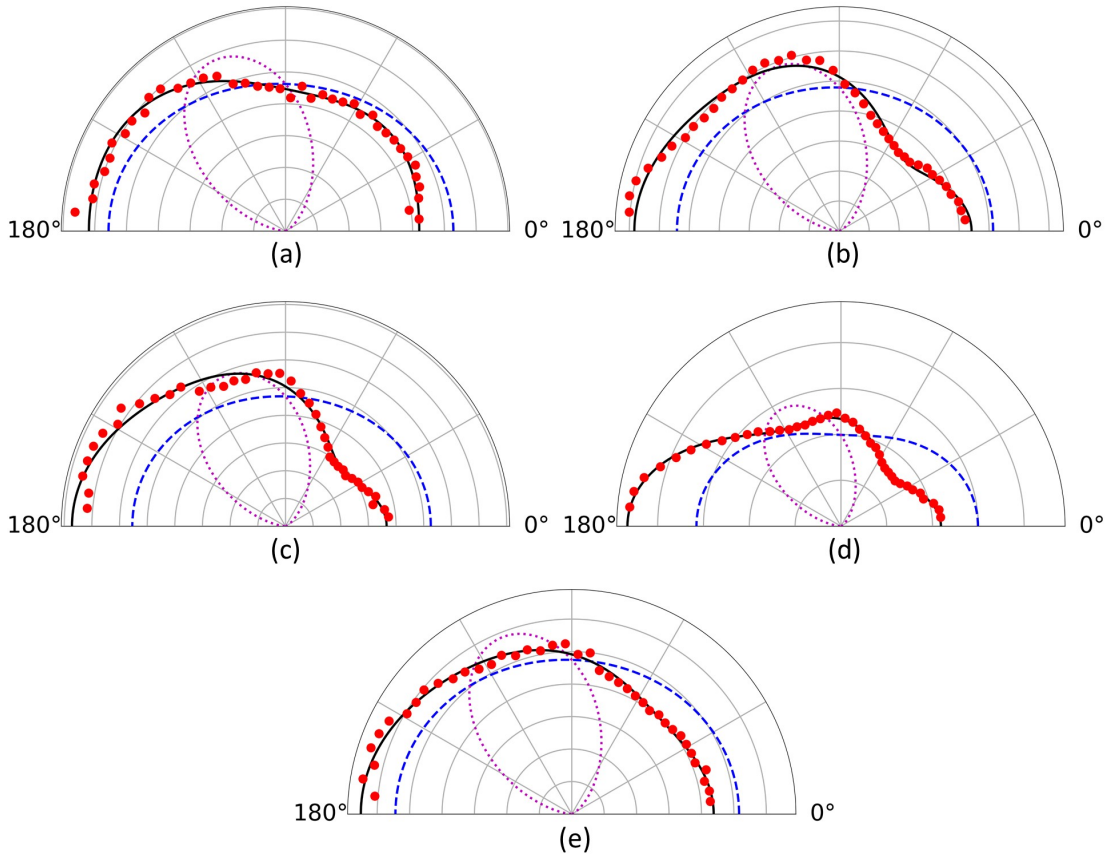

Figure 4.5: Angular distributions of D^- ions from O-D bond cleavage of CH_3COOD, at (a) 6.7, (b) 7.7, (c) 9.1, (d) 10 eV (fast ions), and (e) 10 eV (slow ions). The experimental angular distributions (solid red circles) are fitted assuming $A' \rightarrow A'$ transitions using partial waves s+p (dotted blue lines) and s+p+d (solid black line), and under the assumptions of $A' \rightarrow A''$ transitions using partial waves p+d (dotted purple lines). The incident electron direction is 0 deg.

Fig. 4.5a), requiring an s-wave contribution. Consistently, the fit with partial waves $p + d$ corresponding to an $A' \rightarrow A''$ transition model shows the poorest agreement with the experimental data. The fit with only the two lowest partial waves $s + p$ ($A' \rightarrow A'$) fails to reproduce the forward-backward asymmetry in the measured angular distributions. The addition of a d-wave to $s + p$, in the $s + p + d(A')$ model, reproduces the profile of the of the angular distribution much better at all angles with an $R^2 \approx 0.96$. This clearly indicates that at 6.7 eV, the populated TNI state has A'

symmetry, if we assume that the ARA holds.

The measured angular distributions of the D^- ions at 7.7 and 9.1 eV from DEA to CH_3COOD, corresponding to the second and third resonances, respectively, are shown in Figs. 4.5b-4.5c. The two resonances have qualitatively similar angular distributions of the D^- ions, which peak around 100° and 170° with a shallow minimum around 50° and a small local maximum around 0°. These features contrast with the lower energy resonance (Fig. 4.5a), which is generally more isotropic. Both, the 7.7 eV and 9.1 eV angular distributions are consistent with $s+p+d$ ($A' \rightarrow A'$) transition models (black curves in Figs 4.5b-4.5c), which produce satisfactory fits with $R^2 \approx 0.99$. In contrast, the $p + d(A'')$ and $s + p(A')$ transition models fit the experimental data poorly, failing to produce the measured maxima or relative forward and backward ion yields. Therefore, it is most plausible that both the 7.7 and 9.1 eV resonances have A' symmetry under axial recoil approximation.

For 10 eV electron attachment, we examine the fast and slow ions in Figs. 4.5d and 4.5e, respectively. In both cases, the preferred general direction of ion ejection is again in the backward direction, opposite to the incident electron beam. Again, only the model including the lowest three partial waves $s + p + d$ ($A' \rightarrow A'$) provides a satisfactory fit, $R^2 > 0.97$, strongly suggesting that the 10 eV resonance also has A' symmetry.

4.4.2 $H^-(D^-)$ due to C-H (C-D) bond break

The momentum images of the H^- and D^- anions for the C-H/C-D bond break from the third resonance at 9.1 eV for DEA to CH_3COOH, CH_3COOD, and CD_3COOD are shown in Figs. 4.6a-c. Besides the faster H^-/D^- ions (outer rings in Figs. 4.6a-c), slower ions are also observed the the center of the image in each case. The ion yields

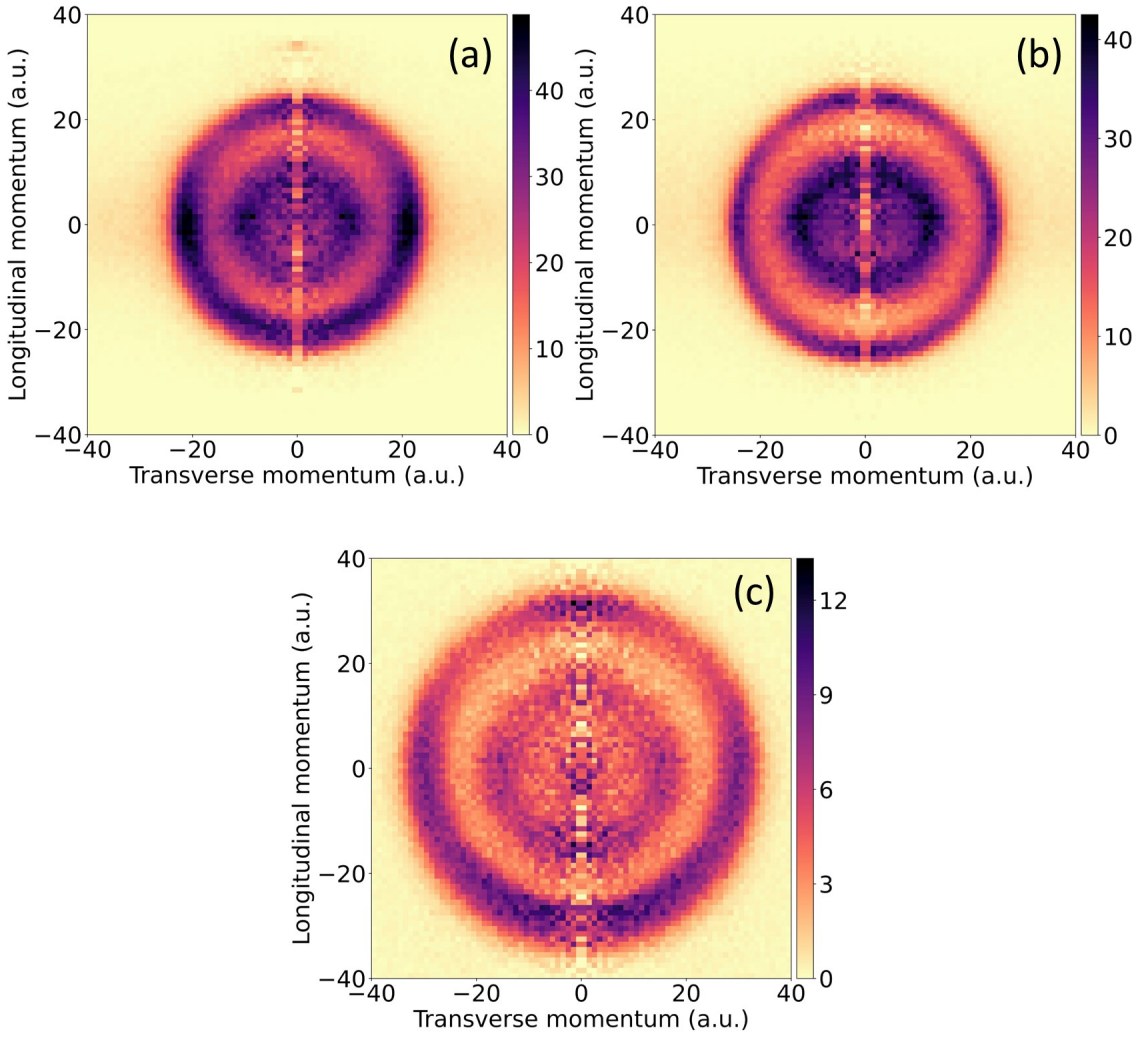

Figure 4.6: Momentum distribution of H^- and D^- ions from C-H/C-D bond cleavage of (a) CH_3COOH, (b) CH_3COOD, and (c) CD_3COOD at 9.1 eV. The incident electron momentum is in the positive longitudinal direction (upward)..

of the fast H^-/CH_3COOH breakups are generally highest in the perpendicular, forward, and backward directions. The slow H^- anions from DEA to CH_3COOH and CH_3COOD appear to be ejected almost isotropically, with a weak maximum in the perpendicular directions. In contrast, the slow D^- ions from DEA to CH_3COOD show a similar structure as the fast ions.

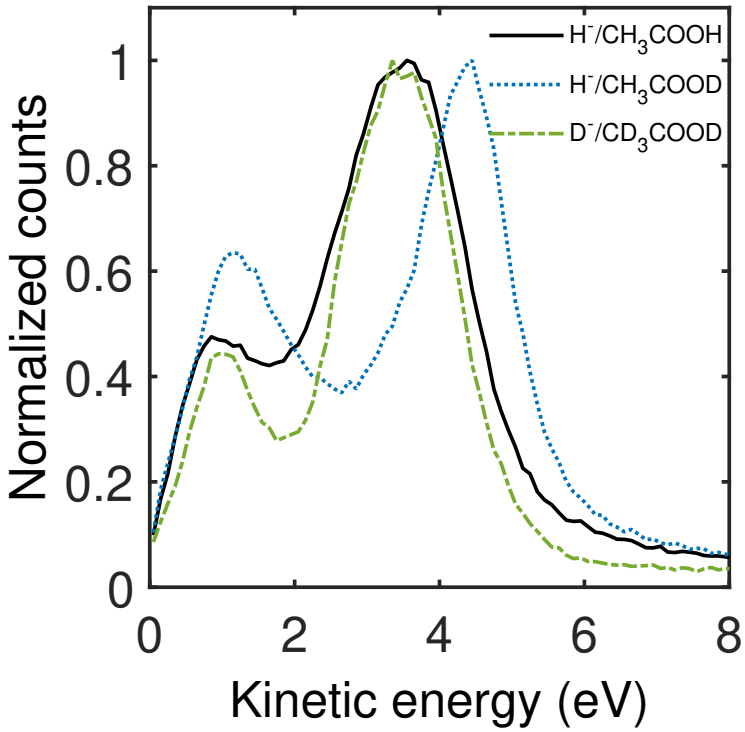

Figure 4.7: Kinetic energy distribution of H^- and D^- ions from C-H/C-D bond cleavage of DEA to CH_3COOH, CH_3COOD, and CD_3COOD at incident electron energies of 9.1 eV. The ion yield for each distribution is rescaled to a maximum of 1 (arbitrary units).

The kinetic energy distributions in Fig. 4.7 for the C-H (C-D) break show two distinctive peaks, corresponding to the outer peak (fast H^-/D^- ions) and the inner peak (slow ions) in Fig. 4.6. This general structure is exhibited by all three isotopologues in the present experiments. The pathway for C-H bond cleavage can be represented by Reaction 2 in Tab. 4.1, with a thermodynamic threshold of 3.47 eV. The slow H^-/D^- ion peaks valueall occur at about 1 eV, indicating that about 4.6 eV (corresponding to $\approx$ 82% of excess energy) is partitioned to excitation or few-body dissociation of the neutral fragment(s). The peak kinetic energy of the fast ions are 3.65, 4.45, and 3.35 eV for the H^-/CH_3COOH, H^-/CH_3COOD, and D^-/CD_3COOD

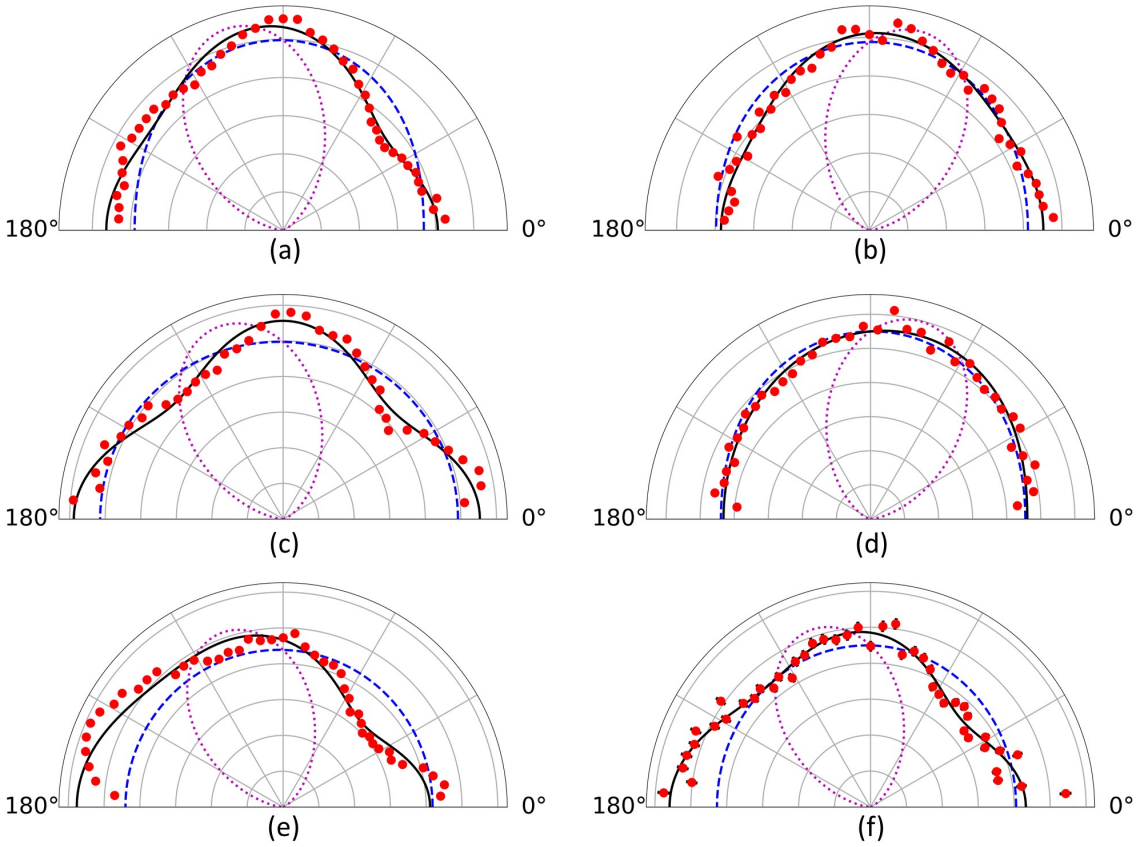

Figure 4.8: Angular distribution of H^- (D^-) ions from C-H (C-D) bond cleavage of DEA to CH_3COOH: (a) fast and (b) slow ions, CH_3COOD: (c) fast and (d) slow ions, and CD_3COOD: (e) fast and (f) slow ions at 9.1 eV. The experimental angular distributions (solid red circle) are fitted with the assumption of a $A' \rightarrow A'$ transition using partial waves s+p (dashed blue line) and s+p+d (solid black line), and under the assumption of a $A' \rightarrow A''$ transition using p+d (dotted purple line). The incident electron direction is 0 deg.

channels, respectively. The internal energy of each neutral fragment is in the range of 1.15 to 2.28 eV, corresponding to 20% to 40% of the excess energy.

We now consider H^- from 9.1 eV DEA to CH_3COOH (Fig. 4.6a), which, by comparison with Fig. 4.3c, clearly occurs mostly by C-H break. Fig. 4.8a shows the angular distributions of the fast (3.6 eV to 4.6 eV) H^- ions for this attachment energy. The distribution of Fig. 4.8a has a maximum around 90°, two shallow minima around 45° and 125°, and significant yields at0° and 180°. Applying the $s + p + d(A')$ model

(black curve) gives a reasonable fit to the measured distribution, with an R^2 value of 0.8. In contrast, the $p + d(A'')$ model (dotted purple curve) fails to capture the measured ion yield in the forward and backward directions, and the $s + p(A')$ model (dashed blue curve) fails to capture the forward-backward asymmetry . This suggests that the 9.1 eV resonance has A' symmetry. Similar features are also observed in angular distributions for fast H^- and D^- ions from CH_3COOD and CD_3COOD in Figs. 4.8c and 4.8e, which are each in good agreement with $s + p + d(A')$ model fits (black curves in Fig 4.8).

4.5 Discussion

To understand the dynamics of DEA to acetic acid, we consider the possible symmetries of the resonances, the measured angular distributions, and the possible final states of the dissociation products. First, we discuss the ground and low lying excited vibrational and electronic states of the radicals and their stability with respect to energy absorption in order to identify the dissociation pathways in the three resonance regions. Next, we compare our results with the photoabsorption spectrum of the acetic acid molecule, which was studied using VUV synchrotron radiation. We also consult the electron energy loss spectrum in order to illustrate the dissociation dynamics of the TNI state under the ARA approximation. Finally, we examine the possible electron attachment probability in the molecular frame (the entrance amplitude, within the axial recoil approximation) to acetic acid by comparing with the well studied Feshbach resonances in formic acid.

Photodetachment and photoelectron-photofragment coincident spectroscopy [133] were employed to study the dissociation dynamics of the neutral acetyloxyl radical,

CH_3COO, starting from the acetate anion (CH_3COO^-) equilibrium geometry. A stable neutral radical (CH_3COO or CH_2COOH) and dissociation products CH_3 and CO_2, were found following photodetachment. The branching ratio of 1:9 between the generation of a stable radical and a dissociation suggested that CH_3COO is metastable and undergoes spontaneous uni-molecular dissociation, rather than direct dissociative photodetachment. The study also found that the fragment CH_2COOH is the result of an isomerization process of CH_3COO after photodetachment. The exact path for hydrogen atom transfer is not known, but it was found to be energetically favorable [155, 156] with a barrier height of 0.08 eV between the lowest states of CH_3COO and CH_2COOH. The lowest few electronic states of the acetyloxyl have also been studied computationally. The ground electronic state has been characterized as a B_2-like $^2A''$ state, and the lowest excited electronic state was found to be only 0.1 eV to 0.2 eV higher in energy having $^2A'$ character [5]. The second excited electronic state is predicted to be about 0.7 eV above the ground state [157]. High-resolution photoelectron imaging of acetate anions [158] found two bound vibrational states around 0.048 eV and 0.066 eV above the ground state, where the first one is the O-C-O bending and the second one is the C-C in plane wagging mode. DFT calculations in Ref. [159] revealed that the CH_2COOH radical is unstable by 0.03 eV and will most likely dissociate into fragments the CH_3 and CO_2.

In the present experiments, for O-H/O-D bond breakage at 6.7 eV and 7.7 eV, the energies available for excitation of the neutral CH_3COO radical are approximately 0.25 eV and 1 eV, respectively. Such low internal energies are consistent with two-body fragmentation (Reaction 1 in Tab. 4.1), although several low-lying excited vibrational and electronic states are accessible at this energy. For the higher energy resonances at 9.1 eV and 10 eV, the energies partitioned into the neutral fragment are between 1.52 eV and 2.9 eV, suggesting a higher probability of isomerization and/or

dissociation of metastable CH_3COO [133].

Turning to the C-H/C-D bond breakage, it is implausible that the slow H^-/D^- ions are the result of two-body dissociation, because the energy deposited in CH_2COOH, CH_2COOD, and CD_2COOD would be 4.63 eV, 4.41 eV, and 4.62 eV, respectively. This large amount of internal energy is sufficient for direct three-body dissociation, as represented by dissociation reaction 3 in Tab. 4.1, where the thermodynamic threshold for this reaction is 3.39 eV. Yet, we cannot rule out that higher energetic thresholds of 5.46 eV and 7.99 eV (4 and 5 in Tab. 4.1) are at play. On the other hand, for the fast H^-/D^- ions at this energy, the internal energy of the fragments ranges from 1 eV to 3 eV, and the distribution is narrow. Therefore, we expect a prompt two-body fragmentation, where most of the available energy is funneled into translational kinetic energy, although the metastable neutral radical may subsequently undergo further dissociation. The branching ratios of C-H/CH_3COOH and C-D/CD_3COOD breaks to produce fast and slow H^- and D^- anions are roughly the same. It is around $4:1$, whereas for C-H/CH_3COOD break it is around 3:1.

The fits to the measured angular distributions (Figs 4.5 and 4.8) indicate that all four resonances, each corresponding to a distinct TNI state, have A' symmetry. However, due to their broad width of each resonance and their overlaps in energy, we do not rule out the possibility of A'' symmetry for the second and third resonances, because some of the A' character may be embedded by a nearby into each of those angular distributions. We note that the broad resonance widths [19] are comparable to the present electron beam energy resolution of (0.5 eV), and the intrinsic energy width of each resonance is primarily due to the projection of the ground state of the neutral molecule in the Franck-Condon region onto the repulsive potential energy surface of each TNI state[3]. To characterize each TNI resonance, we consider the

possible neutral parent states of the present Feshbach resonances from the VUV photoabsorption [6, 160, 161, 162, 163, 164] and EEL [165] spectra in the literature. We turn our attention now to the O-H/O-D break at the 6.7 eV resonance. Leach *et al.* [6] have reported two transitions just above 6.7 eV: (i) the valence transition $13a' \rightarrow 14a'$ at 6.669 eV (calculated) with an oscillator strength of 0.047, and (ii) the Rydberg transition $13a' \rightarrow 3sa'$ at 7.25 eV (experimental) with an oscillator strength of 0.02. They assigned the valence transition $13a' \rightarrow 14a'$ as the $n'_0 \rightarrow \sigma'_{OH}$ transition, which is the same as the $\tilde{A}' - X$ transition in the nomenclature of Bell *et al.* [160]. Robin [163] assigned the broad feature at 7.08 eV as an $n_0 \rightarrow 3s$ Rydberg transition. Ari *et al.* [165] assigned a feature in EELS at 7.1 eV to the $13a' \rightarrow 3sa'$ Rydberg transition, which appears to agree with Refs. [162, 163, 6]. Based on these studies, the valence state $(13a')^{-1}(14a')^1$ or Rydberg state $(13a')^{-1}(3sa')^1$ could be the parent TNI state of a Feshbach resonance. Therefore, in the 6.7 eV Feshbach resonance, the incident electron may excite the $13a'$ valence electron and be captured simultaneously either in the $14a'$ valence orbital or the $3sa'$ Rydberg orbital, giving the TNI state an A' symmetry. This indicates a possible mixed valence and Rydberg character in the first resonance.

The Rydberg optical transition to the 3s orbital in acetic acid shows a broad diffuse structure similar to the corresponding structure in formic acid [160, 6]. The maximum of the band in acetic acid is at 7.795 eV [6]. Leach *et al.* [6] further identified three valence transitions in their VUV photoabsorption measurements and calculations, although they were found to be one order of magnitude weaker than the Rydberg transition. We note also that the EELS [165] investigation found a prominent peak at 7.8 eV, which was assigned to a $\pi \rightarrow \pi^*$ transition. Since the symmetry of the 7.7 eV resonance is most likely A' (Fig. 4.5b), the parent is probably either the Rydberg state $(13a')^{-1}(3sa')^1$, or a mixture of Rydberg and valence $(3a'')^{-1}(4a'')^1$,

configurations.

We will now discuss 9.1 eV resonance, which dissociates by both O-H and C-H bond break. Three Rydberg bands, which are candidate parent TNI states of a Feshbach resonance at 9.1 eV, have been reported in spectroscopic studies [6] as the following transitions: $13a' \rightarrow 3da'$ at 8.948 eV, (ii) $13a' \rightarrow 4sa'$ at 8.994 eV, and (iii) $3a'' \rightarrow 3pa''$ at 9.268 eV. The first A' Rydberg transition $13a' \rightarrow 3da'$ is a weak band. The second A' Rydberg transition $13a' \rightarrow 4sa'$ was reported in the EELS study of Ari *et al.* [165], where this optical band starts at 9.0 eV. It was assigned to a $n_0 \rightarrow 4s$ transition. We consider the $(13a')^{-1}(4sa')^{1}$ state could be the parent state of a Feshbach resonance at 9.1 eV, consistent with the A' symmetry, which is evident in Figs. 4.5 and 4.8.

The two distinct momentum rings we observe at 10 eV for O-H scission from CH_3COOD in Fig. 4.3 suggest two different pathways leading to different ion momenta. Previous measurements [19] of the D^- yield from O-D bond breakage in CH_3COOD [19] show only weak contributions between 9 eV and 10 eV that manifest as a high energy shoulder of the 7.7 eV resonance. To understand the possible origins of the two rings, we consider first the possibility that O-D scission produces the acetyloxyl radical in two low-lying electronic states [5, 157]. It is possible that a conical intersection between two excited states of the neutral acetic acid in the third resonance leads to the two low-lying excited state of the acetyloxyl radical, analogous to the formyloxyl states produced by the A' resonance in formic acid [3]. The dependence of the relative yields of the two rings to the attachment energies above and below 10 eV suggests, however, that the inner ring is due to a contribution from the 9.1 eV resonance. We found that the inner ring yield decreases as the electron beam energy is increased above 9.1 eV, while the outer ring yield increases as the beam energy is increased from 9.1 eV and 10 eV.

We have not found any previous reports of the 10 eV TNI resonance observed as the outer ring in Fig. 4.3. A corresponding parent neutral state could be populated by any of the following Rydberg transitions [6]: (i) $13a' \rightarrow 4pa'$ at 9.435 eV, (ii) $13a' \rightarrow 4da'$ at 9.695 eV, and (iii) $13a' \rightarrow 5sa'$ at 9.78 eV. Notably, the 10 eV resonance has around 1 eV higher KER than the 9 eV resonance, which suggests that both resonances produce acetyloxyl in the ground electronic state.

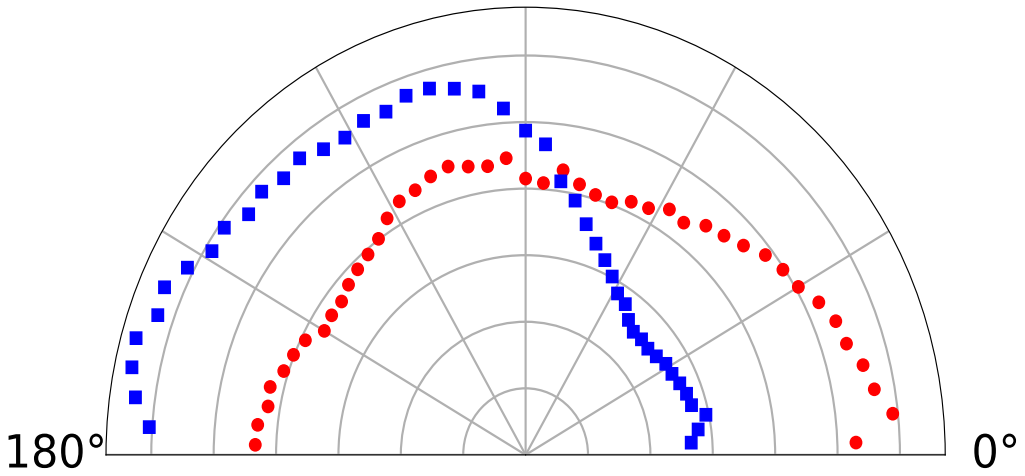

Figure 4.9: Measured H^- angular distribution from O-H bond breakage for the 7.7 eV electron attachment resonance in acetic acid CH_3COOH (blue square) compared with the corresponding angular distribution at 7.25 eV in partially deuterated formic acid, DCOOH (red circle).

We now consider the effect of methylation on the DEA resonances and dynamics by a comparison between acetic acid and formic acid, which was studied previously by anion fragment momentum imaging [3]. In Fig. 4.9, we compare the angular distributions of H^- for O-H bond breakage at 7.25 eV and 7.7 eV for DCOOH and CH_3COOH, respectively. In CH_3COOH, we observe that the emission of the H^- fragment mainly occurs in the backward direction near 180°. In contrast, the H^- from DCOOH is emitted mainly in the forward direction near 0°, i.e., in the direction of the electron beam. The squared modulus of the 3D entrance amplitude [3] (the electron

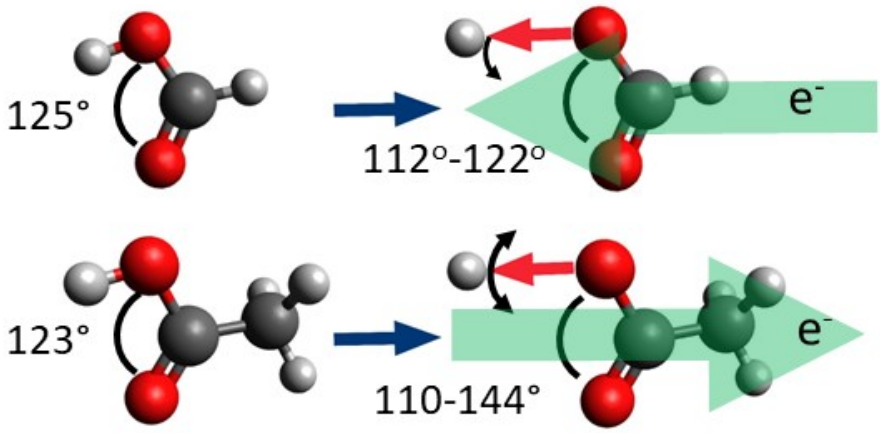

Figure 4.10: Comparison of the maximum probability of attaching an electron to formic acid [3] and acetic acid. The red arrow represents the O-H dissociation axis. The green arrow indicates the preferred electron attachment direction for generating the measured angular distribution in Fig. 4.9. The O-C-O bond angles for the ground and low-lying electronic states are taken from [4, 5, 6].

attachment probability in the molecular frame) for O-H bond breakage from the lowest $^2A'$ Feshbach resonance in formic acid shows that electrons have a maximum probability for attaching to the molecule when the O-H direction is parallel to the incident electron beam direction (top sketch in Fig. 4.10). A similar comparison can be made for the 6.7 eV resonance in CD_3COOD with the 7.25 eV resonance in HCOOD. The general trend is that the angular distributions of H^- from CH_3COOH and DCOOH resemble mirror images of each other (Fig. 4.10). In acetic acid, the O−C=O equilibrium bond angle is 123° [166, 6]. The electronic structure study in Ref. [5] has shown that, at their optimized geometries, the ground state of the acetyloxyl radical as well as the low-lying excited states all have C_s symmetry, and the O−C=O bond angles vary from $110 - 141°$, which suggests some rotation of the O-H bond is likely as the acetic acid TNI dissociates by O-H break. If such rotation is sufficiently small the the ARA is remains valid, and we find electron attachment

probability is highest when the O-H bond is aligned antiparallel to the incident beam, as depicted in the bottom sketch of Fig. 4.10, in contrast with formic acid. This could possibly be confirmed by future *ab initio* electron scattering calculations.

4.6 Conclusion

We have presented the results of the 3D anion momentum imaging measurements of DEA to acetic acid and its partially and fully deuterated forms, leading to H^-/D^- fragments from O-H/O-D and C-H/C-D bond scissions at four resonance energies spanning 6.7 eV to 10 eV. We also measured the kinetic energy and angular distributions of the H^- and D^- anions. The energy partitioning indicates mostly two-body dissociation for O-H/O-D bond breakage at all energies, whereas the C-H/C-D bond breakage at the 9.1 eV resonance indicates the involvement of both two- and three-body dissociation with a branching ratio of 4:1 for both CH_3COOH and CD_3COOD, and 3:1 for CH_3COOD. The anion fragment angular distributions were analyzed under the assumption that the axial recoil approximation holds, in order to determine the most likely symmetries of each TNI electronic state. The angular distributions are found to be consistent with all four resonances having A' symmetry. We note that, due to the energy-overlapping nature of these resonances, contributions from A'' symmetry, particularly above 7.7 eV, should not be ruled out. Both the 6.7 eV and 7.7 eV Feshbach resonances are tentatively assigned as having mixed valence and Rydberg character. By comparing the present experimental results with recent experimental and theoretical investigations of formic acid, we find that the 9.1 eV resonance proceeds via both O-H and C-H bond scission. For O-D bond breakage from CH_3COOD at 10 eV, where we observe two distinct D^- momentum rings, providing strong evidence for a fourth A' resonance that, to our knowledge, has not been

previously reported. Finally, we conclude that electron attachment to acetic acid for all four resonances is generally most likely to take place in the molecular plane with the methyl functional group in the forward direction relative to the incident electron. This contrasts with the A' resonance in formic acid, where the electron attachment amplitude is highest when the hydroxyl functional group is in the forward direction.

Chapter 5

Dissociative Electron Attachment to 1-Methyl-5-NitroImidazole

5.1 Introduction

Radiation therapy is commonly employed to control or destroy tumor cells by damaging the DNA and is often combined with other treatments, such as surgery, chemotherapy, or immunotherapy to treat various common types of tumors [167, 168]. Hypoxic tumors, which are solid tumors with oxygen-deficient regions, resist radiation therapy because their oxygen levels are lower than those of the normal tissue from which they emerged [169]. One way to enhance the effectiveness of radiation therapy is by using radiosensitizers. A radiosensitizer selectively attaches to tumor cells, and when exposed to high-energy radiation (e.g., electrons, protons, X-rays, or γ-rays), it leads to the selective destruction of these cells, with minimal or no effect on healthy tissue [170]. The molecular mechanism by which radiosensitizers operate is not yet fully understood and remains a subject of intense research. Most high-energy radiation, when deposited, ionizes the cells, producing secondary free electrons with energies between 1-20 eV [171, 172]. It is likely that reactions induced by low-energy electrons, involving dissociative electron attachment (DEA), play a significant role [173]. During radiation therapy treatment, the radicals or ions generated through

DEA from the radiosensitizer will attack the solid tumor cells growing in hypoxic cells, effectively destroying it.

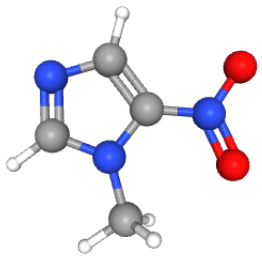

Figure 5.1: Molecular structure of 1-Methyl-5-NitroImidazole ($C_4H_5N_3O_2$).

The goal of this project is to generate a data set of the anion fragments produced by low energy electron attachment to 1-Methyl-5-NitroImidazole (1M5NI) whose structure is shown in Fig 5.1. This research is crucial for understanding the mechanisms of molecular radiosensitizers, as their damaging effects are closely linked to the formation of anionic fragments and radicals during electron induced molecular dissociation. The data set can be used for modeling electron induced radiation damage at the molecular level to biologically relevant media containing 1M5NI as a potential radiosensitizers.

In this study, we focus on direct measurements of anion fragment yields from various bond breaking in 1M5NI. For this, we carried out anion fragment momentum imaging experiments on 1M5NI at the energy range from 3.1 eV to 4.7 eV. We also examined the kinetic energy of the fragments measured from the extracted absolute momenta. The material in this chapter is now published in Ref. [7].

5.2 Experimental Setup

The experimental apparatus used in the present study has been described in detail previously in Ref. [2] and in section 4.2, thus, we include here only the information most relevant to the present experiment. Briefly, an effusive molecular jet was generated using a stainless-steel capillary, which intersected orthogonally with a pulsed electron beam in a coaxial magnetic field inside the spectrometer. At one end of a gas manifold system, approximately 10 g of 1M5NI was placed in a glass sample holder and heated to around $40 - 50$°C. The gas manifold feeding the gas jet capillary was gradually heated to a maximum temperature of (< 80°C) allowing the sublimated 1M5NI vapor to accumulate in the gas manifold to a pressure of 10-100 mTorr before introducing the gas into the sample gas inlet and capillary. The electron beam energy spread (0.5 eV full width at half maximum) and absolute electron beam energy was determined and verified before and after the experiments by measuring the ion yield across the thermodynamic threshold for O^- production from CO_2. Anion fragment momentum was calibrated against the well known O^- momentum distribution from DEA to O_2. A time- and position-sensitive multichannel plate detector with delay-line recorded the time-of-flight and positions of each ion hit in an event list. Following each experiment, the raw position and time data were sorted and converted to momenta.

5.3 Results and Discussion

The mass-resolved anion yields from dissociative electron attachment to 1M5NI within the resonance energy range of $3.1 - 4.7$ eV are shown in Fig 5.2. The predominant anions observed are $NO_2{}^-$ and CN^-, followed by heavier anions resulting from the loss of neutral radicals such as O, OH, CH_3, NO, and/or NO_2. These observations

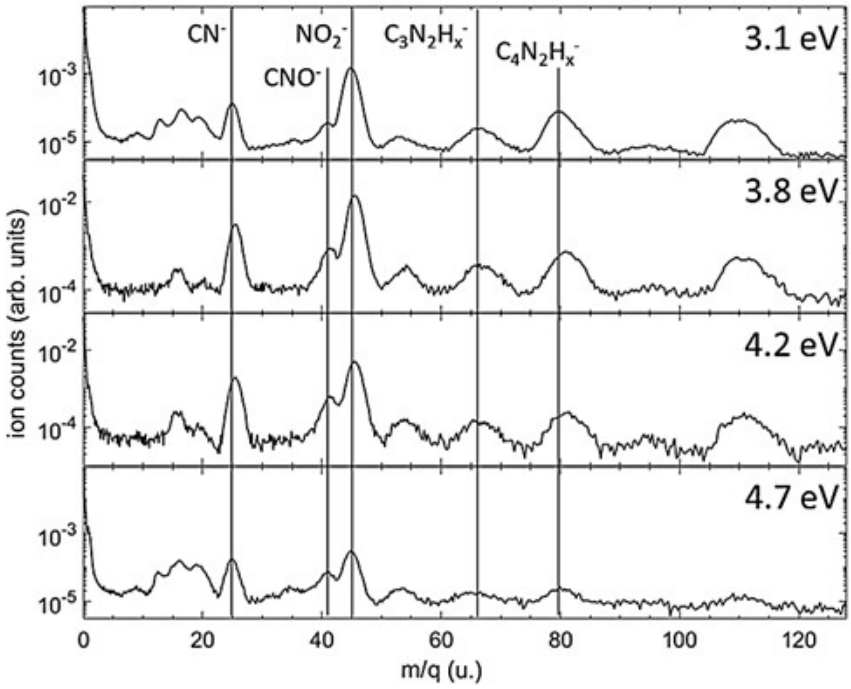

Figure 5.2: The relative yields of anionic fragments resulting from dissociative electron attachment to 1M5NI at four distinct incident energies are shown in time-of-flight mass spectra [7]. The vertical scale, representing the number of ions on a logarithmic scale, is not normalized between the four electron energies. Vertical lines are used to denote the most prominent anion fragments. The region around 16 a.m.u is due to contamination from DEA to H_2O, O_2, and CO_2, all of which produce O^- following electron attachment on the high-energy side of the electron beam energy distribution.

are consistent with the findings reported by Tanzer *et al.* [174]. It is important to note that the mass resolution ($\frac{m}{\Delta m} \simeq 20$) of the current momentum imaging spectrometer does not allow for precise determination of the remaining number of hydrogen atoms in most cases. No significant production of H^- is observed from the molecule at the electron attachment energies. The 3.1 and 4.7 eV measurements reveal a small peak at $\frac{m}{q} = 35u$ which may be attributed to either $C_3{}^-$ or $H_2O_2{}^-$. Additionally, a peak around $\frac{m}{q} = 54u$ is evident at all energies, likely due to $C_2N_2H_x{}^-$, where $x = 1, 2, 3$.

The branching ratios (BRs) represent the percentage of a specific anion relative

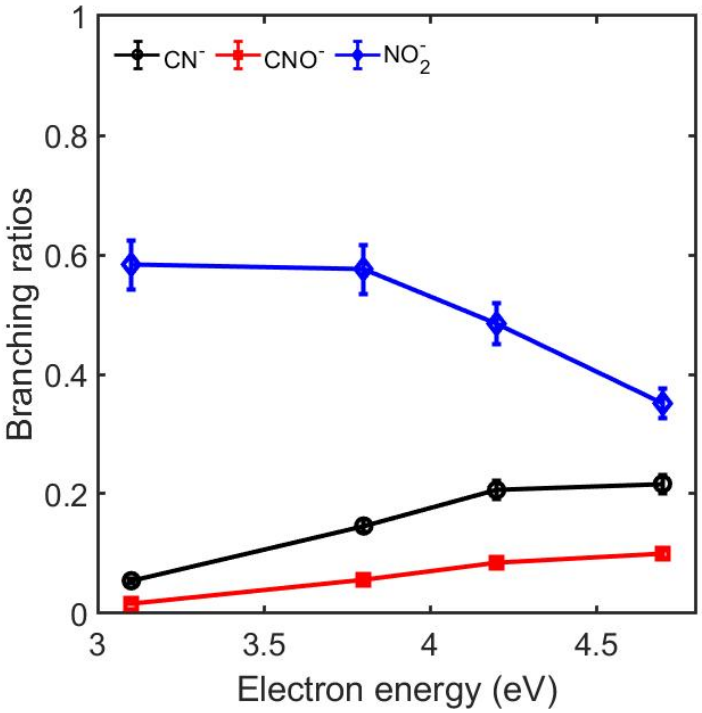

Figure 5.3: The branching ratios of the negative ions CN^- (black), CNO^- (red), and NO_2^- as a function of electron energy.

to the total detected fragmentation pathways. In Figs. 5.3, the measured BRs of the fragment anions CN^-, CNO^-, and NO_2^- as a function of energy are shown. At an electron energy of 3.1 eV, NO_2^- made up approximately 58% of the total anion yield, decreasing to about 35% at 4.7 eV. The maximum of NO_2^- ion yield appeared around 3 eV and decreased with increasing electron energy [174], consistent with the observed decrease in BR for NO_2^-. In contrast, as the electron energy increases, the BRs for CN^- and CNO^- increases, reaching a maximum of 21% and 10%, respectively. The BRs for the other anions in Fig 5.4, show little increase between 4.2 and 4.7 eV. Although none of these fragments contribute more than 10% individually, their combined yield accounts for 23-30% of the total anion yield. Fig. 5.5 displays the kinetic energy distributions for the four most abundant anions produced in DEA to 1M5NI at 3.1 and 4.2 eV electron energies. The inset in each panel presents a cen-

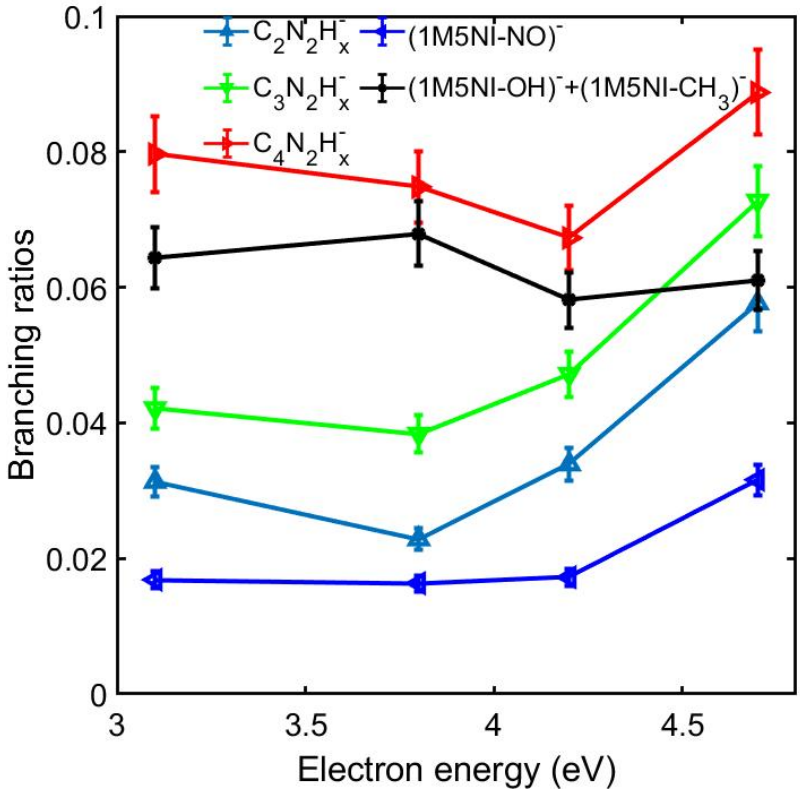

Figure 5.4: The branching ratios of the negative ions $C_2N_2Hx^-$ (dark cyan), $C_3N_2Hx^-$ (green), $C_4N_2Hx^-$ (red), NO loss (blue), and sum of OH and CH_3 loss (black) as a function of electron energy.

tral slice of the three-dimensional momentum distribution, revealing highly isotropic anion momentum. The kinetic energy distributions of all the anion fragments peak near zero eV. They exhibit minimal variation across the range of incident electron energies examined. It is noticeable that the kinetic energy distributions of CN^- is considerably broader compared to NO_2^- and the heavier fragments, suggesting a three-body breakup or a stochastic dissociation mechanism for CN^- kinetic energy. The dissociation of CN^- requires significant motion or rearrangement of the C_3N_3 ring, NO_2, or CH_3 moieties. This is in contrast to the dominant NO_2^- dissociation, which likely involves only the stretching of the nitro C−N bond.

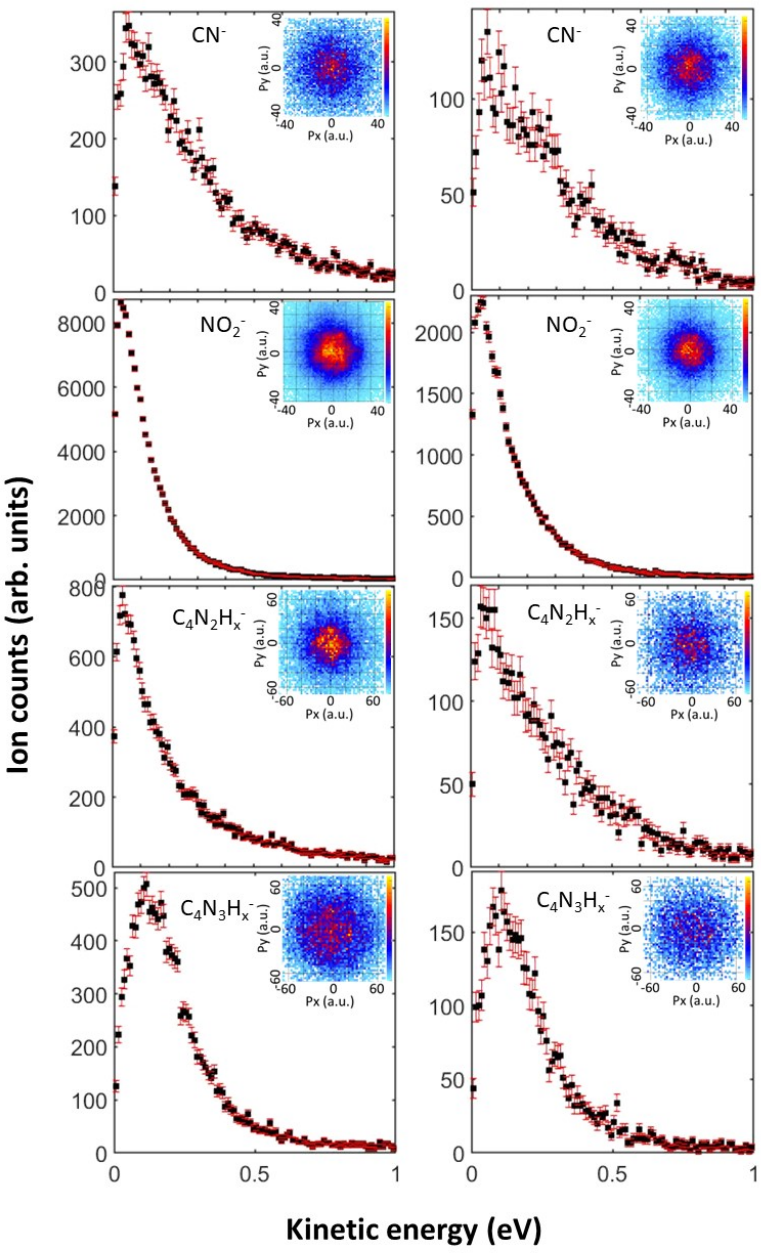

Figure 5.5: The kinetic energy distributions of the anion fragments and momentum-slices (insets) in atomic unit (a.u.) at an electron energy of 3.1 eV (left panel) and 4.2 eV (right panel). The incident electron is directed in the +Py direction in the momentum image.

5.4 Conclusion

We have presented the results of the anion momentum imaging measurements of DEA to 1M5NI at the energy range from 3.1 eV to 4.7 eV. We have identified the

eight fragment anions, though the exact hydrogen loss was not determined. From the branching ratio calculations, NO_2^- and CN^- are found to be the most abundant anions. The kinetic energy distributions of the fragment anions show a broad peak near-zero kinetic energy.

In summary, the generation of anion fragments and radicals from low energy electron attachment to 1M5NI suggests its potential applicability as radiosensitizer. The radicals produced by electron induced dissociation can increase oxygen levels around hypoxic tumors that can further increase the efficiency of the the radiation therapy.

Chapter 6

Conclusions

This chapter summarizes my contributions to the development of the experimental apparatus and presents demonstrations of electron- and photon-based experiments designed to study dissociative electron attachment.

In Chapter 1, I present my motivation for studying multiphoton ionization of ion-molecule clusters and how it is similar to dissociative electron attachment (DEA) studies. I describe the transient negative ion (TNI) formation and how it decays through either DEA and autodetachment. Later, I review charge transfer dissociation of ion-molecule clusters and how this idea can be extended to explore for multiphoton absorption case to access the distinct transient anion states. Lastly, a brief history of multiphoton ionization of atom, molecule, and molecular anions are reviewed.

In Chapter 2, I describe the ion-molecule cluster beam apparatus for multiphoton study. I start with cluster generation and describe how an improved temporal resolution of the parent anion pulse at the interaction region can be obtained by optimizing the experimental parameters of the time-of-flight (TOF) mass spectrometer. We get the mass resolution of the parent anion of 275. This resolution is relatively high compared to the similar apparatus [46]. despite the compactness of our apparatus. Next, I discuss the design perspectives and SIMION simulation of the reflectron TOF mass spectrometer. The reflectron TOF mass spectrometer is used to mass resolve

the fragment anions after photoexcitation. Following that, I describe the laser pulse characterization and overlap procedure of the laser and parent anion beam at the interaction region. Finally, the data acquisition and preprocessing procedure TOF data is presented. In this section, I describe how to subtract the background appearing in the TOF spectrum. The background subtracted TOF spectrum was clean enough (within statistical uncertainty) that we observe five different peaks and identified using SIMION simulation.

The content of Chapter 3 focuses on the multiphoton excitation of ion-molecule dimer $CF_3I \cdot I^-$ at different laser intensities. We observe five fragment anions and total yield of neutral. Among these fragments I^-, CF_3I^-, and $I_2{}^-$ were observed in single photon absorption of $CF_3I \cdot I^-$ at energies between 3.90 eV and 4.77 eV, around the electron detachment threshold of the dimer anion [111]. The fragment anions $CF_3{}^-$ and I^- observed in our multiphoton experiment were also observed in the DEA study to CF_3I. We see that the ratio (fragment counts/parent counts) increases with increasing intensity except for $I_2{}^-$ which becomes a plateau at higher intensities. We predict that at higher intensities other mechanisms such as dissociation or electron detachment dominate, both of which could compete with $I_2{}^-$ production.

The number of photons absorbed in the dissociation process shows that a varying number of photons are absorbed for each fragment channels. We compared this result with the DEA study and found that two different TNI states were accessed by absorbing three and two photons for the channels $CF_3{}^-$ and I^-, respectively. These two TNI states appeared around 0 eV and 4 eV, respectively. We conclude that different excited states were accessed during multiphoton absorption of $Cf_3I \cdot I^-$, and each of these states may not be accessible in single photon excitation.

In Chapter 4, we investigate the TNIs formed by DEA to acetic acid in the dissociation channel H^-. I describe the experimental apparatus used for this experiment

located at Lawrence Berkeley National Laboratory. Here, we extract the kinetic energy and angular distributions from momentum distributions. To distinguish the O−H and C−H channels, we also carried out experiments on partially deuterated acetic acid on hydroxyl site. Among the three previously observed resonances, the first two at 6.7 eV and 7.7 eV are found to dissociate exclusively by O−H bond, whereas the 9.1 eV resonance dissociates by C−H and C−H bond break. We identified a previously unreported resonance at 10 eV that dissociated by O−H break. The measured kinetic energy distribution indicates primarily two-body dissociation producing a neutral radical in its ground states. The angular distributions of the anion fragment are analyzed under axial recoil approximation to find the symmetries of each TNI electronic state. The high kinetic energy release and structured angular distributions both suggest prompt dissociation, such that the axial recoil approximation may hold for all four resonances. The angular distributions of all the four resonances are found to be consistent with A' symmetry , which allows tentative assignments of their electronic configurations, based on previous VUV absorption spectra and electron energy loss spectra [6, 165].

In Chapter 5, we examine the anion fragment yields resulting from DEA to 1-M-5-Nitroimidazole (1M5NI). Here we provide the relative abundances and kinetic energies of the anionic fragments. These data are valuable for simulating electron-induced radiation damage in biological systems containing 1M5NI.

Appendix A

Matlab and SIMION code for the linear plus quadratic reflectron mass spectrometer design.

The code energy.m is used to calculate the energy of the fragment anions based on the energy of the parent anion.

```
clc
u= 1.66e-27; %mass of proton in kg
m1 = 188*u;  %mass of ion in kg ; me=0.00054858
e= 1.6e-19;  %charge of electron or proton
%Energy in Joule or C.V (coulomb.Volt)
Ek1= [2600*e, 2700*e, 2800*e] ;
data=csvread('mass1to323.csv');
mass=data.';
n=numel(mass)
%mass = [1,2,3,4]
m2 = mass*u;
temp_E=[];      %(1,2)
for j=1:n       %max(m2)
    E=zeros(1,3);
```

```
        for i=1:3;
            v1=sqrt(2*Ek1(i)/m1) ; %Velocity in mm/s
            Ek=(0.5*m2(j)*v1^2)/e;
            E(i) = Ek;
        end
    temp_E=[temp_E, [E]]
end
E_all=reshape(temp_E, [3,n])
D_E = E_all(3,:)-E_all(2,:)
E_central_d=E_all(2,:);
E_central=[mass.', E_central_d.'];
E_spread_d=E_all([1,end],:);
E_spread =[mass.', E_spread_d.'];
E_d= [mass.', E_central_d.', E_spread_d.', D_E.']
E=array2table(E_d, 'VariableNames', {'Mass',
 'Central-Energy', 'Lower-Spread',
 'Upper-Spread', '+-spread'})
csvwrite('central_energy_323.csv', E_central_d)
csvwrite('energy_spread_323.csv', D_E)
writetable(array2table(E_d, 'VariableNames',
 {'Mass','Central-Energy',...
 'Lower-Spread', 'Upper-Spread', '+-spread'}),
 'C:\Users\data_323.txt')
```

The program Yoshida.m will calculate the optimized voltages of each electrodes for a particular mass.

```
% Change V1 and Ek in such a way that the ratio
% becomes 0.7718 for a certain max voltage desired.
% Set Physical parameters
u = 1.66e-27; %mass of proton in kg
%m1 = 188*u;  %mass of ion in kg
e= 1.6e-19;   %charge of electron or proton
%Ek= 2700*e ; %Energy in Joule or C.V (coulomb.Volt)
%Ek=(2700/3000)*max voltage
Ek= 2700 ;     %Energy in V (Volt)
V1 = 1307 ;
%delEk = 20 ;
%quadratuc voltage = energy of ion in volt
L = 65;  %Depth of Reflectron (mm)
d1= 55;  %source to reflectron distance (mm)
d2=15;   %reflectron to detector distance (mm)
%v1=1000*sqrt(2*Ek1/m1)        %Velocity in mm/s
%finding the linear voltage
alp = sqrt(1-((d1+d2)/L)^2*(V1/Ek));
V2 = 2*(L/(d1+d2))*Ek*[1-alp]
%calculating resolving power or resolution (m/dm)
a1 = (L/(d1+d2))* sqrt(Ek/V1);
a2 = pi - 2*atan((V2/(2*sqrt(Ek*V1))));
a3 = 1-((d1+d2)/L)*(V1/V2);
resol = ((2*(1+a1*a2))/a3)*(Ek/delEk)^2
ratio=V1/V2
```

```
%Finding the constant parameters 'a' and 'b'
a = (2*V1)/(L^2);
b=V2/L;
x1=[13, 26, 39, 52, 65];
V=zeros(1,5);
for i=1:5;
    Vx=b*x1(i)+0.5*a*(x1(i))^2;
    V(i)=Vx;
end
disp(V);
```

The program circuit.m will calculate the resistances in each electrode.

```
clc
%voltage divider formula
%V_out = (V_s . R2)/(R1+R2),
%R2 is the electrode voltage.
%We will fix R1, R2, and V_out to get V_s
R1 = 1e06;
R2 = 120e6;
%Vout = 4650;
% Vs = Vout*(R1+R2)/R2
% current = Vs/(R1+R2)
% Power= Vs.*current
% Electrode voltages, EV
data=csvread('electrode_voltage_thesis.csv');
%M13     M37     M44     M188
```

```
%27      76.9     91.54    391
%61.3    174.3    207.56   886.5
%102.8   292.3    348       1486.6
%151.5   430.9    513       2191.3
%207.5   590      702.5    3000.5
EV=data
Vout = data(5,:)
%Total resistance of the all the elecrodes, R2.
%Each electrode voltage is
%designated as R or R(i)
%RT=25e6;
R =[];
for i=1:4;
    Rs = (EV(:,i)*R2)/Vout(i)
    R = [R,Rs];
    %P(i+1)= Rs-P(i);
end
disp(R)
disp(R(:,1))
diff(R)
R(1,:)
Res= cat(1,R(1,:), diff(R))
Resistance = Res.'
```

The SIMION geometry files for trajectory simulations.

1. The main geometry file LPR_Reflectron.gem

```
;scale 1 mm / grid unit
pa_define(1000,500,500,p,none)
;vacuum chamber walls
locate(0,200,200)
     {electrode(0)
{rotate_fill(360){within{box(0,0,1,199)};left side wall
within{box(958,0,960,199)} ;right side wall
}}}
;Electrode 1 this is shell around the extracting plate
locate(84,200,200)
{ electrode(1)
{rotate_fill(360)
{within{box(0,0,2,71)}
within{box(2,68,17,71)}
within{box(44,68,192,71)}
}}}
;Electrode 2, 3 , 4 TOF extracting plates
locate(99,200,200){
locate(0,0){electrode(2){
rotate_fill(360){within{box(0,0,2,58)}}}}
locate(28,0){electrode(3){
rotate_fill(360){within{box(0,9,2,58)}}
rotate_edge_fill(360){within{box(0,0,2,9)}}}}
locate(46,0){electrode(4){
rotate_fill(360){within{box(0,9,2,58)}}
```

```
rotate_edge_fill(360){within{box(0,0,2,9)}}}}}

;Electrode 5
locate(184,200,200)
{ electrode(5)  ;
{rotate_fill(360) {within{box(0,30,136,33)} }}}


;Einzel lens set: electrodes  6 7 8
locate(188,200,200) {
locate(0,0){ electrode(6){rotate_fill(360)
{within{box(0,20,40,28)} }}}
locate(44,0){ electrode(7){rotate_fill(360)
{within{box(0,20,40,28)} }}}
locate(88,0){ electrode(8){rotate_fill(360)
{within{box(0,20,40,28)} }}}}
; Deflectors after Einzel lens: electrode 9 10 11 12
locate(342,200,200){e(9){ include(DeflectingPlate1)}}
locate(342,200,200){e(10){ include(DeflectingPlate2)}}
locate(342,200,200){e(11){ include(DeflectingPlate3)}}
locate(342,200,200){e(12){ include(DeflectingPlate4)}}
;chamber wall 1
locate(276,200,200){electrode(0)
{rotate_fill(360){within{box(0,47,4,199)} }}}
;Mass gate : electrodes 13 14 15
```

```
locate(710,200,200){
locate(0,0){electrode(13){rotate_fill(360)
{within{box(0,4,2,30)}}
rotate_edge_fill(360){within{box(0,0,2,4)}}}}
locate(12,0){electrode(14){rotate_fill(360)
{within{box(0,4,2,30)}}
rotate_edge_fill(360){within{box(0,0,2,4)}}}}
locate(24,0){electrode(15){rotate_fill(360)
{within{box(0,4,2,30)}}
rotate_edge_fill(360){within{box(0,0,2,4)}}}}}
locate(707,200,200) {
electrode(0){
rotate_fill(360){within{box(0,4,1,35)}
within{box(2,33,32,35)}}}}
;chamber wall 2
locate(585,200,200){
electrode(0) {rotate_fill(360){within{box(0,10,4,199)} }}}
locate(795,200,200,1,-8,0,0){
locate(55,0,-25)
{e(0) { locate(0,0,0)
{ include(Reflectron_front_plate)}}
e(16) { locate(13,0,0)
{include(Reflectron_middle_plate)}}
e(17) { locate(26,0,0)
{include(Reflectron_middle_plate)}}
```

```
e(18) { locate(39,0,0)
{include(Reflectron_middle_plate)}}
e(19) { locate(52,0,0)
{include(Reflectron_middle_plate)}}
e(20) { locate(65,0,0)
{include(Reflectron_front_plate)}}
e(0) { locate(72,0,0)
{include(Reflectron_front_plate)}}
e(0) { locate(0,0,0)
 {include(Reflectron_shield)}}}}
```

2. Reflectron_shield.gem

```
;Deflection front plate and end plate with mesh
locate(0,0,0){
rotate_fill(360){within{box(0,63,80,65)}}
rotate_fill(360){within{box(78,26,80,65)}}}
```

3. Reflectron_front_plate.gem

```
locate(0,0,0){
rotate_fill(360){within{box(0,26,2,60)}}
rotate_edge_fill(360){within{box(0,0,2,25)}}}
```

4. Reflectron_middle_plate.gem

```
 rotate_fill(360){within{box(0,26,2,60)}}
```

5. DeflectingPlate1.gem

```
locate(,,,,,,-90)
{fill{within{ box3d(0,30,-25,20,37,25)}}}
```

6. DeflectingPlate2.gem

```
locate(,,,,,,0)
{fill{within{ box3d(0,30,-25,20,37,25)}}}
```

7. DeflectingPlate3.gem

```
locate(,,,,,,90)
{fill{within{box3d(0,30,-25,20,37,25)}}}
```

8. DeflectingPlate4.gem

```
locate(,,,,,,180)
{fill{within{box3d(0,30,-25,20,37,25)}}}
```

Appendix B

Matlab code for the data analysis of the multiphoton dissociation project.

The code test_tof_data_analysis_CF3I.m is used to present the data in structured arrays.

```
clearvars
clc
close all
% Specify the folder where the files live.
myFolder = '~\bkg\';
%myFolder = '~\bkg\';
% Get a list of all files in the folder with
%the desired file name pattern.
filePattern = fullfile(myFolder,
'delay_606ns_500s_1_laser_bkg.lmf.txt');
% Change to whatever pattern you need.
theFiles = dir(filePattern);
all_data=[];
for k = 1 : length(theFiles)
```

```
baseFileName = theFiles(k).name;
fullFileName = fullfile(theFiles(k).folder, baseFileName)
fprintf(1, 'Now reading %s\n', fullFileName);
fid = fopen(fullFileName,'r');
for i = 1:9
    line_ex = fgetl(fid);
end
%textscan is not as efficient as repeat fgetl multiple times.
N = uint32(fscanf(fid, ['Number of events =' '%u']));
Data(N) = struct('T',[],'dT',[],'Ch1_hits',[],'Ch1_ToA',[],
 'Ch2_hits',[],'Ch2_ToA',[],'Ch3_hits',[],
 'Ch3_ToA',[],'Ch4_hits',[],'Ch4_ToA',[]);
for i = 1:7
    line_ex = fgetl(fid);
end
while i < N
    i = fscanf(fid, ['--------#' '%u']);
    line_ex = fgetl(fid);
    Data(i).T = fscanf(fid, ['T = ' '%f'])/1e9;
    line_ex = fgetl(fid);
    Data(i).dT = fscanf(fid, ['dT = ' '%f'])/1e9;
    line_ex = fgetl(fid);
    line_ex = fgetl(fid);
    X = str2num(line_ex(11:end));
    Data(i).Ch1_hits = X(1);
```

```
        Data(i).Ch1_ToA = X(2:end);
        line_ex = fgetl(fid);
        X = str2num(line_ex(11:end));
        Data(i).Ch2_hits = X(1);
        Data(i).Ch2_ToA = X(2:end);
        line_ex = fgetl(fid);
        X = str2num(line_ex(11:end));
        Data(i).Ch3_hits = X(1);
        Data(i).Ch3_ToA = X(2:end);
        line_ex = fgetl(fid);
        X = str2num(line_ex(11:end));
        Data(i).Ch4_hits = X(1);
        Data(i).Ch4_ToA = X(2:end);
        line_ex = fgetl(fid);
        line_ex = fgetl(fid);
    end
    allValues = uint32([Data.Ch1_ToA]);
    N_counts=length(allValues)
    %[Y,X] = groupcounts(allValues.');
    X =double(allValues)*5e-4;
    length(X)
    fclose(fid);
    end
    lim=[20  26]
    ind =X > lim(1) & X < lim(2);
```

```
s_range=X(ind);
count_lim=sum(ind)
figure()
 edges = [20 :0.005: 26];
h=histogram(X,edges);
%histfit(X,edges)
 xlim([20, 26]);
 %xlim([22, 26]);
 ylim([0, 200]);
 ax = gca;
ax.FontSize = 20;
ax.LineWidth=1;
%ax.YTickLabel=[];
pbaspect([1 1 1])
xlabel('ToF-/-\mus','fontsize',16)
ylabel('Counts','fontsize',16)
ind1 = X > 20 & X < 26;
test_606_laser_bkg_neutral=X(ind1);
save("test_606_laser_bkg_neutral.mat",
"test_606_laser_bkg_neutral")
```

The code counts_isolate.m is used to separate the laser on and laser off data from structured array.

```
 clearvars
clc
close all
```

```
load('~\DataAnalysis\10072023\delay\delay_746ns_500s.mat');
whos ("-file", "delay_746ns_500s.mat")

% load('~\delay_3ms581us_746ns_1000s_45p4mW.mat');
% whos ("-file", "delay_3ms581us_746ns_1000s_45p4mW.mat")

lowlim = 24.3/5e-4;
highlim=24.6/5e-4;
lowerbound=18.4;  %24;
upperbound=19.0;  %26;
count_trigno1=str2num(append(num2str(
    [Data(1).Ch3_ToA]),''))*5e-4
count_trigno2=str2num(append(num2str(
    [Data(2).Ch3_ToA]),''))*5e-4
index1=find(count_trigno1 >
    lowerbound & count_trigno1 < upperbound)
index2=find(count_trigno2 >
    lowerbound & count_trigno2 < upperbound)
index1=double(isempty(index1))
index2=double(isempty(index2))

 M=Data(end).trigno
 if rem(M,2) == 0
        M=M
 else
```

```
    M=M-1
end

if (index1 ==0) && (index2==1)
    Ch3(M/2) = struct('laser',[], 'anion',[]);
    for k=1:M/2
        m=2*k-1;
        n=2*k;
        Ch3(k).anion=[Data(m).Ch3_ToA];
        Ch3(k).laser = [Data(n).Ch3_ToA];
    end

allValues1=uint32([Ch3.laser]);
[Y1,X1]=groupcounts(allValues1.');
ind=X1>lowlim & X1<highlim;
n1=sum(Y1(ind))

allValues2=uint32([Ch3.anion]);
[Y2,X2]=groupcounts(allValues2.');
ind=X2>lowlim & X2<highlim;
n2=sum(Y2(ind))
 count_laser_n=n1
count_anion_m=n2

else
```

```
        Ch3(M/2) = struct('laser',[], 'anion',[]);
        for k=1:M/2
            m=2*k-1 ; n=2*k;
            Ch3(k).laser=[Data(m).Ch3_ToA];
            Ch3(k).anion = [Data(n).Ch3_ToA];
        end
    allValues1=uint32([Ch3.laser]);
   [Y1,X1]=groupcounts(allValues1.');
   ind=X1>lowlim & X1<highlim;
   n1=sum(Y1(ind))

    allValues2=uint32([Ch3.anion]);
   [Y2,X2]=groupcounts(allValues2.');
   ind=X2>lowlim & X2<highlim;
   n2=sum(Y2(ind))
   count_laser_m=n1
   count_anion_n=n2
   end
   llim=lowlim*5e-4;
   hlim=highlim*5e-4;
figure(1)
X1 =double(allValues2)*5e-4;
edges = [20 :0.005: 26];
h=histogram(X1,edges);
%histfit(X,edges)
```

```
 xlim([20, 26]);
 ylim([0, 50]);
 ax = gca;
ax.FontSize = 20;
ax.LineWidth=1;
%ax.YTickLabel=[];
pbaspect([1 1 1])
xlabel('ToF-/-\mus','fontsize',16)
ylabel('Counts','fontsize',16)
figure(2)
X2 =double(allValues1)*5e-4;
edges = [20 :0.005: 26];
h=histogram(X2,edges);
%histfit(X,edges)
xlim([20, 26]);
ylim([0, 50]);
ax = gca;
ax.FontSize = 20;
ax.LineWidth=1;
%ax.YTickLabel=[];
pbaspect([1 1 1])
xlabel('ToF-/-\mus','fontsize',16)
ylabel('Counts','fontsize',16)
figure(3)
%X =double(allValues2)*5e-4;
```

```
edges = [20 :0.005: 26];
h=histogram(X1,edges);
%histfit(X,edges)
xlim([20, 24.1]);
ylim([0, 50]);
ax = gca;
ax.FontSize = 20;
ax.LineWidth=1;
%ax.YTickLabel=[];
pbaspect([1 1 1])
xlabel('ToF-/-\mus','fontsize',16)
ylabel('Counts','fontsize',16)
ind1 = X1 > 20 & X1 < 26;
test_laser_off_746_ch3=X1(ind1);
save("test_neutral_loff_746_ch3.mat",
"test_laser_off_746_ch3")
ind1 = X2 > 20 & X2 < 26;
test_laser_on_746_ch3=X2(ind1);
save("test_neutral_lon_746_ch3.mat",
    "test_laser_on_746_ch3")
```

The code bkg_sub_sd.m is used to subtract the laser off and laser background data from laser on data.

```
clearvars
clc
close all
```

```
load('~\83\test_laser_on_83.mat');
whos ("-file", "test_laser_on_83.mat");
load('~\83\test_laser_off_83.mat');
whos ("-file", "test_laser_off_83.mat");
load('~\83\test_83_laser_bkg.mat');
whos ("-file", "test_83_laser_bkg.mat");
%step=0.0050
step=0.010; %for the paper and thesis
edges = [20 :step: 26];
x_range=20 :step: 26;
%edges = [20 :0.05: 25];
figure(1)
%h=histogram(test_laser_on_616,edges);f
h=histogram(test_laser_on_83,edges);
x=h.Values;
xlim([20, 26]);
%xlim([22, 26]);
ylim([0, 4000]);
ax = gca;
ax.FontSize = 20;
ax.LineWidth=1;
%ax.YTickLabel=[];
pbaspect([1 1 1])
xlabel('ToF-/-\mus','fontsize',16)
ylabel('Counts','fontsize',16)
```

```
ind1 = test_laser_on_83 > 20 & test_laser_on_83 < 21.5;
count_lon_83=sum(ind1)
% ind_par = test_laser_on_83 > 24.3 & test_laser_on_83 < 24.6;
% count_lon_83_par=sum(ind_par)
sum_x=sum(x)

figure(2)
% h1=histogram(test_laser_off_616,edges);
h1=histogram(test_laser_off_83,edges);
binEdges = h1.BinEdges
x_range1 = binEdges(1:end-1) + h1.BinWidth/2
y=h1.Values;
xlim([20, 26]);
%xlim([22, 26]);
ylim([0, 4000]);
ax = gca;
ax.FontSize = 20;
ax.LineWidth=1;
%ax.YTickLabel=[];
pbaspect([1 1 1])
xlabel('ToF-/-\mus','fontsize',16)
ylabel('Counts','fontsize',16)
% ind_par_1 = test_laser_off_83 > 24.3
    & test_laser_off_83 < 24.6;
% count_lon_83_par1=sum(ind_par_1)
```

```
figure(3)
% h2=histogram(test_836_laser_bkg -0.07,edges);
h2=histogram(test_83_laser_bkg ,edges);
z1=h2.Values;
% z=z1*01.2;


xlim([20, 26]);
%xlim([22, 26]);
ylim([0, 400]);
ax = gca;
ax.FontSize = 20;
ax.LineWidth=1;
%ax.YTickLabel=[];
pbaspect([1 1 1])
xlabel('ToF-/-\mus','fontsize',16)
ylabel('Counts','fontsize',16)
ind1 = test_83_laser_bkg > 20 & test_83_laser_bkg < 21.5;
count_lbkg_83=sum(ind1)
count_rat=count_lon_83/count_lbkg_83
z_norm=z1*count_rat
figure(4)
sub=x-y-z_norm
%x_range=20 :0.05: 24.1
```

```
length(x_range);
length(sub);
%plot(x_range(1:end-1),sub);
plot(x_range1,sub)
hold on
% plot(x_range1,x)
% hold off
xlim([20, 24.2]);
%xlim([22, 26]);
ylim([-10, 400]);
yline(0, '--r');
ax = gca;
ax.FontSize = 20;
ax.LineWidth=1;
%ax.YTickLabel=[];
pbaspect([1 1 1])
xlabel('ToF-/-\mus','fontsize',16)
ylabel('Counts','fontsize',16)

%ind1 = x_range > 21.7 & x_range < 22.1;
ind1 = x_range > 21.8 & x_range < 22.085;
sub(ind1);
n_CF3 = sum(sub(ind1))

S_CF3_lon = sum(x(ind1))
```

```
S_CF3_loff = sum(y(ind1))
S_CF3_bkg = sum(z_norm(ind1))
err_CF3=sqrt(S_CF3_lon+S_CF3_loff+S_CF3_bkg)
%ind2 = x_range > 22.30 & x_range < 22.75;
ind2 = x_range > 22.4 & x_range < 22.76;
sub(ind2)
n_I = sum(sub(ind2))
S_I_lon = sum(x(ind2))
S_I_loff = sum(y(ind2))
S_I_bkg = sum(z_norm(ind2))
err_I=sqrt(S_I_lon+S_I_loff+S_I_bkg)
ind3 = x_range >= 23.0 & x_range <= 23.165;
sub(ind3)
n_CF2I = sum(sub(ind3))
S_CF2I_lon = sum(x(ind3))
S_CF2I_loff = sum(y(ind3))
S_CF2I_bkg = sum(z_norm(ind3))
err_CF2I=sqrt(S_CF2I_lon+S_CF2I_loff+S_CF2I_bkg)
ind4 = x_range > 23.3 & x_range < 23.55;
sub(ind4);
n_CF3I = sum(sub(ind4))
S_CF3I_lon = sum(x(ind4))
S_CF3I_loff = sum(y(ind4))
S_CF3I_bkg = sum(z_norm(ind4))
err_CF3I=sqrt(S_CF3I_lon+S_CF3I_loff+S_CF3I_bkg)
```

```
ind5 = x_range >= 23.785 & x_range  <= 23.935  %
sub(ind5)
n_I2 = sum(sub(ind5))
S_I2_lon = sum(x(ind5))
S_I2_loff = sum(y(ind5))
S_I2_bkg = sum(z_norm(ind5))
err_I2=sqrt(S_I2_lon+S_I2_loff+S_I2_bkg)
count_frag=[n_CF3, n_I, n_CF2I, n_CF3I, n_I2];
E=array2table(count_frag, 'VariableNames',
{'n_CF3', 'n_I' ,'n_CF2I', 'n_CF3I', 'n_I2'})
err_frag=[err_CF3, err_I ,err_CF2I, err_CF3I, err_I2]
E1=array2table(err_frag, 'VariableNames',
    {'err_CF3', 'err_I' ,'err_CF2I', 'err_CF3I', 'err_I2'})
tof_83=sub
%save("tof_power_new_TOFrange","x_range1","tof_83")%,"-append")
%save("tof_power_new_TOFrange","tof_83","-append")
%writetable(array2table(count_frag, 'VariableNames',
    {'n_CF3', 'n_I' ,'n_CF2I', 'n_CF3I', 'n_I2'}),
    'frag_data_83_subra83tio_bin_83ns_newTOF.txt')
%writetable(array2table(err_frag, 'VariableNames',
    {'err_CF3', 'err_I' ,'err_CF2I', 'err_CF3I', 'err_I2'})
    'err_data_83_subratio_bin_83ns_newTOF.txt')
```

Appendix C

Matlab code for fitting the experimental angular distribution data.

Main code for fitting the angular distribution.

```
clc
clear all
load('G:\Data\AngDistFit\CH3COOH.mat');
whos("-file","CH3COOH.mat")
raw_c=CH3COOH9p1Vadist ;
ratio=raw_c/sum(raw_c);
counts=raw_c/sum(raw_c);
w=1./(sqrt(raw_c)/sum(raw_c)).^2;
[coeffs,chi]=ang_dist_psfit(counts,theta,1000,1,40);
c=coeffs
chi
[coeffs,chi]=sp_psfit(counts,theta,1000,1,40);
c1=coeffs
[coeffs,chi]=sp_psfit(counts,theta,1000,1,40);
c2=coeffs
```

```
figure(1)
errorbar(theta,raw_c/sum(raw_c),sqrt(raw_c)/sum(raw_c),'o',
    'LineWidth',2, 'MarkerSize', 5)%,'MarkerFaceColor',
    'blue','MarkerEdgeColor','blue')
ax = gca;
ax.FontSize = 20;
ax.LineWidth=1;
xlim([0, 180]);
%ylim([0.5, 1.01]);
%ylim([0.014, 0.03]);
%ax.YTickLabel=[];
pbaspect([1 1 1])
xlabel('Dissociation theta (deg)','fontsize',16)
ylabel('H^- ion yield (arb. unit)','fontsize',16)

modelfun=@(c, theta) c(1)^2+c(2)^2*cosd(theta).^2
    +c(3)^2*sind(theta).^2 ...
+c(4)^2*(3*cosd(theta).^2 -1) ...
+c(5)^2*sind(theta).^2.*cosd(theta).^2
    +c(6)^2*sind(theta).^4 ...
+2*c(1)*c(2)*sin(c(7)-c(8)).*cosd(theta) ...
+2*c(1)*c(4)*sin(c(7)-c(9)).*(3*cosd(theta).^2 -1) ...
+2*c(2)*c(4)*sin(c(8)-c(9)).
    *cosd(theta).*(3*cosd(theta).^2 -1) ...
```

```
+2*c(3)*c(5)*sin(c(8)-c(9)).
    *cosd(theta).*sind(theta).^2;
%A' to A' transition,s+p+d partial waves
start=c
nlm=fitnlm(theta,ratio,modelfun,start,'Weight',w)
xx = linspace(0,180,180)';
I_counts_nlm=predict(nlm,xx)
line(xx,predict(nlm,xx),'linestyle','--',
    'color','b','LineWidth',1.5)
I_counts_sp=c1(1)^2+c1(2)^2*cosd(xx).^2
    +c1(3)^2*sind(xx).^2
    +2*c1(1)*c1(2)*sind(c1(4)-c1(5))*cosd(xx)
        ;%A' to A' transition,%s+P
I_counts_spd=c(1)^2+c(2)^2*cosd(xx).^2
    +c(3)^2*sind(xx).^2 ...
+c(4)^2*(3*cosd(xx).^2 -1) ...
+c(5)^2*sind(xx).^2.*cosd(xx).^2+c(6)^2*sind(xx).^4 ...
+2*c(1)*c(2)*sin(c(7)-c(8)).*cosd(xx) ...
+2*c(1)*c(4)*sin(c(7)-c(9)).*(3*cosd(xx).^2 -1) ...
+2*c(2)*c(4)*sin(c(8)-c(9)).*cosd(xx).*(3*cosd(xx).^2 -1) ...
+2*c(3)*c(5)*sin(c(8)-c(9)).*cosd(xx).*sind(xx).^2;
%A' to A' transition,s+p+d partial waves
I_counts_pd=c2(1)^2*sind(xx).^2
    +c2(2)^2*sind(xx).^2.*cosd(xx).^2 ...
+c2(3)^2*sind(xx).^4 ...
```

```
+2*c2(1)*c2(2)*sin(c2(4)-c2(5)).*cosd(xx).*sind(xx).^2;
%A' to A" transition,p+d partial waves
figure(2)
errorbar(theta,raw_c/sum(raw_c),sqrt(raw_c)/sum(raw_c),
    'o', 'color','b','LineWidth',1.5, 'MarkerSize', 5)
hold on
plot(xx,I_counts_spd,'r','LineWidth',1.5)
plot(xx,I_counts_sp,'color',[0.4940 0.1840 0.5560],
    'LineWidth',1.5)
plot(xx,I_counts_pd,'k','LineWidth',1.5)
plot(xx,I_counts_nlm,'linestyle','—','color','g',
    'LineWidth',1.5)
%line(xx,predict(nlm,xx),'linestyle','--','color',
    'g','LineWidth',1.5)
ax = gca;
ax.FontSize = 20;
ax.LineWidth=1;
xlim([0, 180]);
%ylim([0.0, 1.01]);
%ylim([0.014, 0.03]);
%ax.YTickLabel=[];
pbaspect([1 1 1])
%legend('D^-','spd','sp','pd','FontSize',10,
    'Location','northwest','Box', 'off')
legend('H^-','spd','sp','pd','spd-nlmfit',
```

```
    'FontSize',10,'Location','northwest',
    'Box', 'off')%,'Orientation','horizontal')
xlabel('Dissociation angle (deg)','fontsize',16)
ylabel('H^ ion yield (arb. unit)','fontsize',16)

theta_fit=xx
c_H_CH3COOD9p1VadistL_spd=I_counts_spd;
c_H_CH3COOD9p1VadistL_sp=I_counts_sp;
c_H_CH3COOD9p1VadistL_pd=I_counts_pd;
c_H_CH3COOD9p1VadistL_nlm=I_counts_nlm;
%save("H_CH3COOD9p1VadistH_fit","c_H_CH3COOD9p1VadistL_spd",
"c_H_CH3COOD9p1VadistL_sp","c_H_CH3COOD9p1VadistL_pd",
"c_H_CH3COOD9p1VadistL_nlm","-append")
```

This function is called by the above fitting code.

```
function [coeffs,chi]=
    ang_dist_psfit(counts,angle,nSwarm,s_start,s_end)
rng('shuffle')
% A' to A' transition, for s+p
% lb=[ -1     -1   -1    -2   -2   ];
% change the bound based on your requirement.
%the number of elecment is the number of parameter
% ub=[ 2   2  2   10   12  ];

%A' to A' transition,s+p+d partial waves
lb=[ 0      0   0     0   0   0   0     0   0     ];
```

```
ub=[ 2    2   2    2    2   2   10    25    12];

 %A' to A" transition,p+d partial waves
% lb=[ 0    0   0     0    -5     ];
% ub=[ 5    5    20    20    20];

opts=optimoptions('particleswarm','Swarmsize',nSwarm,...
'FunctionTolerance',1E-4,'MaxIterations',nSwarm*2,
'MaxStallIterations',round(nSwarm/5),...
'Useparallel',false,'Display','iter');

[coeffs]=particleswarm(@findCorrPar,numel(lb),lb,ub,opts);
function obj=findCorrPar(c)
%the program will minimize the value of obj

%A' to A' transition,%s+P
%I_counts=c(1)^2+c(2)^2*cosd(angle).^2
     +c(3)^2*sind(angle).^2
%+2*c(1)*c(2)*sind(c(4)-c(5))*cosd(angle);

%A' to A' transition,s+p+d partial waves
I_counts=c(1)^2+c(2)^2*cosd(angle).^2
     +c(3)^2*sind(angle).^2  ...
+c(4)^2*(3*cosd(angle).^2  -1)  ...
+c(5)^2*sind(angle).^2.*cosd(angle).^2
```

```
      +c(6)^2*sind(angle).^4  ...
+2*c(1)*c(2)*sin(c(7)-c(8)).*cosd(angle)  ...
+2*c(1)*c(4)*sin(c(7)-c(9)).*(3*cosd(angle).^2  -1)  ...
+2*c(2)*c(4)*sin(c(8)-c(9)).*cosd(angle).
      *(3*cosd(angle).^2  -1)  ...
+2*c(3)*c(5)*sin(c(8)-c(9)).*cosd(angle).*sind(angle).^2;

%A' to A" transition,p+d partial waves
%  I_counts=c(1)^2*sind(angle).^2
      %+c(2)^2*sind(angle).^2.*cosd(angle).^2  ...
%     +c(3)^2*sind(angle).^4  ...
%     +2*c(1)*c(2)*sin(c(4)-c(5)).
      *cosd(angle).*sind(angle).^2;
obj=1/(numel(s_start:s_end)-numel(lb))
      *sum((counts(s_start:s_end)
      -I_counts(s_start:s_end)).^2,"omitnan");
      end
 c=coeffs;

%A' to A' transition, s+p
%I_counts = c(1)^2+c(2)^2*cosd(angle).^2
      +c(3)^2*sind(angle).^2
      +2*c(1)*c(2)*sind(c(4)-c(5))*cosd(angle);

 %A' to A' transition,s+p+d partial waves
```

```
I_counts=c(1)^2+c(2)^2*cosd(angle).^2+
c(3)^2*sind(angle).^2  ...
+c(4)^2*(3*cosd(angle).^2  -1)  ...
+c(5)^2*sind(angle).^2.*cosd(angle).^2+
c(6)^2*sind(angle).^4  ...
+2*c(1)*c(2)*sin(c(7)-c(8)).*cosd(angle)  ...
+2*c(1)*c(4)*sin(c(7)-c(9)).*(3*cosd(angle).^2  -1)  ...
+2*c(2)*c(4)*sin(c(8)-c(9)).
*cosd(angle).*(3*cosd(angle).^2  -1)  ...
+2*c(3)*c(5)*sin(c(8)-c(9)).*cosd(angle).*sind(angle).^2;

%%A' to A" transition,p+d partial waves
% I_counts=c(1)^2*sind(angle).^2
     +c(2)^2*sind(angle).^2.*cosd(angle).^2  ...
% +c(3)^2*sind(angle).^4  ...
% +2*c(1)*c(2)*sin(c(4)-c(5)).*cosd(angle).*sind(angle).^2;

chi=1/(numel(s_start:s_end)-numel(lb))
     *sum((counts(s_start:s_end)
     -I_counts(s_start:s_end)).^2,"omitnan");
figure()
plot(angle,counts,'b^')
hold on
plot(angle,I_counts,'r')
end
```

Bibliography

[1] Eugen Illenberger and Jacques Momigny. *Gaseous molecular ions: an introduction to elementary processes induced by ionization*, volume 2. Springer Science & Business Media, 1992.

[2] H Adaniya, DS Slaughter, T Osipov, and A Belkacem. A momentum imaging microscope for dissociative electron attachment. *Review of Scientific Instruments*, 83(2), 2012.

[3] DS Slaughter, Th Weber, A Belkacem, CS Trevisan, RR Lucchese, CW McCurdy, and TN Rescigno. Selective bond-breaking in formic acid by dissociative electron attachment. *Physical Chemistry Chemical Physics*, 22(25):13893–13902, 2020.

[4] R.Wellington Davis, A.G. Robiette, M.C.L. Gerry, E. Bjarnov, and G. Winnewisser. Microwave spectra and centrifugal distortion constants of formic acid containing 13c and 18o: Refinement of the harmonic force field and the molecular structure. *Journal of Molecular Spectroscopy*, 81(1):93–109, 1980.

[5] Arvi Rauk, Dake Yu, and David A Armstrong. Carboxyl free radicals: formyloxyl (hcoo. bul.) and acetyloxyl (ch3coo. bul.) revisited. *Journal of the American Chemical Society*, 116(18):8222–8228, 1994.

[6] Sydney Leach, Martin Schwell, Sun Un, Hans Werner Jochims, and Helmut Baumgärtel. VUV absorption spectrum of acetic acid between 6 and 20 eV. *Chemical Physics*, 321(1-2):159–170, 1 2006.

[7] Ana I Lozano, Lidia Álvarez, Adrián García-Abenza, Carlos Guerra, Fábris Kossoski, Jaime Rosado, Francisco Blanco, Juan Carlos Oller, Mahmudul Hasan, Martin Centurion, et al. Electron scattering from 1-methyl-5-nitroimidazole: Cross-sections for modeling electron transport through potential radiosensitizers. *International Journal of Molecular Sciences*, 24(15):12182, 2023.

[8] John Robert Taylor and William Thompson. *An introduction to error analysis: the study of uncertainties in physical measurements*, volume 2. Springer, 1982.

[9] MS Windows NT kernel description. `https://webbook.nist.gov/chemistry/`. Accessed: 2024-03-05.

[10] John L Holmes, Fred P Lossing, and Paul M Mayer. Heats of formation of oxygen-containing organic free radicals from appearance energy measurements. *Journal of the American Chemical Society*, 113(26):9723–9728, 1991.

[11] Vaibhav S Prabhudesai, N Bhargava Ram, G Aravind, P Rawat, and E Krishnakumar. Probing site selective fragmentation of molecules containing hydroxyl group using velocity slice imaging. In *Journal of Physics: Conference Series*, volume 80, page 012016. IOP Publishing, 2007.

[12] M W Chase. The journal of physical and chemical reference data. 2008.

[13] R Yamdagni and P Kebarle. Intrinsic acidities of carboxylic acids from gas-phase acid equilibriums. *Journal of the American Chemical Society*, 95(12):4050–4052, 1973.

[14] John Rumble et al. Crc handbook of chemistry and physics. 2017.

[15] H Hotop, M-W Ruf, Michael Allan, and II Fabrikant. Resonance and threshold phenomena in low-energy electron collisions with molecules and clusters. In *Advances in atomic, molecular, and optical physics*, volume 49, pages 85–216. Elsevier, 2003.

[16] Loucas Georgiou Christophorou. *Electron—Molecule Interactions and Their Applications: Volume 2*, volume 2. Academic Press, 2013.

[17] Tatiana Oster, Oddur Ingolfsson, Martina Meinke, Thomas Jaffke, and Eugen Illenberger. Anion formation from gaseous and condensed cf3i on low energy electron impact. *The Journal of chemical physics*, 99(7):5141–5150, 1993.

[18] Martin Heni and Eugen Illenberger. Dissociative electron attachment to cf3i: an example of a completely unbalanced excess energy distribution. *Chemical physics letters*, 131(4-5):314–318, 1986.

[19] Vaibhav S. Prabhudesai, Aditya H. Kelkar, Dhananjay Nandi, and E. Krishnakumar. Functional group dependent site specific fragmentation of molecules by low energy electrons. *Phys. Rev. Lett.*, 95:143202, Sep 2005.

[20] DM Cyr, GA Bishea, MG Scarton, and MA Johnson. Observation of charge-transfer excited states in the i- ch3i, i- ch3br, and i- ch2br2sn2 reaction intermediates using photofragmentation and photoelectron spectroscopies. *The Journal of chemical physics*, 97(8):5911–5914, 1992.

[21] Alice Kunin and Daniel M Neumark. Time-resolved radiation chemistry: femtosecond photoelectron spectroscopy of electron attachment and photodissociation dynamics in iodide–nucleobase clusters. *Physical Chemistry Chemical Physics*, 21(14):7239–7255, 2019.

[22] J Cooper and Richard N Zare. Angular distribution of photoelectrons. *The Journal of chemical physics*, 48(2):942–943, 1968.

[23] Eric Surber and Andrei Sanov. Photoelectron imaging spectroscopy of molecular and cluster anions: Cs2- and ocs-(h2o) 1, 2. *The Journal of chemical physics*, 116(14):5921–5924, 2002.

[24] Jonathan G Underwood and Katharine L Reid. Time-resolved photoelectron angular distributions as a probe of intramolecular dynamics: Connecting the molecular frame and the laboratory frame. *The Journal of Chemical Physics*, 113(3):1067–1074, 2000.

[25] Tamar Seideman. Time-resolved photoelectron angular distributions: concepts, applications, and directions. *Annual review of physical chemistry*, 53(1):41–65, 2002.

[26] Alison V Davis, Roland Wester, Arthur E Bragg, and Daniel M Neumark. Time-resolved photoelectron imaging of the photodissociation of i2-. *The Journal of chemical physics*, 118(3):999–1002, 2003.

[27] David J Leahy, Katharine L Reid, and Richard N Zare. Determination of molecular symmetry axis (z) orientation via photoelectron angular distribution measurements. *The Journal of Physical Chemistry*, 95(21):8154–8158, 1991.

[28] Katharine L Reid and Jonathan G Underwood. Extracting molecular axis alignment from photoelectron angular distributions. *The Journal of Chemical Physics*, 112(8):3643–3649, 2000.

[29] Jae Kyu Song, Masaaki Tsubouchi, and Toshinori Suzuki. Femtosecond photoelectron imaging on pyrazine: Spectroscopy of 3s and 3p rydberg states. *The Journal of Chemical Physics*, 115(19):8810–8818, 2001.

[30] Masaaki Tsubouchi, Benjamin J Whitaker, Li Wang, Hiroshi Kohguchi, and Toshinori Suzuki. Photoelectron imaging on time-dependent molecular alignment created by a femtosecond laser pulse. *Physical Review Letters*, 86(20):4500, 2001.

[31] Arthur E Bragg, Roland Wester, Alison V Davis, Aster Kammrath, and Daniel M Neumark. Excited-state detachment dynamics and rotational coherences of c2- via time-resolved photoelectron imaging. *Chemical physics letters*, 376(5-6):767–775, 2003.

[32] Edward Condon. A theory of intensity distribution in band systems. *Physical Review*, 28(6):1182, 1926.

[33] James Franck and EG Dymond. Elementary processes of photochemical reactions. *Transactions of the Faraday Society*, 21(February):536–542, 1926.

[34] GJ Schulz and RK Asundi. Isotope effect in the dissociative attachment in h 2 at low energy. *Physical Review*, 158(1):25, 1967.

[35] Olivier May, Juraj Fedor, and Michael Allan. Isotope effect in dissociative electron attachment to acetylene. *Physical Review A*, 80(1):012706, 2009.

[36] George J Schulz. Resonances in electron impact on diatomic molecules. *Reviews of Modern Physics*, 45(3):423, 1973.

[37] Jack Simons. Molecular anions. *The Journal of Physical Chemistry A*, 112(29):6401–6511, 2008.

[38] Jack Simons. Molecular anions perspective. *The Journal of Physical Chemistry A*, 127(18):3940–3957, 2023.

[39] Margaret A Yandell, Sarah B King, and Daniel M Neumark. Decay dynamics of nascent acetonitrile and nitromethane dipole-bound anions produced by intracluster charge-transfer. *The Journal of Chemical Physics*, 140(18), 2014.

[40] Golda Mensa-Bonsu, David J Tozer, and Jan RR Verlet. Photoelectron spectroscopic study of i-· icf 3: a frontside attack sn 2 pre-reaction complex. *Physical Chemistry Chemical Physics*, 21(26):13977–13985, 2019.

[41] J Gadhi, G Wlodarczak, J Legrand, and J Demaison. The dipole moments of methyl bromide and methyl iodide. *Chemical physics letters*, 156(4):401–404, 1989.

[42] Gennady L Gutsev, Andrzej L Sobolewski, and Ludwik Adamowicz. A theoretical study on the structure of acetonitrile (ch3cn) and its anion ch3cn-. *Chemical physics*, 196(1-2):1–11, 1995.

[43] A Peter Cox, Geoffrey Duxbury, Judith A Hardy, and Yoshiyuki Kawashima. Microwave spectra of cf 3 br and cf 3 i. structures and dipole moments. *Journal of the Chemical Society, Faraday Transactions 2: Molecular and Chemical Physics*, 76:339–350, 1980.

[44] Don W Arnold, Stephen E Bradforth, Eun H Kim, and Daniel M Neumark. Study of i-(co2) n, br-(co2) n, and i-(n2o) n clusters by anion photoelectron spectroscopy. *The Journal of chemical physics*, 102(9):3510–3518, 1995.

[45] Joshua P Rogers, Cate S Anstöter, and Jan RR Verlet. Ultrafast dynamics of low-energy electron attachment via a non-valence correlation-bound state. *Nature Chemistry*, 10(3):341–346, 2018.

[46] Michael L Alexander, Nancy E Levinger, MA Johnson, Douglas Ray, and WC Lineberger. Recombination of br- 2 photodissociated within mass selected ionic clusters. *The Journal of chemical physics*, 88(10):6200–6210, 1988.

[47] John M Papanikolas, Vasil Vorsa, María E Nadal, Paul J Campagnola, Heinrich K Buchenau, and WC Lineberger. I- 2 photodissociation and recombination dynamics in size-selected i- 2 (co2) n cluster ions. *The Journal of chemical physics*, 99(11):8733–8750, 1993.

[48] John M Papanikolas, James R Gord, Nancy E Levinger, Douglas Ray, Vasil Vorsa, and WC Lineberger. Photodissociation and geminate recombination dynamics of i2-in mass-selected i2-(co2) n cluster ions. *The Journal of Physical Chemistry*, 95(21):8028–8040, 2002.

[49] Edward Matthews, Rosaria Cercola, Golda Mensa-Bonsu, Daniel M Neumark, and Caroline EH Dessent. Photoexcitation of iodide ion-pyrimidine clusters above the electron detachment threshold: Intracluster electron transfer versus nucleobase-centred excitations. *The Journal of Chemical Physics*, 148(8), 2018.

[50] Rosaria Cercola, Edward Matthews, and Caroline EH Dessent. Near-threshold electron transfer in anion-nucleobase clusters: does the identity of the anion matter? *Molecular Physics*, 117(21):3001–3010, 2019.

[51] K Nagesha, VR Marathe, and E Krishnakumar. Negative ion formation from ch3i by electron impact. *International journal of mass spectrometry and ion processes*, 145(1-2):89–96, 1995.

[52] M Braun, Ilya I Fabrikant, MW Ruf, and H Hotop. Low-energy electron collisions with ch3br: the dependence of elastic scattering, vibrational excitation, and dissociative attachment on the initial vibrational energy. *Journal of Physics B: Atomic, Molecular and Optical Physics*, 40(4):659, 2007.

[53] A Schramm, MW Ruf, M Stano, S Matejcik, II Fabrikant, and H Hotop. High-resolution study of dissociative electron attachment to dipolar molecules at low energies: Ch2br2 and ccl3br. *Journal of Physics B: Atomic, Molecular and Optical Physics*, 35(20):4179, 2002.

[54] See Leang Chin. *Multiphoton Ionization of Atoms*. Elsevier, 2012.

[55] A Sharma, MN Slipchenko, MN Shneider, X Wang, KA Rahman, and Alexey Shashurin. Counting the electrons in a multiphoton ionization by elastic scattering of microwaves. *Scientific reports*, 8(1):2874, 2018.

[56] K Yu Vagin and SA Uryupin. Collective modes of plasma formed by multiphoton ionization of rarefied gas. *Plasma Sources Science and Technology*, 29(3):035005, 2020.

[57] Animesh Sharma, Erik L Braun, Adam R Patel, K Arafat Rahman, Mikhail N Slipchenko, Mikhail N Shneider, and Alexey Shashurin. Diagnostics of co concentration in gaseous mixtures at elevated pressures by resonance enhanced multi-photon ionization and microwave scattering. *Journal of Applied Physics*, 128(14), 2020.

[58] U Boesl, R Zimmermann, C Weickhardt, D Lenoir, KW Schramm, A Kettrup, and EW Schlag. Resonance-enhanced multi-photon ionization: a species-selective ion source for analytical time-of-flight mass spectroscopy. *Chemosphere*, 29(7):1429–1440, 1994.

[59] Ulrich Boesl and Aras Kartouzian. Mass-selective chiral analysis. *Annual Review of Analytical Chemistry*, 9(1):343–364, 2016.

[60] VD Zvorykin, AV Shutov, and NN Ustinovskii. Review of nonlinear effects under tw-power ps pulses amplification in garpun-mtw ti: sapphire-krf laser facility. *Matter and Radiation at Extremes*, 5(4), 2020.

[61] AV Shutov, NN Ustinovskii, IV Smetanin, DV Mokrousova, SA Goncharov, SV Ryabchuk, ES Sunchugasheva, LV Seleznev, AA Ionin, and VD Zvorykin. Major pathway for multiphoton air ionization at 248 nm laser wavelength. *Applied Physics Letters*, 111(22), 2017.

[62] AK Dharmadhikari, JA Dharmadhikari, and D Mathur. Visualization of focusing–refocusing cycles during filamentation in baf 2. *Applied Physics B*, 94:259–263, 2009.

[63] IV Smetanin, AO Levchenko, AV Shutov, NN Ustinovskii, and VD Zvorykin. Role of coherent resonant nonlinear processes in the ultrashort krf laser pulse propagation and filamentation in air. *Nuclear Instruments and Methods in Physics Research Section B: Beam Interactions with Materials and Atoms*, 369:87–91, 2016.

[64] M Plummer and CJ Noble. Resonant enhancement of harmonic generation in argon at 248 nm. *Journal of Physics B: Atomic, Molecular and Optical Physics*, 35(2):L51, 2002.

[65] P Ackermann, H Münch, and T Halfmann. Resonantly-enhanced harmonic generation in argon. *Optics Express*, 20(13):13824–13832, 2012.

[66] IA Ivanov and AS Kheifets. Resonant enhancement of generation of harmonics. *Physical Review A*, 78(5):053406, 2008.

[67] A McPherson, G Gibson, H Jara, U Johann, Ting S Luk, IA McIntyre, Keith Boyer, and Charles K Rhodes. Studies of multiphoton production of vacuum-ultraviolet radiation in the rare gases. *JOSA B*, 4(4):595–601, 1987.

[68] Katsumi Kimura. Development of laser photoelectron spectroscopy based on resonantly enhanced multiphoton ionization. *Journal of electron spectroscopy and related phenomena*, 100(1-3):273–296, 1999.

[69] Philip J Silva, Richard A Carlin, and Kimberly A Prather. Single particle analysis of suspended soil dust from southern california. *Atmospheric Environment*, 34(11):1811–1820, 2000.

[70] ML Huertas and J Fontan. Formation of stable positive and negative small ions of tropospheric interest. *Atmospheric Environment (1967)*, 16(10):2521–2527, 1982.

[71] Kawaguchi Kentarou, Ryuji Fujimori, Sayaka Aimi, Shuro Takano, Emi Y Okabayashi, Harshal Gupta, Sandra BrÜnken, Carl A Gottlieb, Michael C McCarthy, and Patrick Thaddeus. Observation of ch toward irc+ 10216. *Publications of the Astronomical Society of Japan*, 59(5):L47–L50, 2007.

[72] Marcelino Agúndez, José Cernicharo, Michel Guélin, Maryvonne Gerin, MC McCarthy, and P Thaddeus. Search for anions in molecular sources: C4h-detection in l1527. *Astronomy & Astrophysics*, 478(1):L19–L22, 2008.

[73] José Cernicharo, Michel Guélin, Marcelino Agúndez, MC McCarthy, and P Thaddeus. Detection of c5n- and vibrationally excited c6h in irc+ 10216. *The Astrophysical Journal*, 688(2):L83, 2008.

[74] JL Hall, EJ Robinson, and LM Branscomb. Laser double-quantum photodetachment of i-. *Physical Review Letters*, 14(25):1013, 1965.

[75] C Blondel, M Crance, C Delsart, and A Giraud. Angular distributions in multiphoton detachment of negative halogens. *Journal de Physique II*, 2(4):839–852, 1992.

[76] Christophe Blondel, Michèle Crance, Christian Delsart, and Antoine Giraud. Excess-photon absorption in a negative ion. *Journal of Physics B: Atomic, Molecular and Optical Physics*, 24(16):3575, 1991.

[77] H Stapelfeldt, Peter Balling, C Brink, and HK Haugen. Excess-photon detachment in the negative gold ion. *Physical review letters*, 67(13):1731, 1991.

[78] MD Davidson, HG Muller, and HB van Linden van den Heuvell. Experimental observation of excess-photon detachment of negative ions. *Physical review letters*, 67(13):1712, 1991.

[79] Robert N Rosenfeld, Joseph M Jasinski, and John I Brauman. Infrared multiphoton electron detachment from the benzyl anion. *The Journal of Chemical Physics*, 71(2):1030–1031, 1979.

[80] Kenneth J Reed, Albert H Zimmerman, Hans C Andersen, and John I Brauman. Cross sections for photodetachment of electrons from negative ions near threshold. *The Journal of Chemical Physics*, 64(4):1368–1375, 1976.

[81] Jennifer E Mann, Sarah E Waller, David W Rothgeb, and Caroline Chick Jarrold. Resonant two-photon detachment of wo2-. *Chemical Physics Letters*, 506(1-3):31–36, 2011.

[82] Mark A Johnson and WC Lineberger. Pulsed methods for cluster ion spectroscopy, 1988.

[83] Lynmarie A Posey, Michael J Deluca, and Mark A Johnson. Demonstration of a pulsed photoelectron spectrometer on mass-selected negative ions: O-, o2-, and o4-. *Chemical physics letters*, 131(3):170–174, 1986.

[84] Xiaojun Wang, Mahmudul Hasan, Lin Fan, Yibo Wang, Hui Li, Daniel S Slaughter, and Martin Centurion. Mass-selected ion–molecule cluster beam apparatus for ultrafast photofragmentation studies. *Review of Scientific Instruments*, 94(9), 2023.

[85] Xiaojun Wang. Mass-selected ion-molecule cluster beam apparatus for ultrafast photofragmentation studies (micbaups). 2023.

[86] JR Pierce. Rectilinear electron flow in beams. *Journal of applied physics*, 11(8):548–554, 1940.

[87] Uzi Even. The even-lavie valve as a source for high intensity supersonic beam. *EPJ Techniques and Instrumentation*, 2(1):17, 2015.

[88] WC Wiley and Ii H McLaren. Time-of-flight mass spectrometer with improved resolution. *Review of scientific instruments*, 26(12):1150–1157, 1955.

[89] Wade L Fite. Expansion of gases from molecular beam sources. In *Research Note No. 1*. Extranuclear Laboratories Inc. Pittsburgh, Pa., 1971.

[90] Giacinto Scoles. Atomic and molecular beam methods. *(No Title)*, 1988.

[91] John Eilef Mathis. *High resolution multi-and single photon electron spectroscopy using hemispherical electron spectrometer with positive-sensitive detection*. The University of Tennessee, 1995.

[92] Kermit K Murray. Resolution and resolving power in mass spectrometry. *Journal of the American Society for Mass Spectrometry*, 33(12):2342–2347, 2022.

[93] Robert J. Cotter. *Time-of-flight mass spectrometry: Instrumentation and applications in biological research*. ACS:Washington, 1997.

[94] BA Mamyrin, VI Karataev, DV Shmikk, and VA Zagulin. The mass-reflectron, a new nonmagnetic time-of-flight mass spectrometer with high resolution. *Zh. Eksp. Teor. Fiz*, 64(1):82–89, 1973.

[95] Timothy J Cornish, Robert J Cotter, and Peter J Todd. A curved field reflectron time-of-flight mass spectrometer for the simultaneous focusing of metastable product ions. *Rapid Communications in Mass Spectrometry*, 8(9):781–785, 1994.

[96] Yoshida Y. *U.S. Patent*, 4625112, 1984.

[97] Joo Yeon Oh, Jeong Hee Moon, and Myung Soo Kim. Tandem time-of-flight mass spectrometer for photodissociation of biopolymer ions generated by matrix-assisted laser desorption ionization (maldi-tof-pd-tof) using a linear-plus-quadratic potential reflectron. *Journal of the American Society for Mass Spectrometry*, 15(8):1248–1259, 2004.

[98] David J Manura and David A Dahl. *SIMION 8.0/8.1 User Manual: Covering SIMION Version 8.1. 0.31*. Scientific Instrument Services, Incorporated, 2011.

[99] Seymour Meyerson. Letters to the editors. *Biomedical Mass Spectrometry*, 2(1):59–62, 1975.

[100] Robert W Boyd. Nonlinear optics. Springer, 2003.

[101] A Max Sayler. *Measurements of ultrashort intense laser-induced fragmentation of simple molecular ions*. Kansas State University, 2008.

[102] Light Conversion. Nonlinear optical interactions. `https://toolbox.lightcon.com/tools/PMangles`.

[103] Light Conversion. Material dispersion. `https://toolbox.lightcon.com/tools/dispersionparameters`.

[104] Nicolas Posseme. *Plasma Etching Processes for CMOS Devices Realization*. Elsevier, 2017.

[105] RG Poulsen. Plasma etching in integrated circuit manufacture—a review. *Journal of vacuum science and technology*, 14(1):266–274, 1977.

[106] Joseph W Haus. *Fundamentals and applications of nanophotonics*. Woodhead Publishing, 2016.

[107] Eiichi Soda, Seiichi Kondo, Shuichi Saito, Koji Koyama, Butsurin Jinnai, and Seiji Samukawa. Mechanism of reducing line edge roughness in arf photoresist by using cf3i plasma. *Journal of Vacuum Science & Technology B: Microelectronics and Nanometer Structures Processing, Measurement, and Phenomena*, 27(5):2117–2123, 2009.

[108] Ziad El Otell, V Šamara, Alexey Zotovich, Terje Hansen, Jean-Francois de Marneffe, and MR Baklanov. Vacuum ultra-violet emission of cf4 and cf3i

containing plasmas and their effect on low-k materials. *Journal of Physics D: Applied Physics*, 48(39):395202, 2015.

[109] AN Goyette, Yicheng Wang, and James K Olthoff. Comparison of the identities, fluxes, and energies of ions formed in high density fluorocarbon discharges. In *AIP Conference Proceedings*, volume 550, pages 238–242. American Institute of Physics, 2001.

[110] S Marienfeld, II Fabrikant, M Braun, MW Ruf, and H Hotop. High resolution low-energy electron attachment to cf3i. *Journal of Physics B: Atomic, Molecular and Optical Physics*, 39(1):105, 2005.

[111] M Georgina Scarton. *A study of photoinduced dissociative electron attachment within ion-molecule complexes*. Yale University, 1995.

[112] Richard Mabbs, Eric Surber, and Andrei Sanov. Photoelectron anisotropy and channel branching ratios in the detachment of solvated iodide cluster anions. *The Journal of chemical physics*, 122(5), 2005.

[113] Kim M Lapere, Robert J LaMacchia, Lin H Quak, Marcus Kettner, Stephen G Dale, Allan J McKinley, and Duncan A Wild. Anion photoelectron spectra and ab initio calculations of the iodide–carbon monoxide clusters: I–···(co) n, n= 1–4. *The Journal of Physical Chemistry A*, 116(14):3577–3584, 2012.

[114] TM Stephen and BL Peko. Absolute calibration of a multichannel plate detector for low energy o, o-, and o+. *Review of Scientific Instruments*, 71(3):1355–1359, 2000.

[115] CA Keller and BH Cooper. Quantitative detection of low energy positive and negative ions with a channel electron multiplier. *Review of scientific instruments*, 67(8):2760–2764, 1996.

[116] JN Chen, M Shi, S Tachi, and JW Rabalais. Detection of low energy neutrals by a channel electron multiplier. *Nuclear Instruments and Methods in Physics Research Section B: Beam Interactions with Materials and Atoms*, 16(1):91–95, 1986.

[117] Brent D Koplitz and Jeffrey K McVey. Mechanism and power dependence of the multiphoton ionization of bromobenzene. *The Journal of chemical physics*, 80(6):2271–2282, 1984.

[118] Donald F McMillen and David M Golden. Hydrocarbon bond dissociation energies. *Annual Review of Physical Chemistry*, 33(1):493–532, 1982.

[119] EW Lemmon, MO McLinden, and DG Friend. Nist chemistry webbook (http://webbook. nist. gov); jd cox, dd wagman and va medvedev. *CODATA Key Values for Thermodynamics (http://www. codata. org)*.

[120] Tatiana Oster, Alexander Kühn, and Eugen Illenberger. Gas phase negative ion chemistry. *International journal of mass spectrometry and ion processes*, 89(1):1–72, 1989.

[121] Knut R Asmis, Travis R Taylor, Cangshan Xu, and Daniel M Neumark. Anion photoelectron spectroscopy of i2- and i2- arn (n= 1–14, 16, 20) clusters. *The Journal of chemical physics*, 109(11):4389–4395, 1998.

[122] Bradley F Parsons, Sean M Sheehan, Kathryn E Kautzman, Terry A Yen, and Daniel M Neumark. Photoelectron imaging of i2- at 5.826 ev. *The Journal of chemical physics*, 125(24), 2006.

[123] Wing-Cheung Tam and SF Wong. Dissociative attachment of halogen molecules by 0–8 ev electrons. *The Journal of Chemical Physics*, 68(12):5626–5630, 1978.

[124] Pedatsur Neta, Miomir Simic, and Elie Hayon. Pulse radiolysis of aliphatic acids in aqueous solutions. i. simple monocarboxylic acids. *The Journal of Physical Chemistry*, 73(12):4207–4213, 1969.

[125] Oddur Ingólfsson. *Low-Energy Electrons: Fundamentals and Applications*. CRC Press, 2019.

[126] Wolfgang Sailer, Andrzej Pelc, Michael Probst, Jumras Limtrakul, Paul Scheier, Eugen Illenberger, and Tilmann D Märk. Dissociative electron attachment to acetic acid (ch3cooh). *Chemical physics letters*, 378(3-4):250–256, 2003.

[127] A Pelc, W Sailer, P Scheier, NJ Mason, E Illenberger, and TD Märk. Electron attachment to simple organic acids. *Vacuum*, 70(2-3):429–433, 2003.

[128] A Pelc, W Sailer, P Scheier, and TD Märk. Generation of (m–h)- ions by dissociative electron attachment to simple organic acids m. *Vacuum*, 78(2-4):631–634, 2005.

[129] Dipayan Chakraborty, Giorgi Kharchilava, Ian Carmichael, and Sylwia Ptasinska. Dissociative electron attachment studies of gas-phase acetic acid using a velocity map imaging technique. *Journal of Physics B: Atomic, Molecular and Optical Physics*, 56(24):245202, 2024.

[130] Vaibhav S Prabhudesai, Dhananjay Nandi, Aditya H Kelkar, and E Krishnakumar. Functional group dependent dissociative electron attachment to simple organic molecules. *The Journal of chemical physics*, 128(15), 2008.

[131] T. C. Freitas, M. T.Do N. Varella, R. F. Da Costa, M. A.P. Lima, and M. H.F. Bettega. Low-energy electron collisions with acetic acid. *Physical Review A - Atomic, Molecular, and Optical Physics*, 79(2), 2 2009.

[132] M. Bertin, D. Cáceres, M.P. Davis, R. Balog, A. Lafosse, N.J. Mason, E. Illenberger, and R. Azria. Electron stimulated desorption of h ions from condensed acetic acid. *Chemical Physics Letters*, 433(4):292–295, 2007.

[133] Zhou Lu and Robert E. Continetti. Dynamics of the acetyloxyl radical studied by dissociative photodetachment of the acetate anion. *The Journal of Physical Chemistry A*, 108(45):9962–9969, 2004.

[134] E. A. Lissi, G. Massiff, and A. E. Villa. Oxidation of carbon monoxide by methoxy-radicals. *J. Chem. Soc., Faraday Trans. 1*, 69:346–351, 1973.

[135] Baoshan Wang, Hua Hou, and Yueshu Gu. Ab initio/density functional theory and multichannel rrkm calculations for the ch3o + co reaction. *The Journal of Physical Chemistry A*, 103(40):8021–8029, 1999.

[136] Prasad Ramesh Joshi, Kylie Chia-Yee How, and Yuan-Pern Lee. Hydrogen abstraction of acetic acid by hydrogen atom to form carboxymethyl radical• ch2c (o) oh in solid para-hydrogen and its implication in astrochemistry. *ACS Earth and Space Chemistry*, 5(1):106–117, 2021.

[137] PJ Chantry and GJ Schulz. Kinetic-energy distribution of negative ions formed by dissociative attachment and the measurement of the electron affinity of oxygen. *Physical Review*, 156(1):134, 1967.

[138] Richard N Zare. Dissociation of h2+ by electron impact: Calculated angular distribution. *The Journal of Chemical Physics*, 47(1):204–215, 1967.

[139] Thomas F O'Malley and Howard S Taylor. Angular dependence of scattering products in electron-molecule resonant excitation and in dissociative attachment. *Physical Review*, 176(1):207, 1968.

[140] Daniel J. Haxton, C. William McCurdy, and Thomas N. Rescigno. Angular dependence of dissociative electron attachment to polyatomic molecules: Application to the $^2b_1$ metastable state of the h_2O and h_2S anions. *Phys. Rev. A*, 73:062724, Jun 2006.

[141] GCG Waschewsky, PW Kash, TL Myers, DC Kitchen, and LJ Butler. What woodward and hoffmann didn't tell us: the failure of the born-oppenheimer approximation in competing reaction pathways. *Journal of the Chemical Society. Faraday transactions*, 90(12):1581–1598, 1994.

[142] Hyuk Kang, Boyong Jung, and Seong Keun Kim. Mechanism for ultrafast internal conversion of adenine. *The Journal of chemical physics*, 118(15):6717–6719, 2003.

[143] D. S. Slaughter, A. Belkacem, C. W. McCurdy, T. N. Rescigno, and D. J. Haxton. Ion-momentum imaging of dissociative attachment of electrons to molecules. *Journal of Physics B: Atomic, Molecular and Optical Physics*, 49(22), 2016.

[144] DJ Haxton, Hidihito Adaniya, DS Slaughter, B Rudek, Timur Osipov, Thorsten Weber, TN Rescigno, CW McCurdy, and Ali Belkacem. Observation of the dynamics leading to a conical intersection in dissociative electron attachment to water. *Physical Review A*, 84(3):030701, 2011.

[145] R Azria, Y Le Coat, G Lefevre, and D Simon. Dissociative electron attachment on H2S: energy and angular distributions of H-ions. Technical Report 4, 1979.

[146] M Tronc, C Schermann, RI Hall, and F Fiquet-Fayard. Differential cross sections and angular distributions of h-from dissociative electron attachment to h2 between 3.75 ev and 13 ev. *Journal of Physics B: Atomic and Molecular Physics*, 10(2):305, 1977.

[147] N Bhargava Ram and E Krishnakumar. Dissociative electron attachment to h 2 s probed by ion momentum imaging. *Physical Chemistry Chemical Physics*, 13(30):13621–13628, 2011.

[148] Krishnendu Gope, Nigel Mason, E Krishnakumar, and Vaibhav S Prabhudesai. Dea dynamics of chlorine dioxide probed by velocity slice imaging. *Physical Chemistry Chemical Physics*, 21(26):14023–14032, 2019.

[149] Dipayan Chakraborty, Aranya Giri, and Dhananjay Nandi. Dissociation dynamics in low energy electron attachment to ammonia using velocity slice imaging. *Physical Chemistry Chemical Physics*, 21(39):21908–21917, 2019.

[150] Pamir Nag, Michal Tarana, and Juraj Fedor. Effects of $\pi^*-\sigma^*$ coupling on dissociative-electron-attachment angular distributions in vinyl, allyl, and benzyl chloride and in chlorobenzene. *Phys. Rev. A*, 103:032830, Mar 2021.

[151] Dipayan Chakraborty, Daniel S. Slaughter, and Sylwia Ptasinska. Dynamics of resonant low-energy electron attachment to ethanol-producing hydroxide anions. *Phys. Rev. A*, 108:052806, Nov 2023.

[152] J Fedor, P Cicman, B Coupier, S Feil, M Winkler, K Głuch, J Husarik, D Jaksch, B Farizon, NJ Mason, et al. Fragmentation of transient water anions following low-energy electron capture by h2o/d2o. *Journal of Physics B: Atomic, Molecular and Optical Physics*, 39(18):3935, 2006.

[153] Prashant Rawat, Vaibhav S Prabhudesai, G Aravind, M A Rahman, and E Krishnakumar. Absolute cross sections for dissociative electron attachment to h2o and d2o. *Journal of Physics B: Atomic, Molecular and Optical Physics*, 40(24):4625, nov 2007.

[154] Hidehito Adaniya. *Imagining dissociation dynamics: Experimental study of electron attachment to water molecule by COLTRIMS technique*. PhD thesis, University of California, Davis, January 2009.

[155] Martina Kieninger, Oscar N Ventura, and Sandor Suhai. Density functional investigations of carboxyl free radicals: Formyloxyl, acetyloxyl, and benzoyloxyl radicals. *International journal of quantum chemistry*, 70(2):253–267, 1998.

[156] Paul G Wenthold and Robert R Squires. Gas-phase properties and reactivity of the acetate radical anion. determination of the ch bond strengths in acetic acid and acetate ion. *Journal of the American Chemical Society*, 116(26):11890–11897, 1994.

[157] Xue-Bin Wang, Hin-Koon Woo, Lai-Sheng Wang, Babak Minofar, and Pavel Jungwirth. Determination of the electron affinity of the acetyloxyl radical

(ch3coo) by low-temperature anion photoelectron spectroscopy and ab initio calculations. *The Journal of Physical Chemistry A*, 110(15):5047–5050, 2006.

[158] Dao-Ling Huang, Guo-Zhu Zhu, and Lai-Sheng Wang. Communication: Observation of dipole-bound state and high-resolution photoelectron imaging of cold acetate anions. *The Journal of Chemical Physics*, 142(9), 2015.

[159] Jean Ann Wyer, Linda Feketeová, Steen Brøndsted Nielsen, and AJ Richard. Gas phase fragmentation of protonated betaine and its clusters. *Physical Chemistry Chemical Physics*, 11(39):8752–8758, 2009.

[160] Stephen Bell, TL Ng, and AD Walsh. Vacuum ultra-violet spectra of formic and acetic acids. *Journal of the Chemical Society, Faraday Transactions 2: Molecular and Chemical Physics*, 71:393–401, 1975.

[161] Masako Suto, Xiuyan Wang, and LC Lee. Fluorescence yields from photodissociative excitation of hcooh, hcooch3, and ch3cooh in the vacuum-ultraviolet region. *Journal of Physical Chemistry*, 92, 1988.

[162] Edwin E Barnes and William T Simpson. Correlations among electronic transitions for carbonyl and for carboxyl in the vacuum ultraviolet. *The Journal of Chemical Physics*, 39(3):670–675, 1963.

[163] Melvin Robin. *Higher Excited States of Polyatomic Molecules V3*, volume 3. Elsevier, 2012.

[164] S. Nagakura, K. Kaya, and H. Tsubomura. Vacuum ultraviolet absorption spectra and electronic structures of formic acid, acetic acid and ethyl acetate. *Journal of Molecular Spectroscopy*, 13(1):1–8, 1964.

[165] Tayfun Ari and M Haluk Güven. Valence–shell electron energy-loss spectra of formic acid and acetic acid. *Journal of Electron Spectroscopy and Related Phenomena*, 106(1):29–35, 2000.

[166] J Lu Derissen. A reinvestigation of the molecular structure of acetic acid monomer and dimer by gas electron diffraction. *Journal of Molecular Structure*, 7(1-2):67–80, 1971.

[167] Michael B Barton, Susannah Jacob, Jesmin Shafiq, Karen Wong, Stephen R Thompson, Timothy P Hanna, and Geoff P Delaney. Estimating the demand for radiotherapy from the evidence: a review of changes from 2003 to 2012. *Radiotherapy and oncology*, 112(1):140–144, 2014.

[168] Csaba Polgár, Oliver J Ott, Guido Hildebrandt, Daniela Kauer-Dorner, Hellen Knauerhase, Tibor Major, Jaroslaw Lyczek, José Luis Guinot, Jürgen Dunst, Cristina Gutierrez Miguelez, et al. Late side-effects and cosmetic results of accelerated partial breast irradiation with interstitial brachytherapy versus whole-breast irradiation after breast-conserving surgery for low-risk invasive and in-situ carcinoma of the female breast: 5-year results of a randomised, controlled, phase 3 trial. *The Lancet Oncology*, 18(2):259–268, 2017.

[169] Jens Overgaard. Hypoxic radiosensitization: adored and ignored. *Journal of Clinical Oncology*, 25(26):4066–4074, 2007.

[170] Hao Wang, Xiaoyu Mu, Hua He, and Xiao-Dong Zhang. Cancer radiosensitizers. *Trends in pharmacological sciences*, 39(1):24–48, 2018.

[171] Thomas Sommerfeld. Intramolecular electron transfer from dipole-bound to valence orbitals: Uracil and 5-chlorouracil. *The Journal of Physical Chemistry A*, 108(42):9150–9154, 2004.

[172] Hsiu-Yao Cheng and Chi-Wei Chen. Energy and lifetime of temporary anion states of uracil by stabilization method. *The Journal of Physical Chemistry A*, 115(35):10113–10121, 2011.

[173] Yeunsoo Park, Katarzyna Polska, Janusz Rak, J Richard Wagner, and Leon Sanche. Fundamental mechanisms of dna radiosensitization: Damage induced by low-energy electrons in brominated oligonucleotide trimers. *The Journal of Physical Chemistry B*, 116(32):9676–9682, 2012.

[174] Katrin Tanzer, Linda Feketeová, Benjamin Puschnigg, Paul Scheier, Eugen Illenberger, and Stephan Denifl. Reactions in nitroimidazole and methylnitroimidazole triggered by low-energy (0–8 ev) electrons. *The Journal of Physical Chemistry A*, 119(25):6668–6675, 2015.